Astronomy Letters, Vol. 27, No. 11, 2001, pp. 683–685. Translated from Pis'ma v Astronomicheskiĭ Zhurnal, Vol. 27, No. 11, 2001, pp. 803–806.

HD Molecular Lines in an Absorption System at Redshift $z = 2.3377$

D. A. Varshalovich[1, *], A. V. Ivanchik[1], P. Petitjean[2], R. Srianand[3], and C. Ledoux[4]

[1] *Ioffe Physicotechnical Institute, ul. Politekhnicheskaya 26, St. Petersburg, 194021 Russia*
[2] *Institut d'Astrophysique, Paris, France*
[3] *IUCAA, Pune, India*
[4] *ESO, München, Germany*

Received June 26, 2001

Abstract—Having analyzed the spectrum of the quasar PKS 1232+0.82 taken by Petitjean *et al.* (2000), we identified HD molecular lines in an absorption system at redshift $z = 2.3377$. We estimated the column density of HD molecules in this system, $N(\mathrm{HD}) = (1-4) \times 10^{14}$ cm^{-2}. The excitation temperature of the first rotational level $J = 1$ relative to the ground state $J = 0$ is $T_{\mathrm{ex}} = 70 \pm 7$ K. As far as we know, this is the first detection of HD molecules at high redshift. © 2001 MAIK "Nauka/Interperiodica"

Key words: *quasar spectra, observational cosmology*

INTRODUCTION

The relative abundance of deuterium [D]/[H] produced during Big Bang nucleosynthesis is one of the key parameters of modern cosmology, because it is the most sensitive indicator of the baryon density in the Universe.

The deuterium abundance at early cosmological epoch (10–14 Gyrs ago) can be determined from high-redshift quasar spectra. Until now, only atomic lines of D I and H I have been used to measure the relative abundances of D I and H I. However, this method runs into serious difficulties. The D I and H I wavelengths almost coincide, viz $\lambda(\mathrm{H\,I})/\lambda(\mathrm{D\,I}) = 1.00027$. Moreover, the column densities of D I and H I differ by a factor of $10^{-4} - 10^{-5}$. Therefore, D I lines are very weak and virtually undetectable when the column density of hydrogen is low. When the hydrogen column density is high enough, H I lines are saturated and broadened, so that D I lines are lost in the H I lines. In addition, one cannot be sure that the lines treated as D I lines are actually D I and not produced by an intervening weak H I cloud shifted in velocity by -80 km s^{-1}. (The latter explanation is possible, because the lines in question are situated within the Ly-α forest where absorption features are numerous.) The above difficulties may be the reason why the [D]/[H] values determined from atomic lines by different authors differ by more than an order of magnitude. For example, 2×10^{-4} (Webb *et. al* 1997) and 1.6×10^{-5} (Pettini and Bowen 2001).

The above difficulties do not arise if the relative abundances of molecules [HD]/[H_2] are measured, because the corresponding wavelengths differ significantly while the redshift parameter is the same. However, it may be difficult to derive [D]/[H] from [HD]/[H_2] because of uncertainties in the chemistry. Nevertheless, this is an independent access to the deuterium abundance in these remote clouds.

Until now, HD lines have not been identified in quasar spectra. Moreover, for a long period, from 1985 to 1997, the only molecular absorption system was known, viz. the H_2 system at $z_{abs} = 2.811$ imprinted in the spectrum of PKS 0528-250 (Levshakov and Varshalovich 1985). At present, only four reliable absorption systems of molecular hydrogen H_2 are known in quasar spectra (Petitjean *et al.* 2000; Levshakov *et al.* 2001) and no other molecules have been detected in their optical spectra.

RESULTS OF ANALYSIS OF THE PKS 1232+082 SPECTRUM

Here, we report on the identification of HD lines in the absorption system at $z_{abs} = 2.3377$ in the spectrum of PKS 1232+082 ($z_{em} = 2.57$ and $m_V = 18.4$). To the best of our knowledge, this is the first identification of redshifted HD molecules.

A high-resolution spectrum of PKS 1232+082 was taken using UVES with the 8.2-m ESO VLT telescope by Petitjean *et al.* (2000). The spectrum contains the strong absorption system of molecular hydrogen H_2 at $z_{abs} = 2.3377$ previously found by Ge and Bechtold (1999).

*E-mail: varsh@astro.ioffe.rssi.ru

1063-7737/01/2711-0683$21.00

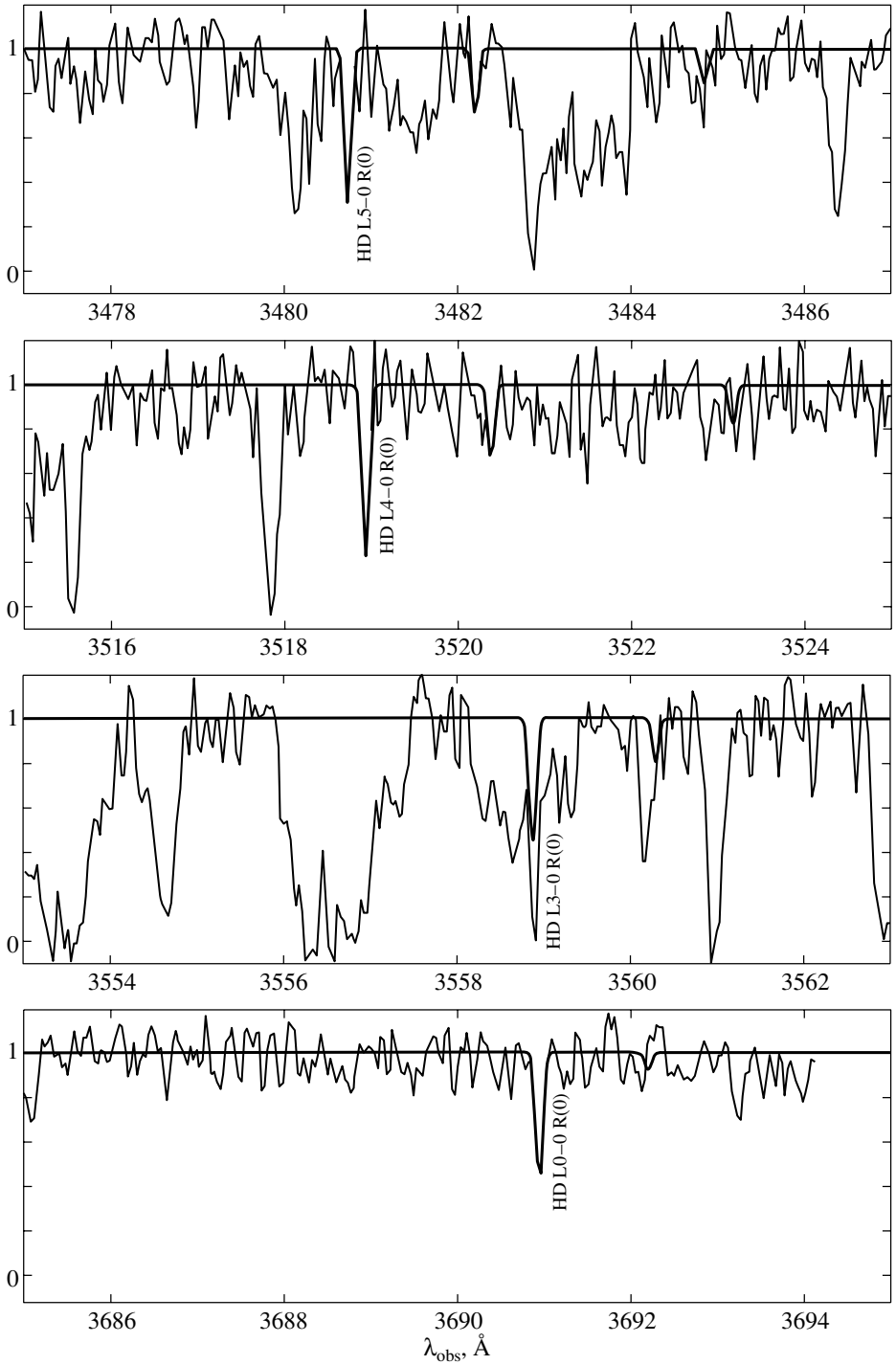

Portions of the VLT spectrum for PKS 1232+082 taken by Petitjean *et al.* (2000). The solid line represents our theoretical HD spectrum.

We found several HD lines of the Lyman series $B\,^1\Sigma^+ - X\,^1\Sigma^+$ corresponding to R(0) transitions from the ground state $J = 0$, $v = 0$, and some tentative lines R(1) from the first rotational level $J = 1$, $v = 0$.

The figure shows portions of the observed spectrum for PKS 1232+082 and our synthetic fit of HD lines. We see R(0) lines in the L 5-0, L 4-0, L 3-0, and L 0-0 bands and some possible R(1) lines, whereas HD lines in L 2-0 and L 1-0 bands are heavily blended by H_2 lines. Parameters of the identified HD lines are given in the table. We took the spectroscopic data on laboratory lines from the measurements by Dabrowski and Herzberg (1976) and the oscillator strengths from Allison and Dalgarno (1970).

The weighted mean value of the redshift parameter

Parameters of the identified lines of HD molecules in the spectrum of PKS 1232+082 in the system at $z_{abs} = 2.3377$

Transition	λ_{lab}, Å	λ_{obs}, Å	z_{abs}
L 5-0 R(0)	1042.854	3480.729(3)	2.337695
R(1)	1043.229	3482.219(9)	2.337699
L 4-0 R(0)	1054.298	3518.935(4)	2.337704
R(1)	1054.734	3520.397(12)	2.337711
L 3-0 R(0)	1066.279	3558.923(3)	2.337703
R(1)	1066.706	3560.34[b]	...
L 2-0 R(0)	1078.835	3600.83[b]	...
R(1)	1079.248	3602.21[b]	...
L 1-0 R(0)	1092.006	3644.79[b]	...
R(1)	1092.404	3646.12[b]	...
L 0-0 R(0)	1105.845	3690.972(2)	2.337694
R(1)	1106.221	3692.23	...

[b] HD line is blended

for the measured HD absorption system is

$$z_{abs}(\mathrm{HD}) = 2.337700(5),$$

in good agreement with $z_{abs}(\mathrm{H_2}) = 2.33771$ (Petitjean *et al.* 2000).

According to our estimates, the column densities of HD molecules in the ground state $J = 0$ and in the first rotational state $J = 1$ are

$$N_{J=0}(\mathrm{HD}) = (1-3) \times 10^{14}\ \mathrm{cm}^{-2},$$

$$N_{J=1}(\mathrm{HD}) = (4-8) \times 10^{13}\ \mathrm{cm}^{-2}.$$

The population of the first rotational level relative to the ground state may be characterized by the excitation temperature:

$$T_{ex} = 70 \pm 7\ \mathrm{K}.$$

However, the R(1) lines have low S/N ratios, so that this value may be considered as an upper limit on T_{ex}. New observations with higher S/N are necessary to confirm the lines from the J=1 level.

A detailed analysis of the relative abundances [HD]/[H_2] and the corresponding estimates of [D]/[H] will be performed elsewhere. Note that an additional problem of interstellar chemistry (concerned with the formation and destruction of molecules) has to be solved to determine [D]/[H] from [HD]/[H_2].

In conclusion, we emphasize that the detection of HD molecules in absorbing matter at such a high redshift may be of importance in understanding the formation of the first generation of stars, because HD molecules could be important cooling agents in the primordial condensations where heavy elements were in deficit.

ACKNOWLEDGMENTS

The work of D.A. Varshalovich and A.V. Ivanchuk was supported in part by the Russian Foundation for Basic Research (project nos. 99-02-18232, 01-02-06098) and the Russian State Program "Astronomy." The observations have been obtained with UVES mounted on the 8.2-m KUEYEN telescope operated by the European Southern Observatory at Parana, Chile. R. Srianand and P. Petitjean acknowledge support from the Indo-French Centre for the Promotion of Advanced Research (Centre Franco-Indian pour la Promotion de la Recherche Avancée) under contract no. 1710-1.

REFERENCES

1. A. C. Allison and A. Dalgarno, Atomic Data **1**, 289 (1970).
2. I. Dabrowski and G. Herzberg, Canadian J. Phys. **54**, 525 (1976)
3. D. R. Flower and E. Roueff, Mon. Not. R. Astron. Soc. **309**, 833 (1999).
4. J. Ge and J. Bechtold, Astron. Soc. Pac. Conf. Ser. **156**, 121 (1999).
5. S. A. Levshakov, M. Dessauges-Zavadsky, and S. D'Odorico, astro-ph/0105529 (2001).
6. S. A. Levshakov and D. A. Varshalovich, Mon. Not. R. Astron. Soc. **212**, 517 (1985).
7. P. Petitjean, R. Srianand, and C. Ledoux, astro-ph/0011437 (2000).
8. M. Pettini and D. Bowen, astro-ph/0104474 (2001).
9. R. Srianand, P. Petitjean, and C. Ledoux, astro-ph/0012222 (2000).
10. J. K. Webb, R. F. Carswell, K. M. Lanzetta, *et al.*, Nature **388**, 250 (1997).

Translated by V. Astakhov

Astronomy Letters, Vol. 27, No. 11, 2001, pp. 686–690. Translated from Pis'ma v Astronomicheskiĭ Zhurnal, Vol. 27, No. 11, 2001, pp. 807–811.

H II Regions and Radio Visibility of Quasar Nuclei

L. I. Matveenko*

Space Research Institute, Russian Academy of Sciences, ul. Profsoyuznaya 84/32, Moscow, 117810 Russia

Received June 25, 2001

Abstract—The core (injector) and the jet (relativistic plasma outflow) of AGN objects are surrounded by an ionized medium, an H II region observed in emission lines. The synchrotron radiation from the core and the jet is observed through a thin screen that cocoons the structure under consideration. The screen transparency depends on wavelength and distance from the injector. We consider the objects 3C 345 and 1803 + 784 whose core emission at decimeter wavelengths is absorption by more than 25 dB. The visible bright compact component is the bright nearby portion of the jet that extends outside the dense part of the screen. We explore the possibility of measuring the screen transparency from absorption in $H\alpha$ recombination lines with different quantum numbers at centimeter wavelengths. © 2001 MAIK "Nauka/Interperiodica"

Key words: *active galactic nuclei, quasars and radio galaxies, H II regions, absorption, recombination lines*

INTRODUCTION

AGN objects are galaxies with enhanced nuclear activity. These can be various types of galaxies and galaxies at different formation stages of their nuclei and at different stages of their activity. As follows from high-angular-resolution radio observations, nuclear activity manifests itself as the ejection of relativistic plasma flow at a velocity close to the speed of light and its subsequent self-focusing into a thin jet. Occasionally, dense knots of relativistic plasma responsible for radio outbursts are ejected. The outburst radio emission is delayed and decreases in intensity with increasing wavelength. The plasma temperature reaches the Compton limit, $T = 10^{12}$ K (Kellermann and Pauliny-Toth 1969). In several cases, this limit is exceeded.

However, variability that does not correlate or anticorrelates with high-frequency outbursts again increases at low frequencies. This is probably attributable to a change in the transparency of the ambient ionized gas. The quasars 3C 345 and 1803 + 784 are typical AGN objects. Below, we consider the possibility of studying the ambient ionized medium from hydrogen recombination absorption lines.

THE FINE STRUCTURE OF AGN OBJECTS

The quasars 3C 345 and 1803+784 have similar redshifts: $z = 0.595$ and 0.68, respectively. Their cores are the injectors of relativistic plasma. A plasma flow is ejected at a relativistic velocity and is focused into a thin, helically wound jet. The core (injector) radio emission dominates at millimeter and short centimeter wavelengths. The optical depth of the jet decreases with increasing distance from the core, and only its nearby part is visible in the frequency range under consideration. The jet optical depth increases with wavelength, which results in the dominance of its radio emission. Radio outbursts correspond to the compact components, dense knots of relativistic plasma moving at velocities close to the speed of light. The brightness temperatures of the compact optically thick structures reach $T_b \approx 10^{12}$ K.

In several cases, high-frequency radio outbursts are accompanied by a reduction in the intensity of the low-frequency emission (negative outbursts). This phenomenon was particularly pronounced in the object 0950 + 658 at a frequency of 2.6 GHz (Fiedler *et al.* 1987). Aller and Aller (1982) noted a general anticorrelation between the high-frequency and low-frequency emissions. The time scale of the low-frequency variability is 1–2 years.

Quasar 3C 345. Radio outbursts were observed in this object in the frequency range 8–89.6 GHz during its enhanced activity between 1981.5 and 1982.5 (Bregman *et al.* 1986; Unwin *et al.* 1983). Studies of one of the most intense outbursts at epoch 1981.6 revealed a cutoff in its spectrum at the frequency $f = 8$ GHz. The low-frequency spectral index is $\alpha \geq 2.6$. The observed features at decimeter wavelengths are attributable to absorption in the ambient ionized

*E-mail: lmatveen@mx.iki.rssi.ru

1063-7737/01/2711-0686$21.00

medium, whose electron density depends on nuclear activity (Matveyenko *et al.* 1986)

The fine structure of the quasar 3C 345 was investigated at low frequencies, at the decimeter wavelengths $\lambda = 18$, 49, and 92 cm (Rantakyro *et al.* 1992; Matveyenko 1993; Matveyenko *et al.* 1996a, 1996b; Matveyenko and Witzel 1999). Most of the 18-cm emission is produced by a bright, compact (10×5 mas) region that lies at a distance of 2 mas from the injector. The effective size of the region changes from epoch to epoch, but the brightness temperature is virtually constant, $T_{\rm peak} \approx 0.2 \times 10^{12}$ K, which determines the change in the radio flux density. In this case, the core brightness temperature does not exceed a few percent of $T_{\rm peak}$.

At $\lambda = 49$ cm, the bright compact region is at 16 mas from the injector and has an effective size of 5×4 mas. Its brightness temperature is $T_{\rm b} \approx 0.5 \times 10^{12}$ K, while the apparent core brightness temperature is 0.003 $T_{\rm peak}$ or 25 dB lower (Matveyenko *et al.* 1996).

At 92 cm, the size of the bright region is 22.6×9.4 mas and $T_{\rm b} \approx 10^{11}$ K. This region corresponds to the nearby part of the jet and lies at ~ 30 mas from the injector (Hong Xia-yu *et al.* 1995). The core radio emission is virtually invisible.

Studies of the fine structure in the quasar 3C 345 at 6 cm show that the core (injector) brightness temperature is lower than the temperature of the nearby compact objects, $T_{\rm b} \approx 0.2 T_{\rm peak}$ (epoch 1990), with the brightness temperatures of the latter reaching 10^{12} K (Unwin and Wehrle 1992; Ros *et al.* 2000; Klare *et al.* 2001). The optical depth of the relativistic plasma in the injector region cannot be lower than that in the nearby components; neither can its brightness temperature. Such a reduction can be caused by the absorption of synchrotron radiation even at this frequency.

Thus, the core spectrum is similar to the outburst spectrum and has a low-frequency cutoff at $f \approx 7$ GHz. The low-frequency spectral index is $\alpha \approx 4$ (Matveyenko *et al.* 1982; Matveyenko and Witzel 1999).

Quasar 1803 + 784. Measurements of the fine structure in the object 1803 + 784 at $\lambda = 18$ cm (Matveyenko and Witzel 1999; Britzen *et al.* 2001; Matveyenko *et al.* 2000) show that the peak brightness temperature of the compact source is almost equal to the Compton limit, $T_{\rm peak} \approx 10^{12}$ K. This source lies at 2 mas from the core. The core brightness temperature is no less than 25 dB lower than the brightness temperature $T_{\rm peak}$, which corresponds to the screen absorption in the injector region at 18 cm by more than 25 dB. The optical depth of the screen at this wavelength decreases with distance from the injector as $\tau \approx 5.5(1 - R/R_0)$ (Matveyenko and Witzel 1999).

A similar spectrum with a low-frequency cutoff is observed for the nucleus of the Seyfert galaxy NGC 1275 (radio source 3C 84, $z = 0.0176$). The cutoff frequency is $f \approx 10$ GHz, and the low-frequency spectral index is $\alpha \approx 3.3$. The optical depth at 18 cm is $\tau \approx 9$, the emission measure is ME $\approx 7 \times 10^7$ cm^{-6} pc, and $N_{\rm e} \approx 10^4$ cm^{-3} (Matveyenko *et al.* 1980, 1985)

H II REGION

The emission from H II regions of AGN objects is observed in narrow and broad $H\alpha$ emission lines. The electron density of these narrow-line regions is $N_{\rm e} \cong 10^5$–10^6) cm^{-3}. As follows from the regions' luminosities, their effective sizes are $\sim 10^{21} L_{46}$ cm, where L_{46} is the ultraviolet luminosity, in units of 10^{46} erg s^{-1}. For broad lines, the regions are $\sim 10^{18.5}\ L_{46}$ cm in size, and their electron density can reach $\sim 10^8$ cm^{-3}. The electron temperatures of the regions under consideration are $T_{\rm e} = 2 \times 10^4$ K (Netzer 1987). The dense blobs in the H II regions are almost completely opaque to radio waves, but they constitute only a small part of the screen.

For the quasars 3C 345 and 1803 + 784, the effective size of the narrow-line H II region reaches $\sim 10^{20}$ cm or ~ 3 pc (~ 8 mas). This ionized medium covers the core (injector) region, the compact components, and the nearby bright part of the jet, which produce most of the object's emission at centimeter and decimeter wavelengths.

The spatial distribution of the ionized matter and its relationship to the object's fine structure are unclear. This may be the matter accreted onto the disk in the azimuthal plane. At the same time, the relativistic plasma flow is ejected along the rotation axis of the accretion disk and moves in a low-density medium. This medium is partly swept up by the flow and partly is drawn apart and envelops it by a thin, dense layer like a cocoon wall. The thickness of the cocoon wall is determined by the condition of equilibrium between the thermal- and relativistic-plasma pressures. The pressure in the jet is proportional to the square of the ambient density, $P_{\rm J} \sim \rho^2$, and decreases with distance from the injector as R^{-2} (Begelman *et al.* 1984). In this case, the electron density decreases as $N_{\rm e} \sim R^{-2}$, while the wall thickness increases as $\sim R$. The screen transparency depends on its optical depth and emission measure; the latter decreases as ME $\sim R^{-3}$

The outburst and AGN-core spectra exhibit breaks and are characteristic of the synchrotron radiation

Table 1.

Hα	f, GHz	Δf, MHz
50	51.071	2918
75	15.281	591
100	6.478	190
125	3.327	78

Table 2.

	3C 345	1803 + 784
z	0.595	0.68
f_0/f	1.595	1.68
F, Jy	8	2.5

from optically thick regions. However, their low-frequency cutoffs are steeper ($\alpha > 3$) than those that follow from the reabsorption of synchrotron radiation, whose spectral index under actual conditions must be $\alpha < 2.5$. The spectral break is observed at long centimeter wavelengths, at $f \approx 7$ GHz.

Thus, the spectral features and the low-frequency variability can be explained by the absorption of synchrotron radio emission from relativistic electrons in an ionized medium, the cocoon wall. The time scale of the low-frequency variability (~ 1 year) and the absorption level imply that the electron density and the screen wall thickness are $N_e \geqslant 10^5$ cm^{-3} and $l < 0.01$ of a light year, respectively. Variations in the ionization of the medium result in variability of the visible low-frequency radio emission from the object (Matveyenko 1993).

The screen transparency is determined by its optical depth. The optical depth of the ionized medium depends on frequency:

$$\tau = 0.08 T_e^{-1.35} [(1+z)f]^{-2.1} \int N_e^2(l) dl,$$

where f is the frequency of the received emission in GHz, $T_e = 2 \times 10^4$ K is the electron temperature of the ionized gas, l is the screen thickness in pc, and $N_e(l)$ is the line-of-sight electron density distribution in cm^{-3}.

The screen electron density in the injector region is $N_e = 10^5$–10^6 cm^{-3} and decreases with distance as $\sim R^{-2}$; the screen wall thickness increases as $\sim R$, while the emission measure decreases as ME $\sim R^{-3}$.

The observed reduction in the jet brightness temperature with distance from the core is attributable to a decrease in the optical depth of the relativistic plasma flow. At short decimeter wavelengths, the jet is optically thick up to ~ 20 mas, and the brightness temperature is close to the Compton limit.

The bright compact sources at decimeter wavelengths are the nearby parts of the jet visible through an absorbing screen. Their positions relative to the injector are determined by the screen transparency. The lower the frequency, the farther the screen from the injector becomes transparent, and, accordingly, the nearby part of the jet (bright component) becomes visible.

In the object 1803 + 784, the absorption of radio emission at $\lambda = 18$ cm ($f_0 = 1$ GHz) reaches ~ 25 dB. This corresponds to an optical depth $\tau \approx 5$, which decreases with distance from the injector as $\tau \approx 6(1 - R/R_0)^{-3}$, where $R_0 = 3$ mas. The screen optical depth depends on frequency, $\sim f^{-2.1}$. At 6.2 cm ($f_0 = 4.8$ GHz), it is smaller than at 18 cm by a factor of 9, $\tau \approx 0.6$, and the absorption does not exceed 1.8. In this case, the apparent core brightness temperature is lower than the temperature of the nearby bright components, $T_b \approx 5 \times 10^{11}$ K, which has been observed by many authors (Unwin and Wehrle 1992; Klare *et al.* 2001; Ros *et al.* 2000).

ABSORPTION IN RECOMBINATION LINES

The absorption of synchrotron radiation in AGN objects in an ionized medium can be independently determined from absorption in recombination lines. Measurements at different frequencies (in different lines) allow the screen absorption to be determined as a function of the distance from the injector.

Recombination lines with different principal quantum numbers Hα, their frequencies f, and line separations Δf are given in Table 1 (Kardashev 1959; Lang 1974).

Radio telescopes are most sensitive at centimeter wavelengths. According to studies of recombination lines in the Orion Nebula, the line-to-continuum ratio increases with decreasing quantum number. This ratio is at a maximum for the lines with quantum numbers $n = 50$–100. In the Orion Nebula, the Hα = 109 line, $f_0 = 5009$ MHz, has the width $\Delta f =$ 485 kHz, and the line-to-continuum temperature ratio is $T_L/T_C = 5.2\%$ (Mezger and Hendenson 1967). In our case, the apparent frequencies of this line for the objects 3C 345 and 1803 + 784 are 3140 and 2982 MHz, respectively (Table 2).

Most of the radio telescopes operate in the range 5–6 GHz, which corresponds to the frequency of the objects under consideration, $f_0 = 8$–9 GHz. The adjacent lines have the quantum numbers $n_x = 83$ ($f_0 = 8093$ MHz, $f = 5058$ MHz) and $n_x = 84$ ($f_0 =$ 7807.7 MHz, $f = 4879.8$ MHz) for the quasar 3C 345

and $n_x = 85$ ($f_0 = 8385.9$ MHz, $f = 4991.6$ MHz) for the object 1803 + 784. The T_L/T_C ratio for the lines with these quantum numbers is even slightly higher than that given above. The line separation $\Delta f \cong 3f/n_x$ is 176 MHz (Gordon 1976).

The increment in antenna temperature when pointing at the source is

$$T_a(f) \sim T_0 e^{-\tau(f)} + T_e(1 - e^{-\tau(f)}),$$

where $T_0 = 10^{12}$ K is the brightness temperature of the central region that produces most of the object's radio emission, $T_e = 2 \times 10^4$ K is the electron temperature of the H II screen, and $\tau(f)$ is the screen optical depth.

The visibility of a recombination absorption line is determined by the screen transparency, by the dependence of its optical depth on frequency f. At high frequencies, $\tau(0) < 1$ and $T(f) \approx T_0 + T_e\tau$. The brightness temperature is $T_0 \gg T_e$ and $T_a(f) \sim T_0$. At low frequencies, $\tau(0) \geqslant 1$ and $T(f) \approx T_0 e^{-\tau} + T_e \approx T_0 e^{-\tau}$.

The line profile is Gaussian; its width is determined by the Doppler broadening (temperature T_e) and microturbulence $\sqrt{\overline{v}_t^2}$ (Gordon 1976):

$$\Delta f/f = [4 \ln 2(2kT/mc^2 + 2\overline{v}_t^2/3c^2)]^{1/2},$$

where m is the mass of the hydrogen atom, and k is the Boltzmann constant.

The thermal line width for $T \approx 10^4$ K is $\Delta\nu/\nu \approx 10^{-4}$ and ~500 kHz for $f \approx 5$ GHz. Since the turbulence of the medium in the core regions of AGN objects is unknown, we cannot estimate the line broadening.

CONCLUSIONS

Measurements of AGN objects in hydrogen Hα radio recombination lines at centimeter wavelengths allow the parameters of the ionized medium that surrounds the injector and the nearby part of the jet to be determined. The expected line absorption accounts for 5% of the brightness temperature of relativistic plasma (background), $T_b \approx 10^{12}$ K. We plan to carry out measurements for the typical quasars 3C 345 and 1803 + 784, whose radio flux densities at 6 cm are given in Table 2.

These measurements can be made with the 100-m Effelsberg radio telescope at 5 GHz. The expected width of the recombination-line profile at these frequencies is ~500 kHz. The frequency resolution may be taken to be 50 kHz. The line separation is $\Delta f \approx 180$ MHz. Given that the redshift z is inaccurate, the band analyzed is taken to be 10 MHz. The sensitivity of the antenna under consideration is ~2K Jy^{-1}. The increment in antenna temperature is $T_a = 15$ K and $T_a = 5$ K for the objects 3C 345 and 1803 + 784, respectively. The expected effect is $T_L = 0.05T_C$ or 0.75 K and 0.25 K. The fluctuation sensitivity is $\delta \approx 0.002$ K for an averaging of 200 s. The signal-to-noise ratio is 25 and 8, respectively.

The effect under consideration must also show up directly in measurements of the relative brightness temperature for the nucleus of 3C 345 on radio maps obtained in different channels at 6 cm with the MK-4 or VLBA systems.

REFERENCES

1. H. D. Aller and M. F. Aller, in *Low Frequency Variability of Extragalactic Radio Sources,* Ed. by W. D. Cotton and S. R. Spangler (Publ. National Radio Astronomy Observatory, Green Bank, 1982), p. 105.
2. M. C. Begelman, R. D. Blanford, and M. J. Rees, Rev. Mod. Phys. **56**, 255 (1984).
3. J. N. Bregman, A. E. Glassgold, P. J. Huggings, *et al.*, Astrophys. J. **301**, 708 (1986).
4. S. Britzen, A. Witzel, T. P. Krichbaum, *et al.*, Pis'ma Astron. Zh. **27**, 3 (2001) [Astron. Lett. **27**, 1 (2001)].
5. R. Fiedler, B. Dennison, and R. Simon, in *National Radio Astronomy Observatory, Green Bank, 1987,* Ed. by J. J. Condon and F. J. Lockman, p. 129.
6. M. A. Gordon, in *Galactic and Extra-Galactic Radio Astronomy,* Ed. by G. L. Verschuur and K. I. Kellermann (Springer-Verlag, New York, 1974; Mir, Moscow, 1976).
7. Hong Xia-yu, Wan Tong-shan, Shen Zhi-qiang, *et al.*, Chin. Astron. Astrophys. **14/4**, 323 (1995).
8. N. S. Kardashev, Astron. Zh. **36**, 838 (1959) [Sov. Astron. Lett. **3**, 813 (1959)].
9. K. I. Kellermann and I. I. K. Pauliny-Toth, Astrophys. J. Lett. **155**, L31 (1969).
10. J. Klare, J. A. Zensus, E. Ros, and A. P. Lobanov, Astron. Astrophys. (2001) (in press).
11. K. R. Lang, in *Astrophysical Formulas* (Springer-Verlag, Berlin, 1974), p. 120.
12. L. I. Matveenko, Pis'ma Astron. Zh. **19**, 291 (1993) [Astron. Lett. **19**, 108 (1993)].
13. L. I. Matveenko and A. I. Witzel, Pis'ma Astron. Zh. **25**, 643 (1999) [Astron. Lett. **25**, 555 (1999)].
14. L. I. Matveenko, K. I. Kellermann, I. I. K. Pauliny-Toth, *et al.*, Pis'ma Astron. Zh. **6**, 77 (1980) [Sov. Astron. Lett. **6**, 42 (1980)].
15. L. I. Matveenko, I. I. K. Pauliny-Toth, and V. I. Kostenko, *et al.*, Pis'ma Astron. Zh. **11**, 420 (1985) [Sov. Astron. Lett. **11**, 173 (1985)].
16. L. I. Matveenko, I. I. K. Pauliny-Toth, W. A. Sherwood, *et al.*, Pis'ma Astron. Zh. **12**, 156 (1986) [Sov. Astron. Lett. **12**, 63 (1986)].
17. L. I. Matveenko, I. I. K. Pauliny-Toth, D. A. Graham, *et al.*, Pis'ma Astron. Zh. **22**, 17 (1996a) [Astron. Lett. **22**, 14 (1996a)].
18. L. I. Matveenko, I. I. K. Pauliny-Toth, L. B. Baath, *et al.*, Astron. Astrophys. **312**, 738 (1996b).

19. L. I. Matveenko, A. I. Witzel, and J. A. Zensus, in *Proceedings of the 182nd International Astronomical Union Colloquium, China, 2000.*
20. P. G. Mezger and A. P. Hendenson, Astrophys. J. **147**, 506 (1967).
21. H. Netzer, in *Astrophysical Jets and Their Engines, Ser. C: Mathematical and Physical Science,* Ed. by W. Kundt (D. Reidel, Dordrecht, 1987), p. 103.
22. F. T. Rantakyro, L. B. Baath, I. I. K. Pauliny-Toth, *et al.*, Astron. Astrophys. **259**, 8 (1992).
23. E. Ros, J. A. Zensus, and A. P. Lobanov, Astron. Astrophys. **354**, 55 (2000).
24. S. C. Unwin, M. H. Cohen, T. J. Pearson, *et al.*, Astrophys. J. **271**, 536 (1983).
25. S. C. Unwin and A. E. Wehrle, Astrophys. J. **398**, 74 (1992).

Translated by V. Astakhov

Astronomy Letters, Vol. 27, No. 11, 2001, pp. 691–702. Translated from Pis'ma v Astronomicheskiĭ Zhurnal, Vol. 27, No. 11, 2001, pp. 942–952.

Nuclear Activity of NGC 5548 from *UBVRI* Observations during 1990–2000

V. T. Doroshenko[1,*], V. M. Lyuty[1], N. G. Bochkarev[1], N. I. Merkulova[2], S. G. Sergeev[2], V. V. Vlasyuk[3], V. P. Mikhailov[3], O. I. Spiridonova[3], O. V. Ezhkova[4], K. N. Grankin[4], and S. Yu. Mel'nikov[4]

[1]*Sternberg Astronomical Institute, Universitetskiĭ pr. 13, Moscow, 119899 Russia*
[2]*Crimean Astrophysical Observatory, p/o Nauchnyĭ, Crimea, 98409 Ukraine, and Chilean Isaac Newton Institute, Crimean Branch*
[3]*Special Astrophysical Observatory, Russian Academy of Sciences, Nizhniĭ Arkhyz, Stavropolskiĭ Kraĭ, 357147 Russia*
[4]*Ulugbek Astronomical Institute, Academy of Sciences of Uzbekistan, Astronomicheskaya ul. 33, Tashkent, 700052 Uzbekistan*

Received May 15, 2001

Abstract—We present our $UBVRI$ observations of the nucleus of the Seyfert Galaxy NGC 5548 from 1990 until 2000 at four astronomical observatories: the Crimean Station of the Sternberg Astronomical Institute, the Special Astrophysical Observatory of the Russian Academy of Sciences, the Crimean Astrophysical Observatory (Ukraine), and the Mount Maidanak Observatory of the Ulugbek Astronomical Institute (Uzbekistan). All data have been reduced to a single system and are given for an $A = 14.3''$ aperture. Large light variations have been observed in the galactic nucleus over the last ten years: the total variability amplitude through the $A = 14.3''$ aperture was $1\overset{m}{.}8$, $1\overset{m}{.}4$, $0\overset{m}{.}94$, $0\overset{m}{.}65$, and $0\overset{m}{.}35$ in U, B, V, $R_{\rm J}$, and $I_{\rm J}$, respectively. The structure function of the variable component shows a power-law dependence on the time shift with the index $b \approx 0.7$. Treating the variability as a superposition of random outbursts with various durations and amplitudes is consistent with the observations. The maximum outburst duration inferred from the structure function is about 500 days. The best agreement between the observed and computed color–magnitude relations is achieved when the galaxy's brightness and color indices through the $A = 14.3''$ aperture are $V = 14.17, U - B = 0.23, B - V = 0.95, V - R_{\rm J} = 1.06, V - I_{\rm J} = 1.68$, while the colors of the variable component are, on average, $U - B = -1.10$, $B - V = 0.15$, $V - R_{\rm J} = 0.50$, $V - I_C = 0.75$, and they vary only slightly with its brightness. This implies that the outburst color indices are constant to a first approximation. However, there is evidence that the energy distribution of some outbursts differs from the average one. Some outbursts may exhibit enhanced ultraviolet and optical U radiation. © 2001 MAIK "Nauka/Interperiodica"

Key words: *active galactic nuclei, quasars, and radio galaxies*

1. INTRODUCTION

The Seyfert galaxy NGC 5548 is one of the best studied galaxies with active nuclei. Both ground-based facilities and satellites are used for its investigation. An intensive international monitoring of the NGC 5548 nucleus was performed from 1993 until 1998. However, interest in this galaxy has not waned. Therefore, systematically supplementing the existing photometric database with new observations seems to be of importance in studying both the long-term and short-term nuclear variability of this galaxy.

Systematic UBV photometry of NGC 5548 has been performed at the Crimean Station of the Sternberg Astronomical Institute (SAI) since 1968, and its regular $UBVRI$ observations have been carried out at Crimean Astrophysical Observatory since 1989. In 1990, the staff at Mount Maidanak Observatory of the Ulugbek Astronomical Institute (Uzbekistan) joined the observations with a $UBVR$ photometer using their telescopes, and patrol BVR observations of NGC 5548 with a CCD photometer have been carried out by the staff of the Special Astrophysical Observatory in the Caucausus since 1998.

Our objective was to collect together the $UBVRI$

*E-mail: doroshen@sai.crimea.ua

1063-7737/01/2711-0691$21.00

observations at these observatories from 1990 until mid-2000, reduce them to a single system, and perform an initial analysis of the data obtained.

2. OBSERVATIONS

Most of the photometric observations were carried out with photometers in which photomultipliers were used as the detectors. This yielded reliable photometric results in the spectral range 3600 to 10000 Å. The drawback of many CCD arrays is a low quantum efficiency in the ultraviolet. Therefore, photometers with photomultipliers are still more efficient than CCD photometers in the U band.

The observations at the Crimean Station of the SAI were carried out using a 60-cm Zeiss telescope mostly with a *UBV* pulse-counting photometer. The instrumental system was close to the standard photometric system of Johnson (1966). Each estimate was the sum of the photons accumulated in several (from 8 to 15) 10-s-long exposures. The rms error of each estimate for the nucleus of NGC 5548 through the $A = 14.3''$ aperture was, on average, $0^m.026$, $0^m.015$, and $0^m.022$ in U, B, and V, respectively. The comparison star during these observations was always star C from Lyuty (1972). Its $UBVR_J$ magnitudes are $U = 11.23 \pm 0.02$, $B = 10.98 \pm 0.02$, $V = 10.43 \pm 0.01$, and $R_J = 10.14 \pm 0.02$.

The observations with a thermoelectrically cooled ST-6 375 × 242-pixel CCD camera were performed on 14 nights. Below, the estimates obtained with this photometer appear with an abbreviation SAIc. The photometer is equipped with broadband filters that reproduce a $UBVRI$ system close to Johnson's standard photometric system. When a reducing lens is used, the CCD image scale is $1.8''$ per pixel. The instrumental field of view is $9.5' \times 7.2'$. Star ST1 from the list of comparison stars studied by Penston *et al.* (1971), which is commonly used as a comparison star during CCD observations, fell on one frame together with the galaxy. Its $BVRI$ magnitudes are given in Romanishin *et al.* (1995), and its U magnitude was taken as a mean of the data from Lyuty (1972) and Penston *et al.* (1971): $U = 14.48$, $B = 14.45$, $V = 13.76$, $R_C = 13.35$, and $I_C = 13.04$. The CCD images were processed with the software developed by Vlasyuk (1993). However, because the level of dark current in our camera was high and because it was impossible (for technical reasons) to sufficiently cool it, these observations have a low signal-to-noise ratio, so the mean error of a single estimate was $0^m.06$, $0^m.035$, and $0^m.023$ for the observations in B, V, and R, respectively.

The observations at Mount Maidanak High-Altitude Observatory in Uzbekistan (Mdn) were made using two 60-cm reflectors equipped with pulse-counting photometers. The photomultiplier was FEU-79. The measurements were obtained with standard $UBVR$ filters in Johnson's system through $24.2''$ and $26''$ apertures. The comparison star was star C. The observational errors were $0^m.034$, $\approx 0^m.016, 0^m.015$, and $0^m.017$ in U, B, V, and R, respectively. It is worth mentioning that the Observatory at Mount Maidanak is comparable in astroclimatic parameters to the world's best observatories (Ehgamberdiev *et al.* 2000).

The observations at the Special Astrophysical Observatory (SAO) in the Caucasus were occasionally carried out with a 1-m telescope but mostly with a 60-cm telescope (Zeiss-600) using a photometer with a liquid-nitrogen-cooled 1040×1160-pixel CCD array. The photometer is equipped with a set of broadband B, V, R, and I filters. The instrumental field of view on the Zeiss-600 telescope is $7.5' \times 8.5'$. Star ST1 mentioned above served as a comparison star. The galaxy's brightness was measured through $A = 10''$ and $15''$ apertures centered on the source's peak brightness. The mean measurement error in the magnitude of the nucleus through the $A = 10''$ aperture is $0^m.025$ in B and $0^m.021$ in V and R. Details on this instrument and on the observing technique and initial data reduction can be found in Amirkhanian *et al.* (2001).

The photometric observations at the Crimean Astrophysical Observatory (CrAO) were performed with a 1.25-m telescope (AZT-11) using a chopping photometer–polarimeter (Piirola 1973), which allows quasi-simultaneous measurements in five optical bands close to Johnson's $UBVRI$ system. During observations in the photometric mode, the instrument is a two-beam one: the sky background is also subtracted during an exposure. However, because the objective and background apertures are close (about 26 arcseconds), there is the risk of light from the outer parts of the galaxy falling on the background aperture. Therefore, when observing galaxies, the sky background was measured separately, at a distance of 7–8″ arcminutes from the galactic nucleus. An $A = 15''$ aperture was used. The observations were carried out by the method of differential photometry with respect to the comparison star using a check star. The comparison stars (C1 and C are the main and check ones, respectively) were taken from Lyuty (1972). The signal accumulation time on a single counter of each photomultiplier was 10 s. We made eight measurements for each object during one series of observations, from which we then calculated the means and rms deviations of a single measurement. Typically, they did not exceed $0^m.01$. The telescope is automatic, and an offset photoelectric guide is used in the observations. The accuracy of pointing at the

galaxy and subsequent guiding is 1/5 of the seeing or, in the worst case, it is ∼1 arcmin for 5″ seeing.

3. DATA REDUCTION

In general, at all four observatories (SAI, SAO, Mdn, and CrAO), the end product of the observations and their subsequent reduction are the series of internally homogeneous magnitude estimates for the nuclear region of NGC 5548. However, obtaining a single series that is as homogeneous as possible involves difficulties.

First, difficulties arise because the apertures used for the measurements at different observatories differ in size. Consequently, the galaxy's stellar radiation actually gave a different contribution to each of these series. To reduce all observations to the $A = 14.3''$ aperture, we used the surface-brightness distributions in the galaxy itself from Romanishin *et al.* (1995) and Doroshenko *et al.* (1998). The $A = 14.3''$ aperture was chosen because most of the observations were made in the Crimea using a UBV photometer with this aperture. The surface-brightness distribution given in Doroshenko *et al.* (1998) is based on multiaperture UBV photometry. Romanishin *et al.* (1995) obtained it by analyzing direct CCD images in B, V, R, and I. There is satisfactory (within the limits of the error measurements) agreement between these distributions in B and V. Below, we therefore used the surface-brightness distributions in B, V, R, and I from Romanishin *et al.* (1995), because they were traceable to much larger distances from the nucleus (from 1″ to 75″) and because they had smaller errors than those from Doroshenko *et al.* (1998). In U, in the range of distances 3″ to 60″ from the center, we took the surface-brightness distribution from Doroshenko *et al.* (1998). These surface-brightness distributions allow us to take into account the galactic contribution through different apertures and to reduce all observations to the $A = 14.3''$ aperture.

Second, despite the adaptation of the photometric systems of all the instruments used to Johnson's standard system, some differences still remain in practice. Therefore, we reduced the subsequent construction of a homogeneous UBV series to determining the coefficients of linear regression between the SAI series as the most complete and homogeneous one, on the one hand, and all the remaining series, on the other. This can be accomplished most reliably when there are many common dates of observations between different observatories. The regression coefficients in equations of the form

$$\mathrm{Mag(SAI)} = a\mathrm{Mag(CrAO, Mdn, SAO)} + b \quad (1)$$

are given in Table 1.

Table 1. Regression coefficients in Eqs. (1)

Mag		a	b	r	n
		CrAO			
U	(SAI)	0.854	1.720	0.92	21
B	(SAI)	1.151	−2.131	0.96	21
V	(SAI)	1.115	−1.515	0.95	24
		Mdn			
U	(SAI)	1.266	−3.578	0.97	16
B	(SAI)	1.023	−0.393	0.98	63
V	(SAI)	1.079	−1.118	0.98	17
R	(CrAO)	0.986	0.280	0.97	25
		SAO			
B	(SAI)	0.932	0.978	0.98	17
V	(SAI)	1.097	−1.292	0.96	24
R	(CrAO)	0.878	1.351	0.93	20

Since no R observations were carried out at the Crimean Station of the SAI and since there were few common dates of observations between CrAO and Mdn or between CrAO and SAO, we matched all R data by using the fact that there were many common dates of observations between the Crimean Station of the SAI and the Crimean Astrophysical Observatory. Therefore, based on these common dates between SAI and CrAO, we sought a correlation between the V (SAI) and R (CrAO) estimates. It turned out to be high ($r = 0.987$ for $n = 21$ coincident dates). As a result, we derived an equation for the transformation of SAI V magnitudes to CrAO R magnitudes: $R_J(\mathrm{CrAO}) = 0.688V(\mathrm{SAI}) + 3.347$. The new series of R magnitudes thus obtained was combined with the original CrAO R measurements. In this way, we obtained a more complete series of R data, to which the SAO and Mount Maidanak observations can be adjusted. Of course, this leads to a less reliable combination of the R data into a single light curve. The corresponding regression coefficients are given in Table 1.

Occasionally, we also used the I_J magnitude estimates obtained at the Crimean Astrophysical Observatory alone for our analysis. These magnitude estimates are few in number but span a long time interval. Since they were made with a 15″ aperture, we applied only an aperture correction to them.

The combined series of $UBVR_JI_J$ magnitudes for the nucleus of NGC 5548 through the $A = 14.3''$

Table 2. $UBVR_JI_J$ magnitudes of NGC 5548 through $A = 14.3''$

Date	JD2400000+	U	B	V	R_J	I_J	Obs.
Feb. 21, 1990	47944.522	13.94	14.49	13.77	–	–	SAI
Mar. 16, 1990	47967.348	14.17	14.63	13.88	–	–	SAI
Mar. 19, 1990	47970.499	14.20	14.66	13.83	–	–	SAI
Mar. 19, 1990	47970.513	14.03	14.60	13.85	–	–	SAI
Mar. 22, 1990	47973.422	14.21	14.59	13.88	–	–	SAI

apertures from 1990 until 2000 inclusive is given in Table 2.[1] Below, we give several rows from this table.

4. ANALYSIS

4.1. Macrovariability Parameters

Figure 1 shows the light curves since 1990. The filled and open circles indicate the SAI data and the data from all the remaining observatories, respectively. In addition, the dashed line represents the brightness of the stellar component of the galaxy itself through the $A = 14.3$ aperture. The continuum data at $\lambda = 5100$ Å, as obtained during an international monitoring of NGC 5548 (AGNWATCH) (www.astronomy.ohiostate.edu/~agnwatch/data.html), are represented by a thin line. These data were first recalculated to B and V magnitudes using formulas from Romanishin *et al.* (1995) and then reduced to the $A = 14.3''$ aperture. Note the excellent agreement of our B and V data with the AGNW data.

As the observations of NGC 5548 have been carried out at the Crimean Station of the SAI since 1969, we can compare the light curve at the beginning of these observations with the light curve for the last ten years. The historical U light curve is shown in Fig. 2. We see that, because the efforts of the four observatories were united in 1999–2000, the time resolution has significantly improved, and strong outbursts have been traced in more detail. The variability amplitude is largest in U and decreases from U to I. The total variability amplitude in magnitudes for 1969–2000 was $1\overset{m}{.}8$, $1\overset{m}{.}4$, $0\overset{m}{.}94$, $0\overset{m}{.}65$, and $0\overset{m}{.}35$ in U, B, V, R_J, and I_J, respectively. However, in none of these bands did the nuclear brightness reach the level of the underlying galaxy in this time. The lowest brightness of the nucleus was in 1996, 1998, and 1999.

Apart from outbursts, smoother light variations show up on long time scales. A simple examination of the U light curve (Fig. 2) indicates that the brightness, on average, rose between 1969 and 1980, and then there was a period of stabilization; subsequently, violent nuclear activity was observed.

To perform an initial analysis of the variability on long time scales, we calculated the mean flux density and the ratio of the corresponding standard deviations corrected for observational errors to the mean flux ($F_{\rm var} = std_{\rm var}(F)/\langle F\rangle$) for two intervals of observations: 1969–1989 and 1990–2000. These parameters are given in Table 3. Also given in this table are the maximum-to-minimum flux ratios ($R_{\rm max} = F_{\rm max}/F_{\rm min}$), which characterize the variability amplitude.

An analysis of Table 3 and an examination of Fig. 2 show that the mean flux density varies with time. The variability in the spectral range λ3600–7000 Å may not be a strictly stationary process, although it is close to it.

4.2. Structure Function

The subsequent analysis of our photometric data is performed with the structure function (SF). It can be used to study both stationary and nonstationary processes.

The structure function was introduced by Kolmogorov in 1941 (Rytov 1976) to analyze statistical problems associated with the turbulence theory. In astronomical practice, the structure function has been widely used to analyze time series since the study by Simonetti *et al.* (1985).

To bring the reader up to date, we briefly consider some properties of SF. Researchers mostly use the structure function only of the first order (SF_1), which for a random process $x(t)$, by definition, is a mathematical expectation of the square of the difference $x(t+\tau) - x(t)$, i.e.,

$$SF_1(\tau) = M[x(t+\tau) - x(t)]^2,$$

where τ is the time shift. For stationary processes, the structure function is uniquely related to the autocorrelation function by

$$SF_1(\tau) = 2D[x(t)] \times [1 - ACF(\tau)],$$

where $D[x(t)]$ is the dispersion of the process, and ACF is its autocorrelation function.

The slope of the autocorrelation function varies with shift. For sufficiently small time shifts, the process may be considered as a linear trend. In that case, $SF_1 \propto \tau^2$. On large time scales, the slope of SF_1 decreases, passing to $2D[x(t)]$ in the limit when $\tau \to \infty$, because on long time scales the random variables become statistically independent. Adding measurement errors to the process causes SF_1 to increase by

[1] Table 2 is published in electronic form only and is accessible via ftp cdsarc.u-strasbg.fr/pub/cats/J (130.79.128.5) or http://cdsweb.u-strasbg.fr/pub/cats/J.

Table 3. Variability parameters

Years	Band	$\langle F\rangle$, mJy	$F_{\rm var}$	$R_{\rm max}$	Years	Band	$\langle F\rangle$, mJy	$F_{\rm var}$	$R_{\rm max}$
1990–2000	U	8.707	0.35	5.32	1969–1990	U	9.672	0.32	5.01
	B	10.00	0 15	3.59		B	10.73	0.23	2.86
	V	14.01	0.12	2.37		V	14.53	0.15	2.07
	$R_{\rm J}$	23.77	0.12	1.82					
	$I_{\rm J}$	31.42	0.08	1.38					

$2D_{\rm err}$, where $D_{\rm err}$ is the dispersion of the observational errors. For a wide range of processes, there is a power-law dependence of SF_1 on time interval. Many processes can be represented as a superposition of a large number of pulses with a deterministic shape (shot noise). If the spectral density $P(f)$ increases as $1/f^{\gamma}$ with decreasing f, then such a process is called flicker noise. It is well known (Malakhov 1968) that a power-law power spectrum is obtained as a special case in the shot noise model. If γ takes on values from 1 to 3, then the structure function for such processes is $SF_1 \propto \tau^{\mathbf{b}}$, where $\mathbf{b}$ changes from 0 to 2 (Malakhov 1968). More complex structure function may correspond to actual processes.

Figure 3 shows the structure functions (SF_1) constructed on a logarithmic scale for the U, B, V, and $R_{\rm J}$ fluxes over the entire period of observations of this object since 1969. We calculated the structure functions by breaking down the time interval into equally spaced bins on a logarithmic scale and determined pairs of the times of observations $t_j > t_i$ for each bin in such a way that their difference $\tau = t_j - t_i$ was within a given bin; we then calculated

$$SF_1(\tau_k) = \sum_{j,i}[x(t_j) - x(t_i)]^2/n_k,$$

where n_k is the number of pairs in the kth bin. Each series of observations obtained in the Crimea, or in the Caucasus, or at Mount Maidanak, was broken down into bins of equal length, and the general structure function was calculated as a weighted mean of the structure functions from a separate series, while the weights were defined by the number of pairs in the kth bin from each series. Figure 3 clearly shows an upper plateau and an inclined line. The lower plateau attributable to observational errors on short time scales is indicated by the dashed line. All structure functions have a gap on times $\log\tau$ from -1 to 0. This is because there are no observations on time scales from 3 hours to 1 day in our data. This gap can apparently be filled only by organizing a collection of data from observing stations scattered all over the world, as was done during the international monitoring of NGC 5548 performed from 1993 until 1998. For comparison, the open circles in Fig. 3c indicate the structure function for NGC 5548 during 1988–1996, as inferred from the continuum data at $\lambda = 5100$ Å of the International Consortium AGNW, which were recalculated for the V band and the $A = 14.3''$ aperture.

Our comparison suggests that the V structure functions in the linear part, as inferred from our and the AGNW data, are similar. According to the AGNW data, SF_1 is well filled on time scales from 2 hours to 1 day. The international monitoring data reach the lower plateau at the observational error level even for $\tau < 1$ days.

The main parameters of the structure function derived from our data (slope and correlation coefficient) for various time delays are given in Table 4.

Let us first consider the structure function on large time scales. In the U, B, V, and R bands, a similarity can be noted between SF_1 on time scales $1 < \tau < 1000$ days. As we see from Fig. 3, when passing from U to R, the inclined part of the structure function becomes increasing less smooth. The absence of SF_1 smoothness in R can be attributed in part to data incompleteness. However, although the V data are most complete and accurate, the structure function in V is, nevertheless, less smooth than that in U. The slopes b of the logarithm of the structure function in all spectral bands are close, within the error limits: $b = 0.73 \pm 0.02$ in U and $b = 0.66 \pm 0.03$ in R. There may still be a tendency for the slope to decrease when passing from U to R. An interesting feature of the derived structure functions is a turnover on time scales $\log\tau \approx 2.7$. The time scale that corresponds to reaching the upper plateau in all structure functions is $\sim$500 days. It determines the maximum time scale when the flux variations are still correlated.

The structure function on time scales from 10 min to 2.5 hours is clearly not a continuation of the structure function on time scales larger than 1 day. For small time scales, the slope b of the structure function in U and B is nearly zero. In V, although it passes above the observational errors, its slope is $b \sim 0.33$ for the correlation coefficient $r = 0.77 \pm 0.10$. In R, the slope of the structure function is $b \sim 0.28$ for the correlation coefficient $r = 0.49 \pm 0.18$. However, in all bands, the structure function on small time scales

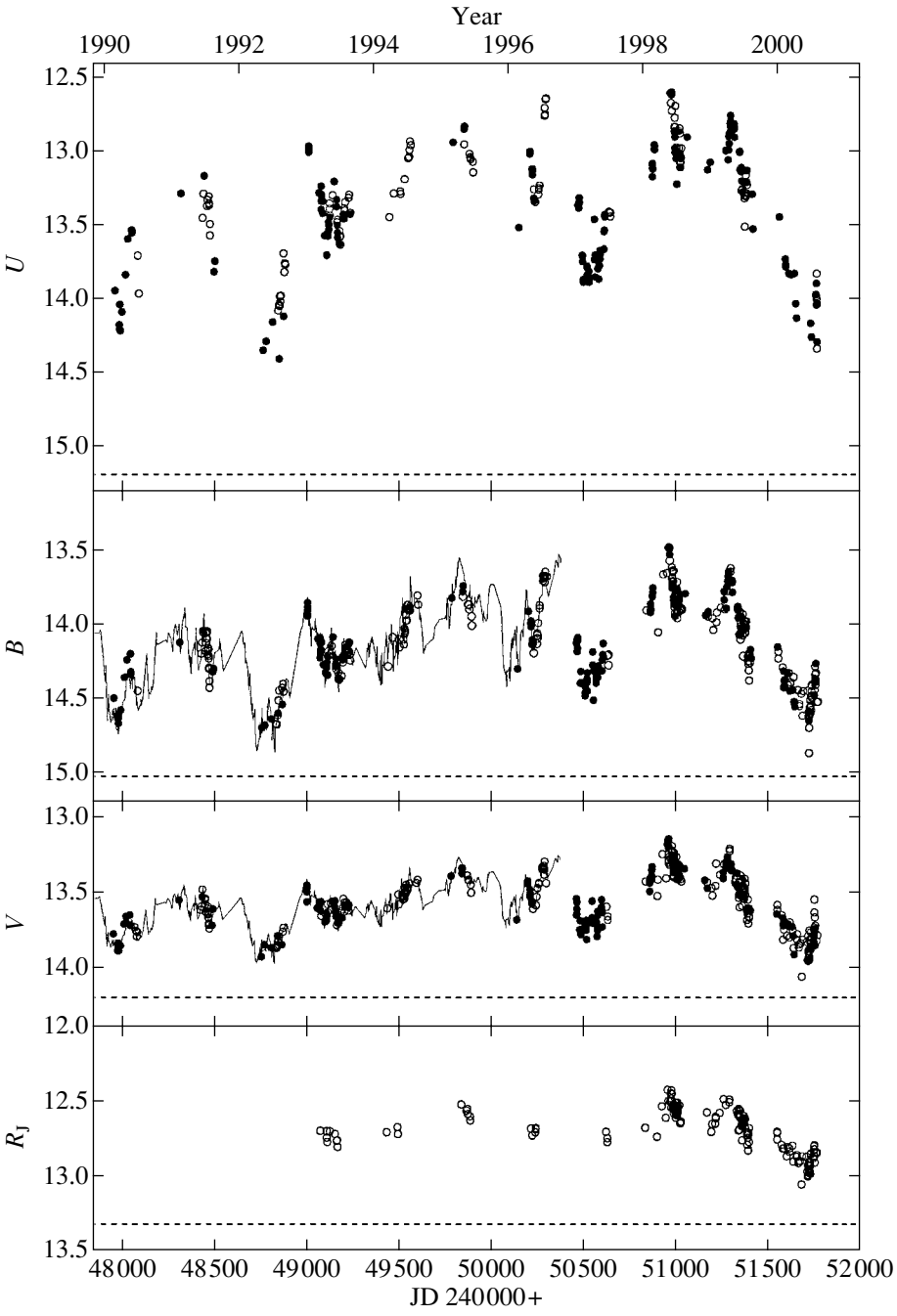

Fig. 1. $UBVR_J$ light curves of NGC 5548 through the $A = 14.3''$ aperture. The filled and open circles represent the SAI observations and the observations at the other observatories, respectively. The dashed line indicates the galaxy's brightness through the $A = 14.3''$ aperture.

passes above the line attributable to the observational errors. The excess is, on average, $(1.8–1.6)\sigma$. On small time scales, we may have to do with a random process of a slightly different nature than that characteristic of long time delays.

4.3. Analysis of Color–Magnitude Relations

The observed $U - B$, $B - V$, $V - R$, and $V - I$ color indices correlate with brightness variations: on average, they decrease when the object becomes brighter. It would be natural to explain such dependencies by an increasing role of the parent galaxy with decreasing brightness of the variable component in the nucleus and by the fact that the color indices of

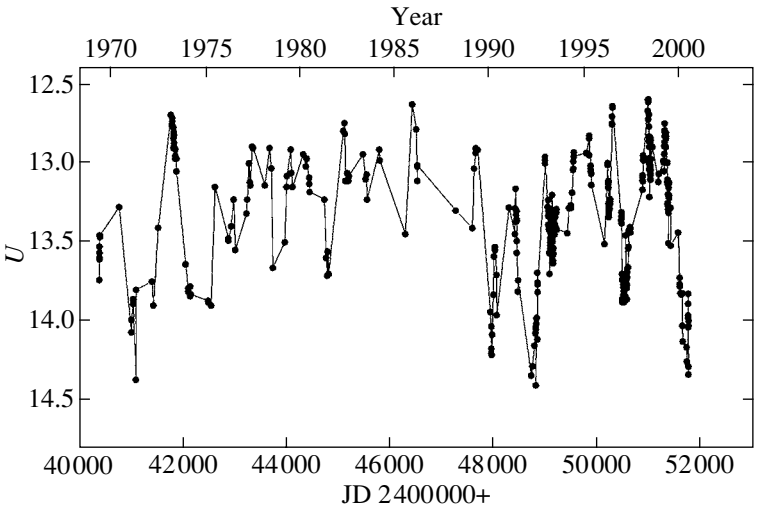

Fig. 2. Light curve of NGC 5548 through the $A = 14.3''$ aperture over the entire period of photoelectric observations at Crimean Station of the SAI.

the galaxy are appreciably larger than those of the variable source. It is worth noting that such a dependence manifests itself in the $U - B$ color only for $V > 13^m.6$, i.e., when the object becomes faint. Since the observed $U - B$ color index remains, on average, at the $U - B = -0.9$ level when the V magnitude changes from $13^m.1$ to $13^m.6$, this means that the corresponding color index of the variable source varies little with its brightness, because its contribution dominates in a bright state. Since the galactic color index begins to dominate in a faint state, the total color index increases starting from some level when the brightness of the variable source decreases even if its color index is constant.

Bearing in mind the possible constancy of the color indices of the variable component as its brightness varies, we can estimate $U - B$, $B - V$, $V - R$, and $V - I$ of the variable component averaged over the entire data set even without any knowledge of the galactic contribution to the total flux. Such estimates are usually made by analyzing the slopes of the regression lines in flux–flux diagrams in two different bands. The slope of the straight line gives the flux ratio in the two color bands. Using the equation for the transformation of magnitudes to fluxes, according to the absolute calibration by Johnson (1966), we determined the color indices: $U - B = -1.10 \pm 0.01$, $B - V = 0.09 \pm 0.01$, $V - R_J = 0.48 \pm 0.02$, and $V - I_J = 0.81 \pm 0.06$.

Thus, we know the galactic fluxes (in mJy) through the $A = 14.3''$ aperture ($FU = 1.535$, $FB = 4.204$, $FV = 7.644$, $FR_J = 13.165$, and $FI_J = 19.684$), as inferred from the data of Romanishin *et al.* (1995) and Doroshenko *et al.* (1998). In addition, we know the color index of the variable component. Consequently, we can calculate the expected (in observations) dependence of color indices on the V magnitude for the total flux through the $A = 14.3''$ aperture and compare it with the observed dependence, which is shown in Fig. 4. To simplify the figure, the filled circles indicate the observational data averaged over small bins of V magnitudes. The vertical and horizontal bars near each circle correspond to the standard deviations in the distribution of data in each bin in V. The thin solid line represents model 1 for the above fluxes from the galaxy and the color indices of the variable component. This model satisfactorily describes only the observed variations of $U - B$ with V. The calculated variations in the other color indices disagree with the observations: the thin solid line lies above the observed values. However, as follows from experience and from the aperture magnitudes of NGC 5548 from Romanishin *et al.* (1995), the galaxy's magnitudes are determined with a large error, particularly through a small aperture such as we used. Therefore, we considered other models with galactic fluxes deviating by 15–25% from the above values. The situation with $B - V$, $V - R_J$, and $V - I_J$ significantly improved when,

Table 4. Parameters of the structure function

Band	9 min–2.5 hours			1.4–900 days		
	b	σb	r	b	σb	r
U	−0.16	0.32	−0.15	0.72	0.02	0.98
B	0.10	0.09	0.28	0.69	0.02	0.98
V	0.33	0.07	0.77	0.65	0.03	0.96
R_J	0.28	0.11	0.49	0.66	0.03	0.96

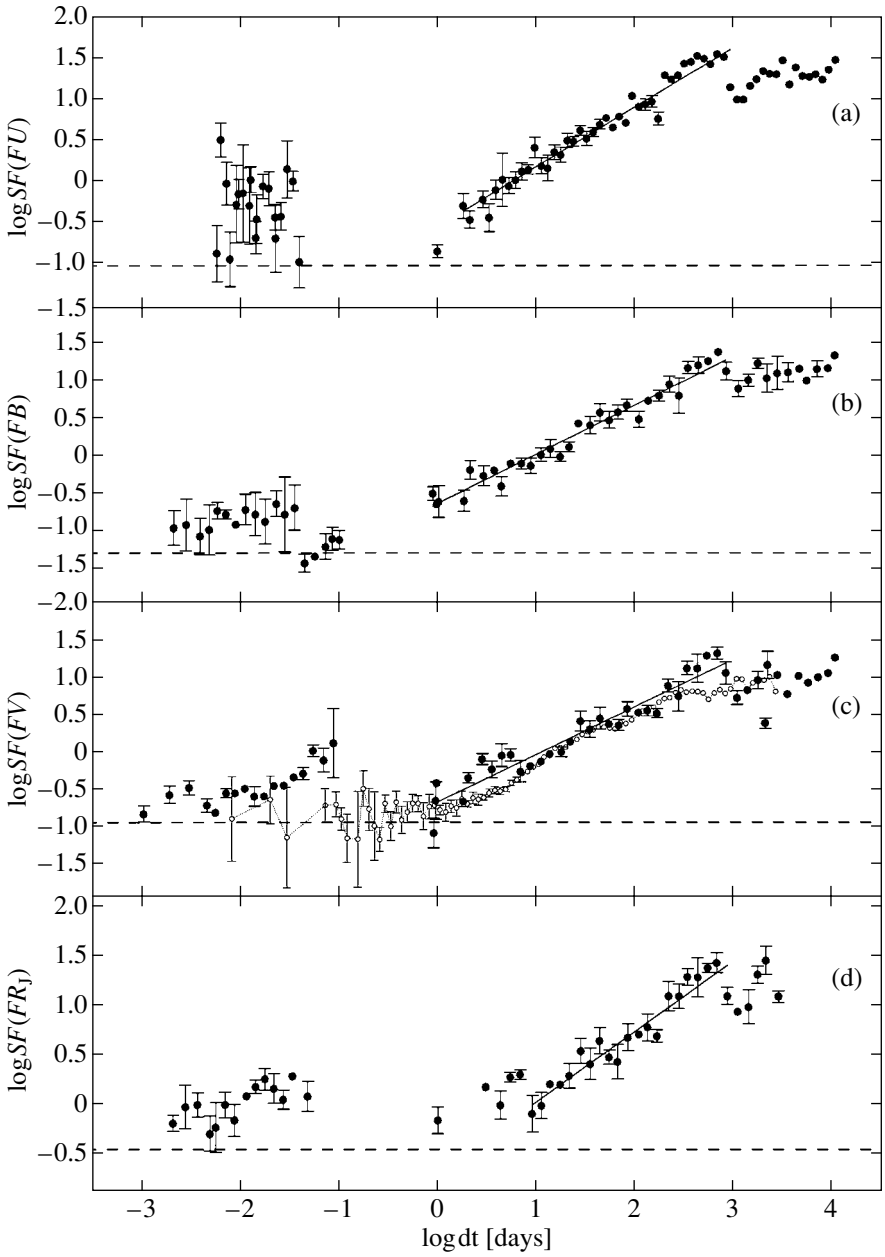

Fig. 3. Structure function for the variable flux from the NGC 5548 nucleus: our data are represented by the filled circles, and the AGNWATCH V data are represented by the open circles.

for the same color indices of the variable source, we took galactic fluxes that were 25% lower in U and B than the values considered in model 1 and that were 20 and 15% higher in R and I (model 2). In the figure, this model is indicated by the dotted line. In Fig. 4b, the dotted line coincides with the heavy solid line. Moreover, the calculated values become quite satisfactory if we slightly change the color indices of the variable component and take them to be equal: $U - B = -1.02$, $B - V = 0.09$, $V - R_J = 0.50$, and $V - I_J = 0.75$ (model 3). In Fig. 4, model 3 is represented by the heavy solid line. Model 4, where the galactic flux in U and B differs from the initially assumed flux by a mere 15 and 10%, is also in satisfactory agreement with the observations. Model 4 is even in slightly better agreement with the observations than model 3, given that the color indices of the galactic component ($B - V = 0.95$, $V - R_J = 1.06$, and $V - I_J = 1.68$) correspond more closely to elliptical galaxies. Recall that, according to the study by Romanishin *et al.* (1995), the galaxy NGC 5548 has a huge bulge with an effective radius of $\approx 7''$. Parameters of the galaxy and the variable

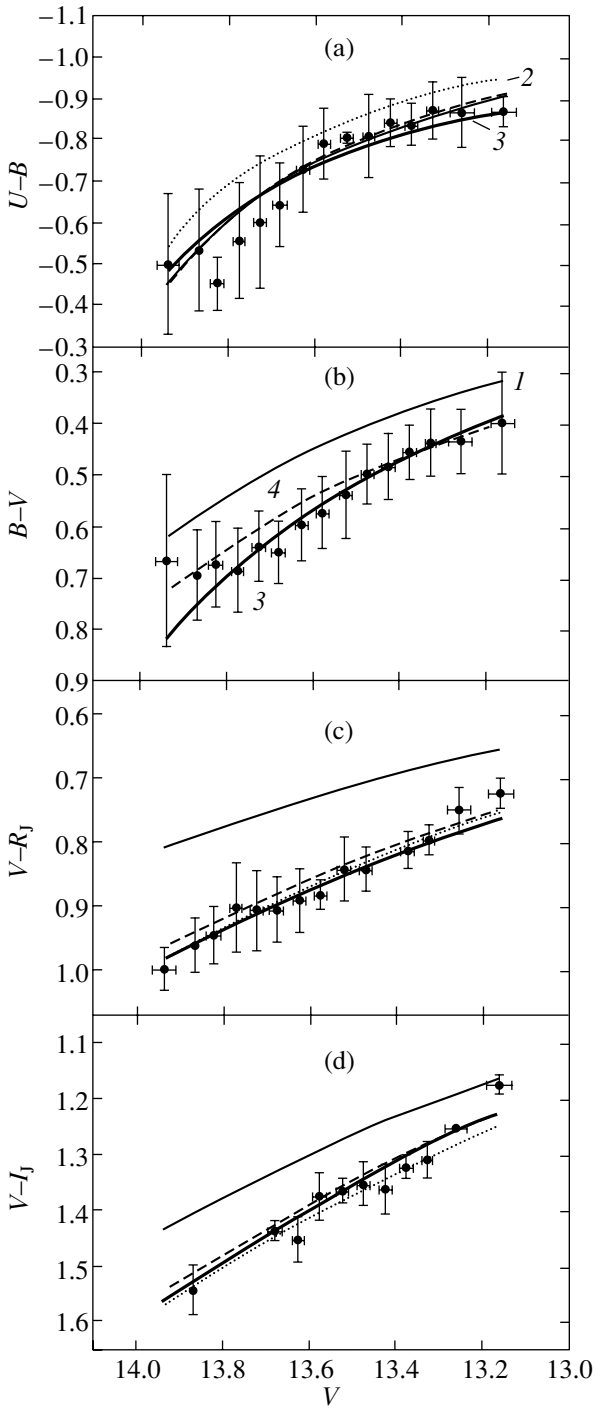

Fig. 4. Comparison of the observed color–magnitude relations binned in V with the calculated ones. The filled circles represent the observed values. Different lines indicate different models (1–4), whose parameters are given in Table 6.

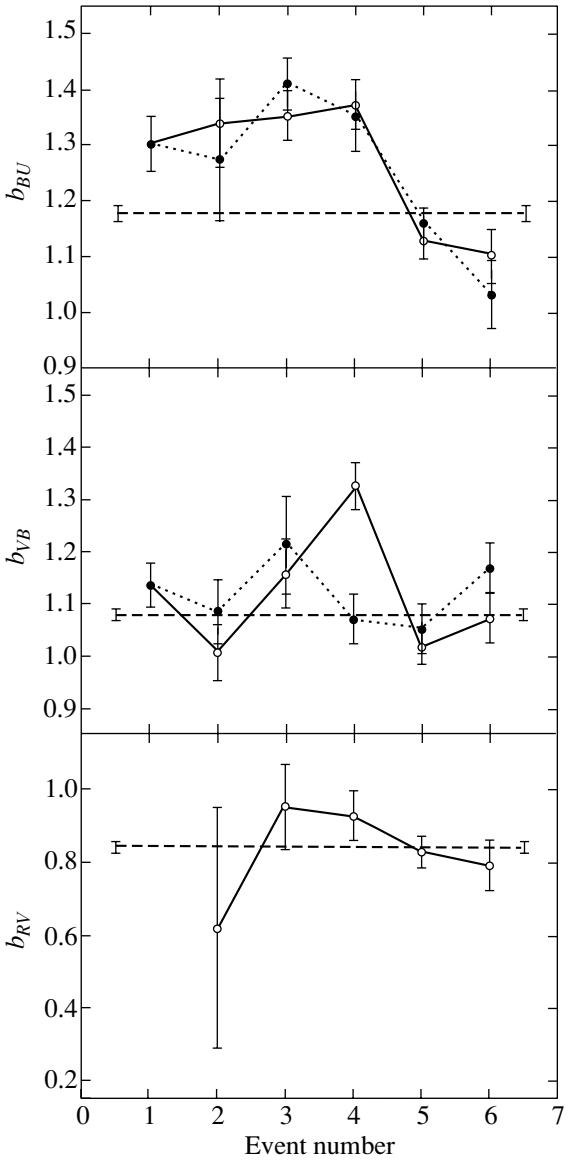

Fig. 5. Parameters of the slopes of the regression lines in flux–flux diagrams for six major events.

component for all the models considered are given in Table 5.

Thus, analyzing the observed color indices and their correlation with variations in the total brightness, we concluded that the colors of the variable sources are, on average, $U-B=-1.06\pm0.04$, $B-V=0.09\pm0.01$, $V-R_{\rm J}=0.48\pm0.02$, and $V-I_{\rm J}=0.75\pm0.02$, while the galaxy's magnitudes through the $A=14.3''$ aperture are $U=15.35$, $B=15.12$, $V=14.17$, $R_{\rm J}=13.43$, and $I_{\rm J}=12.87$. The small difference in $B-V$ presented here and in Lyuty and Doroshenko (1993), who gave $B-V=-0.01\pm0.02$, results from using different calibrations when transforming fluxes to magnitudes.

4.4. The Color Indices of Individual Major Events

According to our analysis in the previous section, we took the color indices for the variable component

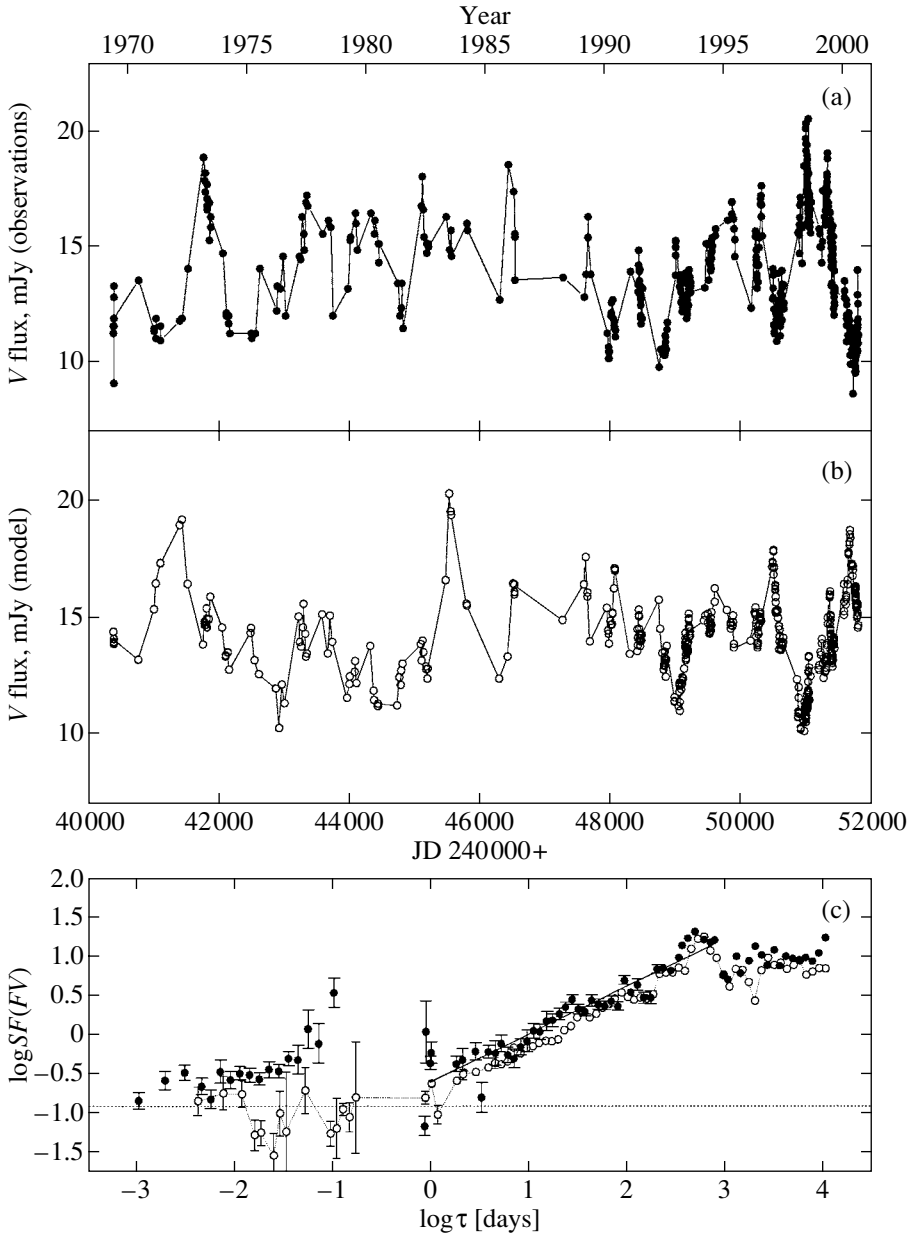

Fig. 6. (a) The observed V light curve and (b) a realization of a random process as a superposition of independent outbursts when the number of outbursts depends on duration as a power law with the index $\alpha = -1.6$ and the outburst amplitudes depend on duration as a power law with the index $\beta = 0.2$. (c) The structure functions for the observed (filled circles) and modeled (open circles) processes.

averaged over the entire data set and assumed them to be constant as the brightness varied. However, it is by no means obvious that individual characteristic events on the light curve that may be associated with strong outbursts have the same color characteristics. Let us consider the flux–flux relation for some of such events. For the regression coefficients to be reliably calculated, these events must cover sufficiently large light variations on a small time scale. For our analysis, we chose six events:

no. 1—Mar. 1972–Apr. 1974 (JD 2441392–2149), no. 2—Feb. 1990–Aug. 1991 (JD 2447944–8483), no. 3—May 1992–Apr. 1993 (JD 2448745–9108), no. 4—Feb. 1996–Feb. 1997 (JD 2450139–50491), no. 5—Mar. 1997–Aug. 1998 (JD 2450522–51052), and no. 6—Jan.–Aug. 1999 (JD 2451197–51408).

For them, we calculated the slopes of the straight lines (b_{BU}, b_{VB}, b_{RV}) in the FB–FU, FV–FB, and FR–FV planes. The results are presented in Fig. 5, in which the open circles indicate the slopes and

Table 5. Galactic fluxes through the $A = 14.3''$ aperture and the color indices of the variable component for various model color–magnitude relations.

Model	Galaxy, fluxes in mJy					Variable component			
	FU	FB	FV	FR_J	FI_J	$U-B$	$B-V$	$V-R_J$	$V-I_J$
1	1.535	4.204	7.644	13.165	19.684	−1.10	0.09	0.48	0.81
2	1.151	3.153	7.644	15.798	22.637	−1.10	0.09	0.48	0.81
3	1.151	3.153	7.644	15.798	22.637	−1.02	0.09	0.50	0.75
4	1.305	3.784	7.797	15.798	22.637	−1.10	0.15	0.50	0.75

their errors calculated from the combined data of the four observatories, and the filled circles indicate the corresponding coefficients calculated from the SAI data alone. The dashed line represents the same coefficients simultaneously for the entire data set. We see from the figure that the slopes of the straight lines in the FR–FV and FV–FB planes for individual events are equal, within the error limits, to the mean and to each other. In the FB–FU plane, however, some slopes of the straight lines significantly differ from the mean and from each other. Thus, for example, events nos. 3 and 4 significantly differ in slope b_{BU} both from the mean and from the corresponding values for events nos. 5 and 6. This means that the energy distribution in events nos. 3 and 4 is enhanced in the ultraviolet compared to the energy distribution in events nos. 5 and 6 or compared to the average spectrum of the variable component. Several bluer outbursts may be involved in events nos. 3 and 4.

5. DISCUSSION

The jaggedness of the light curves for the nuclei of Seyfert galaxies has prompted researchers to consider them in terms of a shot noise model as a superposition of independent outbursts whose duration has a power-law distribution (Terebizh *et al.* 1989; Sergeev 1999). Under certain conditions imposed on the outburst amplitude and duration, this process may result in the first-order structure function being a power law with an index b from 0 to 2. It has emerged that the outburst shape is of no importance if only it has no singularities; i.e., the derivative of the outburst shape must be bounded. Sergeev (1999) showed that if the number of outbursts per unit time of duration ω depend on duration as a power law, i.e., $n(\omega) \sim \omega^{\alpha}$, and if the outburst amplitudes also depend on duration as a power law, i.e., $A(\omega) \sim \omega^{\beta}$, then the structure function would also tend to a power law depending on interval τ with index $b = \alpha + 2\beta + 2$, i.e., $SF_1 \rightarrow \tau^{\alpha + 2\beta + 2}$.

We modeled such a process for various α and β, as applied to the available actual epochs of observations and taking into account the fact that the observed structure function on a logarithmic scale had the slope $b = 0.7$. In this case, we assumed that, first, the outburst amplitude decreased with decreasing outburst duration, i.e., $\beta > 0$, and, second, there were physical constraints on the burst duration, i.e., a power-law distribution of outbursts took place in some range of durations, $\omega_{\min} < \omega < \omega_{\max}$. Thus, there were simply no outbursts with a duration outside this range. Figure 6b shows a typical realization of a random process with $\alpha = -1.6$ and $\beta = 0.2$. In this case, the mean time interval between two sequences of outbursts was taken to be $dt = 0.01$ days, i.e., the outbursts significantly overlapped. $\omega_{\min} = 0.001$ days and $\omega_{\max} = 300$ days are close to the observed values. When treating the nuclear variability of active galaxies as a superposition of outbursts with various amplitudes and durations, the maximum time interval of the correlated variations inferred from observations may be considered to be the maximum outburst duration. Recall that the maximum interval of the correlated flux variations was found from observations to be ~500 days. Taking the above range of outburst durations allowed us to obtain features on the modeled light curve that were close in duration to the observed ones. Modeling the process with $\omega_{\max} \approx 50$–100 days did not give the prolonged brightness rises or declines on the light curves that were actually observed. For comparison, Fig. 6a shows the observed V light curve. Figure 6c illustrates the structure functions for the observed light curve (filled circles) and for the modeled light curve with noise corresponding to observational errors of 2% superimposed (open circles). The observed error is indicated in the figure by the dotted line. As we see from a comparison of the model and the observations, the model light curve is generally similar to the observed one in light-curve jaggedness and in amplitude and duration of strong outbursts. The structure functions for these light curves coincide. We can thus conclude that our assumptions about a power-law dependence of the amplitude on duration and about a power-law distribution of outburst durations are quite real. We cannot completely rule out the possibility that a shot- or flicker-noise process

takes place in the observed nuclear variability of active galaxies. Previously, Terebizh *et al.* (1989) reached a similar conclusion by analyzing the power spectrum for optical brightness variations in the nucleus of the Seyfert galaxy NGC 4151.

6. CONCLUSIONS

Summarizing the results of our study of the photometric variability in NGC 5548, we can say that in more than 30 years, the total variability amplitude through the $A = 14.3''$ aperture has been $1^m.8$, $1^m.4$, $0^m.94$, $0^m.65$, and $0^m.35$ in U, B, V, R_J, and I_J, respectively.

On time scales of ~ 1 days, an additional variability with almost the same amplitude in all bands, $\sim 0^m.1$–$0^m.08$, is apparently observed in some cases.

The structure function of the variable component exhibits a power-law dependence on the time shift with an index of $b \approx 0.7$, suggesting that the observed variability is similar to noise. A more specific analysis of this issue indicates that the view of the photometric variability in active galactic nuclei as a superposition of random outbursts with various durations and amplitudes (shot noise) is consistent with the observations. The maximum outburst duration determined from the structure function is about 500 days.

The agreement between the observed and computed color–magnitude relations is best when the galaxy's brightness and color indices through the $A = 14.3''$ aperture are $V = 14.17$, $U - B = 0.23$, $B - V = 0.95$, $V - R_J = 1.06$, and $V - I_J = 1.68$, which correspond to $V - R_C = 0.74$ and $V - I_C = 1.31$ in Cousins's system. These color indices are close to those for elliptical galaxies, which confirms the conclusion by Romanishin *et al.* (1995) that the effective radius of the bulge in this galaxy is very large ($R_{eff} \approx 7''$). The color indices of the variable component vary little with its brightness and are, on average, $U - B = -1.10$, $B - V = 0.15$, $V - R_J = 0.50$, and $V - I_J = 0.75$ (or $V - R_C = 0.34$ and $V - I_C = 0.58$ in Cousins's system).

In light of our treatment of the nuclear variability as a superposition of random outbursts, the constancy of the color indices of the nucleus as its brightness varies may imply (to a first approximation) the constancy of the outburst color indices. However, there is evidence that the energy distribution of some outbursts differs from the average one. Some outbursts may have enhanced ultraviolet radiation.

7. ACKNOWLEDGMENTS

Most authors were supported in part by the INTAS (grant no. 96-0328) and the Russian Foundation for Basic Research (project no. 00-02-16272). N.I. Merkulova and S.G. Sergeev were supported in part by the American CRDF grant no. UP1-2116. N.G. Bochkarev also wishes to thank the Russian Foundation for Basic Research and the State Foundation for Natural Sciences for financial support (project no. 99-02-39120).

REFERENCES

1. V. R. Amirkhanian, N. A. Vikul'iev, V. V. Vlasyuk, and J. A. Stepanian, Bull. Spec. Astrophys. Obs. **50** (2001) (in press).
2. V. T. Doroshenko, V. M. Lyuty, and V. I. Shenavrin, Pis'ma Astron. Zh. **24**, 197 (1998) [Astron. Lett. **24**, 160 (1998)].
3. V. T. Doroshenko, V. M. Lyuty, N. G. Bochkarev, *et al.,* Pis'ma Astron. Zh. **27**, 83 (2001) [Astron. Lett. **27**, 65 (2001)].
4. S. A. Ehgamberdiev, A. K. Baijumanov, S. P. Ilyasov, *et al.,* Astron. Astrophys., Suppl. Ser. **145**, 293 (2000).
5. H. L. Johnson, Annu. Rev. Astron. Astrophys. **4**, 193 (1966).
6. V. M. Lyuty, Astron. Zh. **49**, 930 (1972) [Sov. Astron. **16**, 763 (1972)].
7. V. M. Lyuty and V. T. Doroshenko, Pis'ma Astron. Zh. **19**, 995 (1993) [Astron. Lett. **19**, 405 (1993)].
8. A. N. Malakhov, *Fluctuations in Self-oscillatory Systems* (Nauka, Moscow, 1968).
9. M. J. Penston, M. V. Penston, and A. Sandage, Publ. Astron. Soc. Pac. **83**, 783 (1971).
10. V. Piirola, Astron. Astrophys. **27**, 373 (1973).
11. W. Romanishin, T. J. Balonek, R. Ciardullo, *et al.,* Astrophys. J. **455**, 516 (1995).
12. S. M. Rytov, *An Introduction to Statistical Radiophysics* (1976).
13. S. G. Sergeev, Candidate's Dissertation (Krymsk. Astrofiz. Obs., Crimea, 1999).
14. J. H. Simonetti, J. M. Cordes, and D. S. Heeschen, Astrophys. J. **296**, 46 (1985).
15. V. Yu. Terebizh, A. V. Terebizh, and V. V. Biryukov, Astrofizika **31**, 75 (1989).
16. V. V. Vlasyuk, Astrofiz. Issled. **36**, 107 (1993).

Translated by V. Astakhov

Astronomy Letters, Vol. 27, No. 11, 2001, pp. 703–711. Translated from Pis'ma v Astronomicheskiĭ Zhurnal, Vol. 27, No. 11, 2001, pp. 942–952.

Photometric and Spectrophotometric Observations of the Classical Symbiotic Star YY Her during Its Return to Quiescence

A. A. Tatarnikova[1, *], V. F. Esipov[1], E. A. Kolotilov[1], J. Mikolajewska[2], U. Munari[3], and S. Yu. Shugarov[1]

[1] *Sternberg Astronomical Institute, Universitetskii pr. 13, Moscow, 119899 Russia*
[2] *Copernicus Astronomical Center, Warsaw, Poland*
[3] *Padoa Astronomical Observatory, Asiago, Italy*

Received May 14, 2001; in final form June 22, 2001

Abstract—We present new photometric *UBVRI* and spectroscopic observations of the symbiotic star YY Her during its return to quiescence after a strong outburst in 1993. High-resolution spectra of YY Her at similar phases at outburst maximum ($\varphi = 0.48$) and in quiescence ($\varphi = 0.37$) are presented for the first time. The ephemeris of YY Her has been refined ($P = 586^{\rm d}$). The last two observed minima (in 1999 and 2000) differed radically in shape from the 1997 minimum described previously. Both were sharp and deep ($\Delta U \sim 1\overset{m}{.}6$, $\Delta V \sim 0\overset{m}{.}9$). To explain this shape of the V light curve, which is only slightly affected by nebular emission, it should be assumed that the cool component of YY Her fills much of its Roche lobe and has a hot spot on the hemisphere facing the hot component. The emission spectrum rich in Fe II lines, which is characteristic of symbiotic stars, was observed during the outburst, but high-ionization lines (He II λ4686) were also observed. The He I $\lambda\lambda$5876, 7065 lines exhibit distinct P Cyg profiles; the centers of the absorption components are shifted from the emission ones by $V_r \approx 100$ km s^{-1}, suggesting moderate outflow velocities. © 2001 MAIK "Nauka/Interperiodica"

Key words: *symbiotic stars*

INTRODUCTION

The symbiotic star YY Her has been observed photographically and visually since 1890. A detailed analysis of its light curves by Munari *et al.* (1997a) revealed a periodicity in the visual band with $P = 590^{\rm d}$ and amplitude $0\overset{m}{.}3$. These authors also pointed to the existence of several points at phases near the minimum during which the visual brightness was abnormally low. However, they failed to reach a correct conclusion about the actual variability amplitude because of the scarcity of observations and the large number of missed minima.

In quiescence, the ultraviolet + optical spectrum of YY Her can be satisfactorily interpreted in terms of a three-component model composed of a cool component, a gaseous nebula, and a hot component. In most studies, the hot component of YY Her in quiescence is a subdwarf with a temperature of $\sim 10^5$ K [see Munari *et al.* (1997b) and references therein]. The cool component of YY Her at minimum light was classified by optical TiO molecular bands as a red giant of a spectral type slightly later than M4. Based on the depths of near-infrared TiO bands, Murset and Schmid (1999) obtained a similar spectral type.

As in all classical symbiotic stars, nova-like outbursts have been observed in YY Her. Munari *et al.* (1997a) detected four outbursts in its visual and photographic light curves. The last strong outburst occurred in 1993 (Munari *et al.* 1997b). It was concluded from optical and ultraviolet observations that the spectral energy distribution for the hot component during outbursts could not be represented by a single Planck function (which can be done with satisfactory accuracy for the star in quiescence). In the near ultraviolet, an additional radiation source whose energy distribution is similar to the spectrum of a blackbody with a temperature of $\sim$15000 K and whose luminosity at maximum light accounts for <20% of the hot component's luminosity contributes significantly to the total flux.

In quiescence, the hot and cool components have approximately equal luminosities, while at the maximum of the 1993 outburst, the bolometric flux from the hot component rose by almost an order of magnitude (from 1.3×10^{-9} to 12.2×10^{-9} erg cm^{-2} s^{-1}).

* E-mail: aat@sai.msu.ru

1063-7737/01/2711-0703$21.00

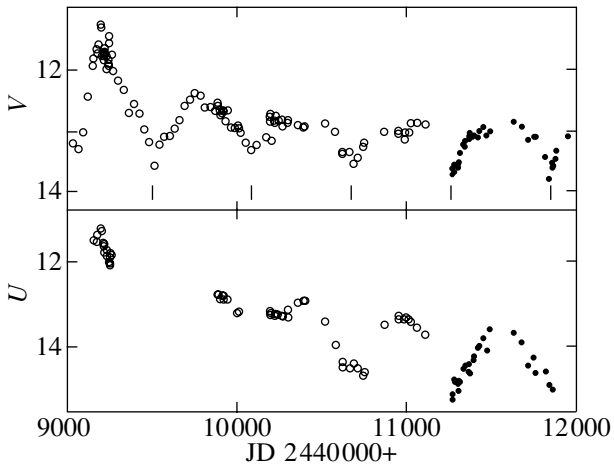

Fig. 1. U and V light curves for YY Her. The open circles represent data from Tatarnikova *et al.* (2000). The filled circles represent our data. The vertical bars near the horizontal axis for the V band mark the dates of minima.

This behavior does not fit into the thermonuclear-flash model, in which a hot subdwarf evolves into an A–F supergiant with the bolometric flux changing only slightly (Mikolajewska and Kenyon 1992).

We extended our photometric and spectroscopic observations to cover the star's quiescent state, which allowed us not only to refine the ephemeris, but also to reach definitive conclusions regarding the red giant's light curve and the complex structure of the nebula around the hot component of YY Her. In the case of symbiotic stars, one of the most important questions is the nature of the cool component, because the various models for the quiescent and active states of symbiotic stars are based on this or, to be more precise, on the cool component's mass-loss rate.

OBSERVATIONS

Tables 1 and 2 give photoelectric *UBVRI* observations of YY Her. The observations are being carried out with a 0.6-m telescope at Crimean Station of the Sternberg Astronomical Institute (SAI); their errors do not exceed $0\overset{m}{.}03$. The magnitudes of the standard star HD 168957 are $U = 6\overset{m}{.}35$, $B = 6\overset{m}{.}91$, and $V = 7\overset{m}{.}01$. The star that Munari *et al.* (1997a) designated as G on the finding chart was chosen as the standard; its magnitudes are $V = 13\overset{m}{.}08$, $R = 12\overset{m}{.}44$, and $I = 11\overset{m}{.}94$. Figure 1 shows the U and V light curves for YY Her constructed by using previously published data (see Tatarnikova *et al.* 2000)

Spectroscopic observations of YY Her in the range 4000–7500 Å with a dispersion of 8 Å/pixel are being carried out with a 1.25-m telescope at the Crimean Station of the SAI. The two spectra taken on August 4, 2000 ($\varphi = 0.85$), and October 4, 2000 ($\varphi = 0.95$), are similar to the August 21, 1997 spectrum ($\varphi = 0.01$) described previously by Tatarnikova *et al.* (2000), but the line fluxes are slightly weaker, as is the flux beyond the Balmer jump estimated from the U magnitude (Min $= 2451848 + 586^{\mathrm{d}}E$). Table 3 gives the emission-line fluxes determined by fitting the line profile with a Gaussian.

High-resolution (0.2 Å/pixel) spectra were taken with the 1.8-m Padoa Astronomical Observatory telescope (Italy) on August 1, 1993, at maximum light during the strong 1993 outburst [three days before, a low-resolution spectrum was obtained; it was used by Munari *et al.* (1997a, 1997b) to determine the components' physical parameters) and on October 28, 1999, in quiescence. Since the latter spectrum was underexposed, the equivalent widths for lines with wavelengths shorter than for Hα could not be accurately determined. Five-point smoothing was applied to all spectra. Table 4 lists laboratory wavelengths of the identified lines, their radial velocities, FWHMs, and equivalent widths.

In quiescence, only lines of hydrogen and singly ionized helium can be identified in a high-dispersion spectrum. The absence of the [O III] 4959 and 5007 lines may result not only from decline in the activity of the hot component of YY Her, but also from underexposure.

During the outburst, a high-resolution spectrum exhibits a large number of Fe II emission features (see Fig. 2a), which is typical of most symbiotic stars during their outbursts. However, in contrast to classical symbiotic stars, such as, for example, BF Cyg (Cassatella *et al.* 1992), the hot component of YY Her proved to be hot enough for the He II λ4686 line to be present in the spectrum even in its active state (see Table 4).

Figure 2b shows the Hα profiles during the outburst and in quiescence. Both spectra were taken at similar phases, but the star was 3^m brighter in U on August 1, 1993 ($\varphi = 0.48$), than on October 28, 1999 ($\varphi = 0.37$). The line profile has a complex, asymmetric shape even in quiescence. During the outburst, the red Hα wing was most broadened; this wing extended to velocities of 1300 km s^{-1}, while in quiescence, it extended to a mere 500 km s^{-1}. For comparison, Fig. 2c shows the Hα profile of the symbiotic star AS 338, which exhibits a distinct P Cyg profile. In the case of YY Her, a P Cyg profile is observed for the He I $\lambda\lambda$5876,7065 lines (see Fig. 2d), whose absorption components lie at $V_r \approx -130$ km s^{-1}.

Table 1. Photometric *UBV* observations of YY Her

JD 2440000+	U	B	V
11275	15.10	14.85	13.71
11276	15.21	14.95	13.61
11284	14.75	14.73	13.66
11287	14.80	14.99	13.56
11306	15.01	15.06	13.60
11307	14.86	14.96	13.57
11308	14.86	15.03	13.51
11313	14.78	14.84	13.51
11319	14.80	14.73	13.36
11336	14.50	14.66	13.22
11345	14.47	14.68	13.26
11367	14.58	14.49	13.14
11370	14.39	14.47	13.10
11374	14.61	14.46	13.03
11376	–	14.48	13.14
11387	–	14.38	13.10
11397	14.29	14.40	13.08
11400	14.22	14.43	13.08
11422	14.02	14.52	13.11
11434	13.96	14.32	13.00
11453	13.79	14.22	13.01
11475	14.07	13.92	13.08
11493	13.58	14.22	13.01
11634	13.66	14.06	12.86
11678	13.88	14.07	12.93
11720	14.43	14.40	13.15
11752	14.23	14.35	13.11
11762	14.60	14.44	13.10
11820	14.56	14.75	13.43
11845	14.88	14.98	13.79
11864	14.98	15.08	13.61

VARIABILITY

Regular photometric observations of the symbiotic star YY Her have been carried out since June 1995. Previously, only separate *UBV* points, which mostly covered the brightness maximum during the 1993 outburst, and a fairly complete visual light curve were available. The brightness of YY Her rapidly evolved during the initial period after its outburst. Thus, for example, its U brightness in the first two months declined at a rate $dU/dt \approx 0.01$ mag day^{-1}, which is an order of magnitude faster than that recorded by Kolotilov *et al.* (2001) for the symbiotic star AS 338. During the three subsequent orbital cycles, the system slowly returned to quiescence; its U brightness declined at a rate $dU/dt \approx 5.7 \times 10^{-4}$ mag day^{-1}.

Table 2. Photometric *VRI* observations of YY Her

JD 2440000+	V	R	I
11865	13.52	11.76	10.06
11866	13.52	11.74	10.05
11867	13.57	11.76	10.09
11868	13.57	11.73	10.08
11879	13.46	11.71	10.09
11887	13.33	11.58	10.00
11888	13.33	11.59	10.02
11953	13.10	11.45	10.08

The 1997 minimum (see Fig. 3) was fairly broad with a period of constant minimum brightness lasting at least for 130 days (judging by the U light curve). It should be noted that the brightness decline at short wavelengths began earlier, more specifically, at least 60 days earlier in U than in V. The reverse was observed as the star was emerging from its minimum: the rise in brightness took effect first in the visual and then in the ultraviolet.

The next minimum observed in 1999 was narrow. Figure 3 shows part of the U light curve together with a symmetric curve const $\times\,|\cos(x)|$. We managed to observe only one branch, when the star emerged from its minimum. If the light curve is assumed to be symmetric about the phase of primary minimum, then it may be concluded that there was no state of constant brightness at the 1999 minimum, in contrast to that observed in 1997. The color indices near minimum light corrected for interstellar reddening [$E(B-V) = 0\overset{m}{.}2$] are $\langle U-B\rangle_{1999} = 0\overset{m}{.}25$ and $\langle B-V\rangle_{1999} = 1\overset{m}{.}34$, although the $\langle B-V\rangle$ color is the same as that during the previous minimum; judging by $\langle U-B\rangle$, the star became much redder ($\langle U-B\rangle_{1997} = -0\overset{m}{.}1$). This is because the contribution of the nebular emission to the total flux became smaller than that during the previous minimum, which is attributable to decline in the activity of the hot component of YY Her. Note also an increase in the variability amplitude in all bands when passing to quiescence: $\Delta U = 1\overset{m}{.}6$, $\Delta B = 1^m$, and $\Delta V = 0\overset{m}{.}8$ (during the 1997 minimum, $\Delta U = 1\overset{m}{.}15$, $\Delta B = 0\overset{m}{.}75$, and $\Delta V = 0\overset{m}{.}5$). Since the near-ultraviolet

Table 3. Emission-line fluxes and equivalent widths of the Hβ and He II λ4686 lines*

Date	U	Phase	4340 H I	4363 [O III]	4686 He II	4740 He I	4861 H I	5876 He I	6678 He I	4861 $W_{\mathrm{H}\beta}$	$W_{\mathrm{He\,II}}$
Aug. 4, 2000	14.23	0.85	15.7	7.3	22.8	6.5	33.2	5.4	18.9	39.1	26.8
Oct. 4, 2000	14.56	0.95	–	–	18.2	–	22.7	–	10.9	36.0	28.9

* The fluxes are given in units of 10^{-13} erg cm^{-2} s^{-1}. The equivalent widths were taken relative to the continuum at 3600 Å calculated from the U magnitude.

Table 4. FWHMs, heliocentric radial velocities, and equivalent widths of emission and absorption (Na I) lines in YY Her. The values for October 28, 1999, and August 1, 1993, are given in and without parentheses, respectively

λ, Å	$\Delta\lambda$, Å	V, km s^{-1}	W, Å
He II, 4686*	0.93	−91	2.11
Hβ	0.75(0.68)	−11(−1.3)	29.2(−)
He I, 4921	0.55	−23	1.88
Fe II, 4924*	0.61	−42	1.47
[OIII], 4959	0.38	−49	0.26
[OIII], 5007*	0.92	−48	2.28
He I, 5015	0.41	−74	1.38
Fe II, 5018	0.50	−24	1.57
Fe II, 5168	0.52	−29	0.98
Fe II, 5197	0.46	−26	0.54
Fe II, 5235	0.44	−26	0.62
Fe II, 5284	0.39	−37	0.38
Fe II, 5317	0.44	−26	1.01
Fe II, 5363	0.39	−25	0.30
He I, 5875(P Cyg)	0.72(0.67)	−6(3.2)	5.28(8.75)
Na I, 5890(abs)	0.32	−20	0.28
Na I, 5896(abs)	0.3	−23	0.18
Fe II, 6456?	0.7	−29	0.51
Hα	1.15(0.80)	2(13)	129.4(112.9)
He I, 6678	0.80(0.41)	−19(−17.6)	4.46(8.50)
He I, 7065(P Cyg)	0.74(0.73)	−10(−5.6)	2.99(4.53)

* A blend of several lines.

light variations undoubtedly result from an eclipse of most of the nebula (>80%) and since the nebula is associated with the hot component, it should be assumed that YY Her has a large inclination to the line of sight, i.e., it is seen almost edge-on.

Similar variability amplitudes were observed in quiescence for the eclipsing symbiotic star BF Cyg, although the temperatures of the hot components of these stars differ greatly [$T_{\mathrm{hot}} = 60000$ K for BF Cyg (Mikolajewska *et al.* 1989) and $T_{\mathrm{hot}} = 100000$ K for YY Her]. However, the light curves of YY Her have no sinusoidal shape characteristic of several symbiotic stars and BF Cyg in particular. Judging by the light curve, the minimum occurred before MJD 11275 (where MJD = JD−2440000), which is at least 30 days earlier than that calculated from the ephemeris given by Munari *et al.* (1997a).

The coverage of the 2000 minimum by V observations was most complete. Since it is similar in shape and depth to the previous minimum, it may be

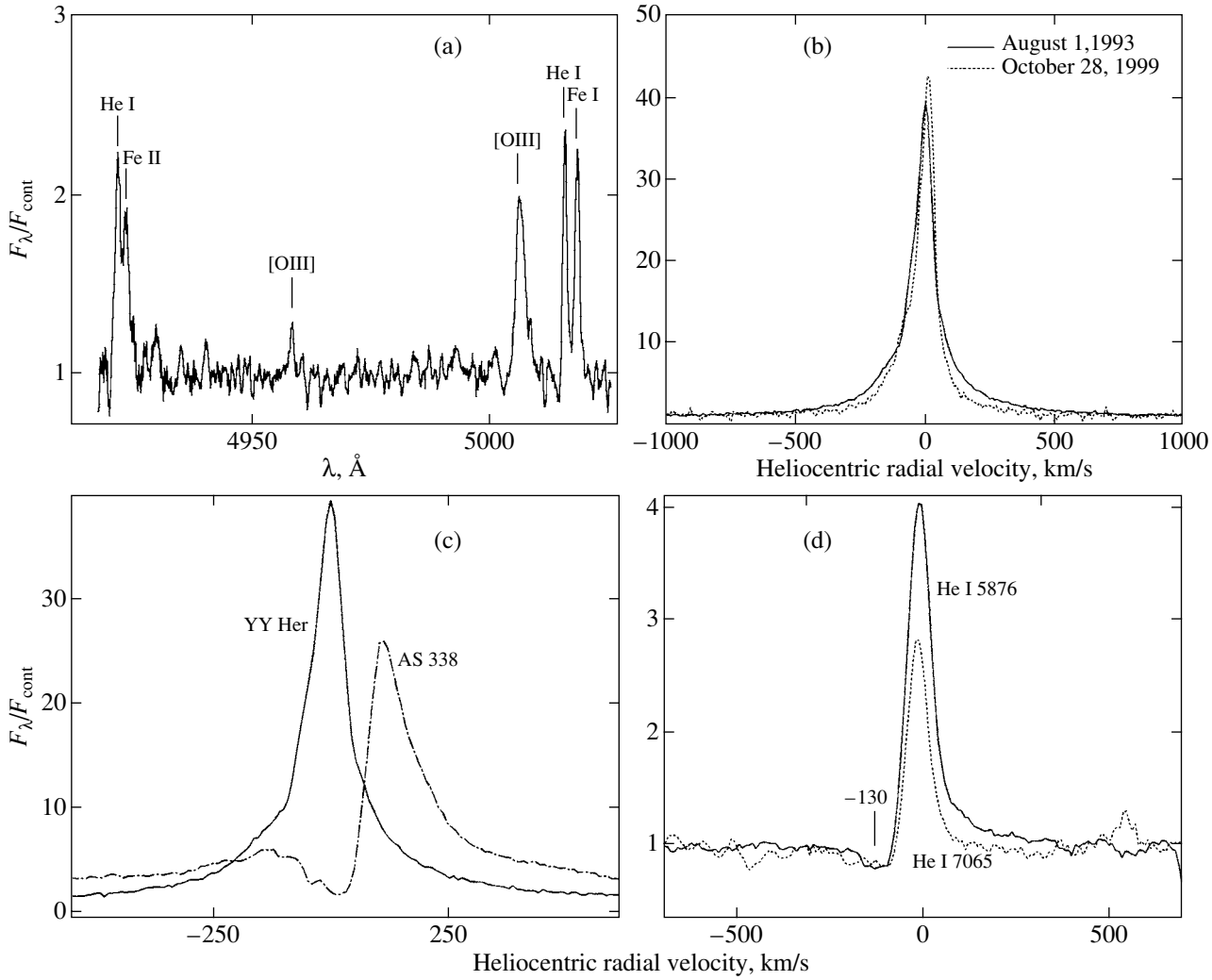

Fig. 2. Portion of the spectrum for YY Her during the strong 1993 outburst (Fig. 2a) and Hα profiles in quiescence and during the outburst (Fig. 2b); Fig. 2c shows Hα profiles of the symbiotic stars YY Her (August 1993) и AS 338 (November 1993), and Fig. 2d shows He I $\lambda\lambda$5876, 7065 profiles during the outburst. In all cases, the continuum-normalized flux is along the vertical axis.

concluded that YY Her returned to quiescence and that its active phase lasted slightly longer than three orbital cycles. The middle of the minimum was at MJD = 11849; below, we assume it to be the phase of minimum light. The period was found from a series of V observations, including visual magnitude estimates from Munari *et al.* (1997a) when YY Her was in quiescence, by using the code of Yu.K. Kolpakov (SAI, http://infra.sai.msu.ru/kolpakov) to be 586 days. In Fig. 1, the dates of minima are given by

$$\mathrm{Min}(V) = 2451848 + 586^{\mathrm{d}}E.$$

Mikolajewska (Copernicus Astronomical Center) gives the following ephemeris:

$$\mathrm{Min}(V) = 2448919.8 + 589.4^{\mathrm{d}}E.$$

The light curves suggest that the dates of minima slightly differ in different bands.

DISCUSSION

Cool Component

A shallow secondary minimum is occasionally observed in V at a phase of $\sim$0.5 (see Fig. 1); it is also seen in the visual light curve of YY Her published by Munari *et al.* (1997a). This minimum most likely results from the ellipticity of the cool component (for $T_{\mathrm{hot}} \approx 10^5$ K, $T_{\mathrm{cool}} \approx 3500$ K, and equal bolometric fluxes of the components, the ratio of their radii is $\sim$0.001, which rules out the possibility that an eclipse of part of the red giant by the hot component affects the light curve). This means that the cool component of YY Her fills much of its Roche lobe.

The primary minimum in V cannot be explained by an eclipse of the gaseous nebula alone. Figure 4 shows the optical spectra of YY Her at phases close

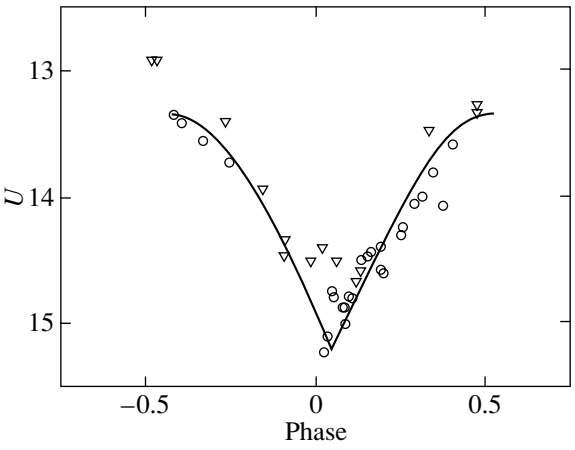

Fig. 3. Comparison of the U light curves during the minima of 1997 (triangles) and 1999 (open circles). The solid line represents a symmetric curve const $\times$ $|\cos(x)|$.

to the 1997 and 2000 minima, as well as the model energy distributions as a sum of the emissions from the nebula and the red giant. The spectral energy distributions for red giants were taken from Beshenova and Kharitonov (1975), M3.5, and Silva and Cornell (1992), M4. We assumed the nebular emission to consist of free–free and free–bound H II and He III emissions [a(He) = 0.1] and the electron temperature of the nebula to be $T_e = 20000$ K. Judging by the fit to the May 12, 1997 spectrum (Fig. 4a), only the red giant emitted in V at that time; subsequently, by August 21, 1997 (Fig. 4b), the V brightness declined further by almost $0^m.5$ [these spectra were considered by Tatarnikova *et al.* (2000)]. This change in brightness should be entirely attributed to the cool component. A similar pair of spectra were taken in 2000 (Figs. 4c, 4d). At that time, the visual brightness difference was $0^m.3$. Consequently, the cool component of YY Her is variable.

For the V light curve to be constructed for the cool component of YY Her, the combined contribution of the hot component and the nebula must be subtracted from the overall light curve. Therefore, based on all the available spectra [including those from Tatarnikova *et al.* (2000)] taken either before the outburst or after October 1994, when the optical energy distribution could be satisfactorily described in terms of a three-component model (a cool component, a hot component, and a nebula absorbing all Lc photons of the hot component), we constructed a dependence of $V_{\rm hot}$ on U:

$$V_{\rm hot} = 0.978U + 1.60,$$

where $V_{\rm hot}$ is the total magnitude of the nebula + hot component (or only the nebula at phases close to the minimum) determined by convolving the calculated energy distribution with the transmission curve in V, and U is the observed photometric magnitude.

Subsequently, we corrected the V light curve for the emissions from the hot component and the nebula. Figure 5 shows the light curve of the cool component from MJD = 10194 folded with the ephemeris given in the preceding section. Its characteristic features are a sharp primary minimum with a depth of $0^m.8$ and a broader secondary minimum with a depth of $0^m.3$. Also shown in this figure is the folding of all the available R magnitude estimates; for clarity, these data points are displaced along the vertical axis to coincide with the V magnitudes of the cool component. Although the effect of the Paschen continuum on the R magnitude is negligible, these estimates cannot be ascribed to the cool component alone because of the presence of a bright Hα line whose equivalent width at maximum light is 113 Å. However, allowance for the contribution of this line would change the R magnitude estimates by no more than $0^m.1$. The available data points suggest that the secondary minimum is also observed in R and that its amplitude is approximately equal to the amplitude in the visual band. The secondary minimum most likely results from the ellipticity effect. It should then be assumed that the cool component of YY Her nearly fills its Roche lobe and that the system is observed almost edge-on. The ultimate confirmation of this would be the detection of a secondary minimum on the infrared light curves.

It should be noted that as the system was emerging from its last minimum, the brightness of the cool component rose more slowly with increasing wavelength. As the V brightness of YY Her rose by $0^m.5$, when, judging by the 1997 spectra, this change can be assumed to be entirely attributable to the cool component, its R brightness increased by $0^m.3$, while its I brightness was nearly constant (only erratic light variations at a $\Delta I = 0^m.1$ level were observed). The folding of all the available R magnitude estimates shows (see Fig. 5) that the amplitude of the primary minimum in R is slightly smaller than that in V, whereas in I, the primary minimum is virtually unobservable: the estimates from Table 2 for the primary minimum match the out-of-eclipse magnitude estimates for the system from Table 4 in Munari *et al.* (1997a). Such a strong wavelength dependence of the eclipse depth suggests that this feature may result from the egress of a hot spot on the cool component's surface illuminated by the hot component (reflection effect). This is also confirmed by the fact that, as was shown by Tatarnikova *et al.* (2000), the spectral type of the cool component determined from TiO bands exhibits a phase dependence, with the latest spectral type being observed at primary minimum. However, the theoretical calculations of the reflection effect for

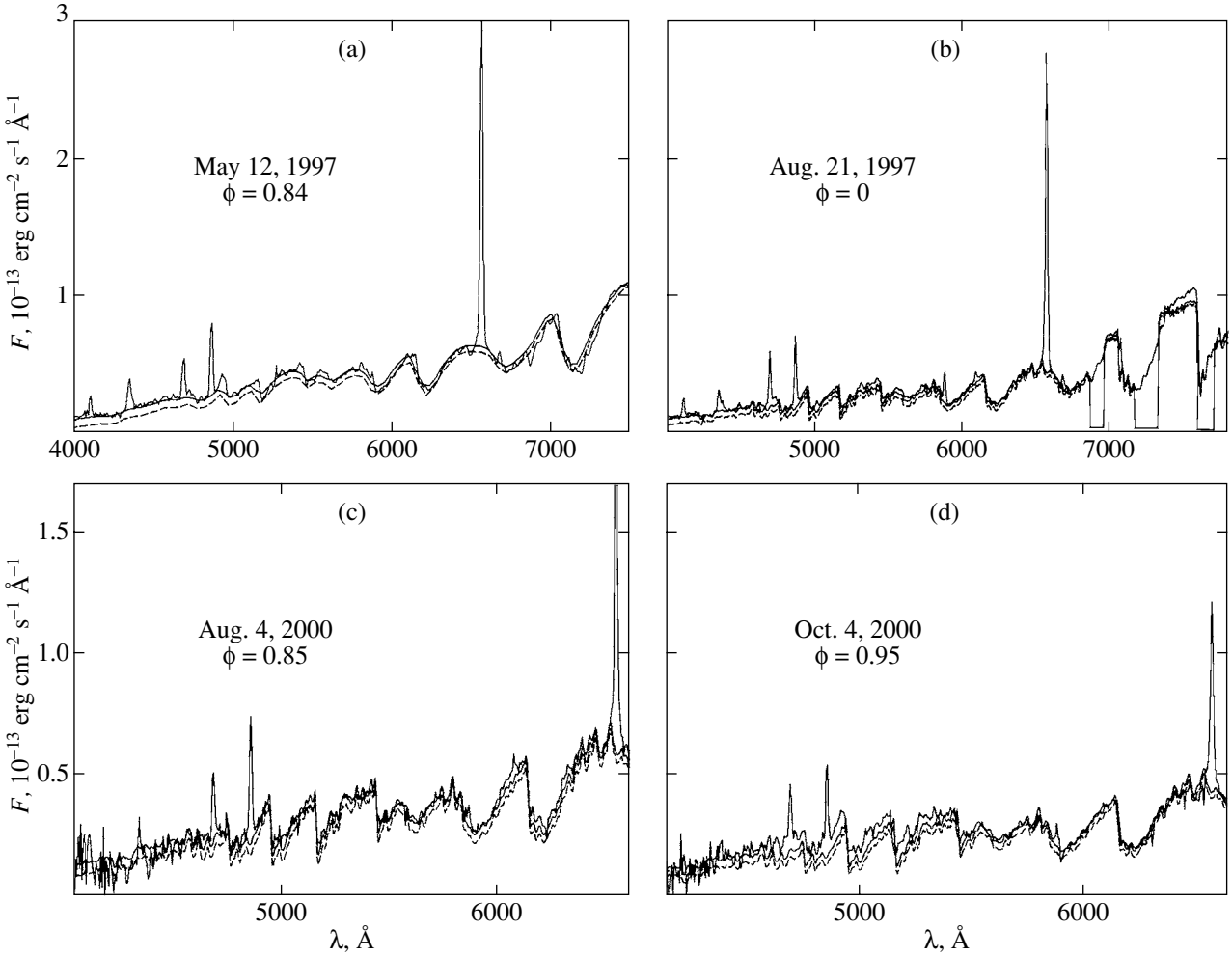

Fig. 4. Spectra of YY Her at phases close to the 1997 (a, b) and 2000 (c, d) minima. The solid and dashed lines represent, respectively, model energy distributions in the continuum (nebula + cool component) and in the cool component's spectra [the giant is M3.5 III for panel (a) and M4 III in the remaining cases]. In panel (b), the wavelengths at which strong absorption bands of the Earth's atmosphere lie are marked by zero fluxes in the spectrum of the red giant.

symbiotic stars by Proga *et al.* (1996, 1998) do not confirm any significant effect of the hot component's radiation on the temperature and optical brightness of the cool component.

Further optical and infrared photometric observations will allow the light curves of the cool component to be constructed at various wavelengths. This, in turn, will make it possible to interpret the light curves in terms of a model that includes the ellipticity and hot-spot effects.

If the period of constant brightness observed in 1997 is assumed to be associated with an eclipse of the nebula by the red giant, then the components' sizes with respect to the separation between the cool component and the nebula (p), more specifically, the sizes of the cool component and the dense, compact part of the nebula ($R_{\rm cool}/p$ and $R_{\rm neb}/p$), can be estimated from the phases of the inner and outer contacts. As has been shown previously by Tatarnikova *et al.* (2000), the cool component significantly overfills its Roche lobe for spherical components in a circular orbit of radius p and for a nebula that surrounds the hot component (i.e., if p is equal to a, the orbital semimajor axis for YY Her). Since the derived radius of the giant must be within the Roche lobe, it remains to assume that much of the gaseous nebula lies between the components rather than near the hot component. At approximately equal masses of the cool and hot components of YY Her, the compact gaseous nebula should be placed almost halfway between the components ($p = a/2$). However, such estimates significantly depend on the nebula's geometry, and for symbiotic stars, there is reason to suggest that the nebula is bipolar in shape. Skopal *et al.* (1997) ran into a similar problem when analyzing the minimum observed in BF Cyg during a bright outburst in 1989.

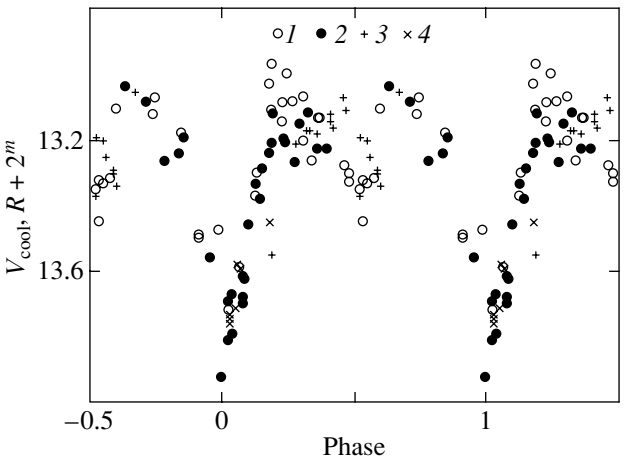

Fig. 5. Folding of the V light curve for the cool component of YY Her over the last three periods; open circles represent data from Tatarnikova *et al.* (2000), and filled circles represent our data. For clarity, the R magnitude estimates are displaced along the vertical axis by two magnitudes; pluses represent data from Munari *et al.* (1997a), and crosses represent our data.

In this case, the condition $R_{\rm giant} < R_{\rm Roche}$ requires an abnormally large component mass ratio for BF Cyg ($q > 6$). It should be noted that the phase of constant brightness was observed in BF Cyg only during the first minimum after the onset of its outburst, while for YY Her, this minimum is third from the onset of an active phase. The first two minima may have been similar in shape, but this cannot be firmly established because of the breaks in the observations.

Spectroscopic observations in the red could be very helpful in determining the luminosity class for the cool component of YY Her. This is because the depths of optical TiO bands are a reliable criterion for determining only the temperature (or spectral type) of the cool component, while the absorption lines available in this wavelength range cannot be reliably measured due to the complex behavior of the continuum. However, criteria that allow a red giant to be distinguished from a supergiant have been developed in the red spectral range [e.g., Kenyon and Fernandez-Castro (1987) used the Na I $\lambda\lambda$8181,8195 doublet for this purpose].

The Nebula and the Hot Component

The difference in shape between the 1997 minimum and the 1999 and 2000 minima is probably attributable to a change in the nebular structure. The 1997 minimum appears as if the densest compact part of the nebula, which gives the largest contribution (80%) to the U flux, were totally eclipsed. In contrast, judging by the absence of a phase of constant brightness near the minimum, an extended nebula with sizes of the order of the cool component's size is eclipsed at the subsequent minima, i.e., the nebula increased in size. However, the fact that the star at the 1999 minimum was almost $0^m\!.7$ fainter in U than at the 1997 minimum suggests that the activity of the hot component during this period continued to decline and that the number of Lc photons decreased. Whereas, judging by the fit to the August 21, 1997 spectrum (see Fig. 4b), the nebula's emission measure at the 1997 minimum was $\mathrm{ME} = n_e^2 V = 9.5 \times 10^{57} (\mathrm{d}/10\ \mathrm{kpc})^2\ \mathrm{cm}^{-3}$, its emission measure at the next minimum must be approximately a factor of 2 smaller. The nebula's size can increase as the volume emission measure decreases only when the mean electron density decreases.

If the cool component is assumed to fill its Roche lobe, then its luminosity must be $3600 L_\odot$ (Tatarnikova *et al.* 2000). For the spectral type M4, we obtain $R_g = 170 R_\odot$. The mean electron density of the eclipsed compact structure can then be determined from the 1997 minimum: $2 \times 10^{10}\ \mathrm{cm}^{-3}$; a similar high density was obtained by Mikolajewska *et al.* (1989) for the inner region of the nebula in the symbiotic star BF Cyg.

ACKNOWLEDGMENTS

We wish to thank the referees for helpful critical remarks. This study was supported by the Russian Foundation for Basic Research (project nos. 00-02-16471, 00-15-96533, and 99-02-17589), and KBN grant no. 5P03D019 20 of the Polish Research Committee.

REFERENCES

1. L. D. Beshenova and A. V. Kharitonov, Tr. Astrofiz. Inst., Akad. Nauk Kaz. SSR **27**, 1 (1975).
2. A. Cassatella, T. Fernandez-Castro, R. Gonzalez-Riestra, and J. J. Fuensalida, Astron. Astrophys. **258**, 368 (1992).
3. S. J. Kenyon and T. Fernandez-Castro, Astron. J. **93**, 938 (1987).
4. E. A. Kolotilov, J. Mikolajewska, P. M. Marrese, *et al.*, Pis'ma Astron. Zh. **27**, 61 (2001) [Astron. Lett. **27**, 51 (2001)].
5. J. Mikolajewska and S. J. Kenyon, Mon. Not. R. Astron. Soc. **256**, 177 (1992).
6. J. Mikolajewska, S. J. Kenyon, and M. Mikolajewski, Astron. J. **98**, 1427 (1989).
7. U. Munari, M. Rejkuba, and M. Hazen, *et al.*, Astron. Astrophys. **323**, 113 (1997a).
8. U. Munari, E. A. Kolotilov, A. A. Popova, and B. F. Yudin, Astron. Zh. **74**, 898 (1997b) [Astron. Rep. **41**, 802 (1997b)].
9. U. Murset and H. M. Schmid, Astron. Astrophys., Suppl. Ser. **137**, 473 (1999).

10. D. Proga, S. J. Kenyon, and J. C. Raymond, Astrophys. J. **471**, 930 (1996).
11. D. Proga, S. J. Kenyon, and J. C. Raymond, Astrophys. J. **501**, 339 (1998).
12. D. R. Silva and M. E. Cornell, Astrophys. J., Suppl. Ser. **81**, 865 (1992).
13. A. Skopal, A. Vittone, L. Errico, *et al.*, Mon. Not. R. Astron. Soc. **292**, 703 (1997).
14. A. A. Tatarnikova, M. Rejkuba, L. M. Buson, *et al.*, Astron. Zh. **77**, 802 (2000) [Astron. Rep. **44**, 190 (2000)].

Translated by V. Astakhov

Astronomy Letters, Vol. 27, No. 11, 2001, pp. 712–718. Translated from Pis'ma v Astronomicheskiĭ Zhurnal, Vol. 27, No. 11, 2001, pp. 834–840.

Apsidal Motion in the Close Binary IT Cassiopeiae

V. S. Kozyreva* **and A. I. Zakharov**

Sternberg Astronomical Institute, Universitetskii pr. 13, Moscow, 119899 Russia

Received May 26, 2000; in final form May 31, 2001

Abstract—In 1982 and 1993, we carried out highly accurate photoelectric *WBVR* measurements for the close binary IT Cas. Based on these measurements and on the observations of other authors, we determined the apsidal motion [$\dot{\omega}_{\rm obs} = (11\overset{\circ}{.}0 \pm 2\overset{\circ}{.}5)/100$ years]. This value is in agreement with the theoretically calculated apsidal motion for these stars [$\dot{\omega}_{\rm th} = (14^\circ \pm 3^\circ)/100$ years]. © 2001 MAIK "Nauka/Interperiodica"

Key words: *eclipsing variable stars, apsidal motion*

INTRODUCTION

IT Cassiopeiae (IT Cas) (GSC 3650–959, $\alpha_{2000} = 23^{\rm h}42^{\rm m}01^{\rm s}$, $\delta_{2000} = +51^\circ44'.6$, F6 V+F6 V, $P = 3\overset{\rm d}{.}90$, $e = 0.089$, $V = 11\overset{\rm m}{.}2$) was discovered by Fadeeva as an eclipsing binary on the basis of photographic observations; she also obtained its first photographic light curve (Parenago 1938). Florya (1946) constructed a complete light curve of this system by using 337 photographic plates (from 1933 until 1939) and refined its orbital period ($P = 3\overset{\rm d}{.}89672$). In addition, Busch (1975) obtained a photographic light curve by reducing 1958–1973 photographic plates.

We carried out the first photoelectric *WBVR* measurements at the Tien-Shan Observatory of the Sternberg Astronomical Institute (SAI) in 1982. The photoelectric light curve was used to calculate the components' photometric parameters and orbital elements (Khaliullin and Kozyreva 1989). Our 1993 photometric measurements presented here aimed at investigating the apsidal motion in IT Cas.

OBSERVATIONS

In 1993, we made photometric *WBVR* measurements (Kornilov *et al.* 1991) of IT Cas with a 50-cm AZT-14 reflector at the Tien-Shan High-Altitude Astronomical Observatory of the SAI (Moscow State University) using the four-channel photoelectric photometer designed by Kornilov and Krylov (1990). We obtained the light curves at primary and secondary minima and estimated the brightness outside the minima.

The Tien-Shan observations from 1982 (Khaliullin and Kozyreva 1989) were reprocessed and significantly corrected for this study: we modified the background subtraction procedure (this is, in particular, true for the July 16, 1982 observations) and, more importantly, eliminated the error in the calculated heliocentric correction to the phase (July 22, 1982). A new table of the 1982 and 1993 observations was placed on the Web page at http://lnfm1.sai.msu.ru/~valq (broad-band photometry).

Figures 1 and 2 show our V observations of IT Cas in 1993 relative to the comparison star HD 236202 (BD+50° 4119). We obtained the *WBVR* magnitudes for IT Cas and the comparison star HD 236202 with respect to *WBVR* standards (Khaliullin *et al.* 1985) in 1982 and 1993.

Photoelectric observations of the eclipsing binary JT Cas have also been carried out by a number of other authors. Several B, V, and R light curves at minima were obtained during the 1994–1995 campaign at the Mount Maidanak High-Altitude Observatory in Uzbekistan by Zakirov (Sandberg Lacy *et al.* 1997). In 1995, Wolf (Holmgren and Wolf 1996) measured the primary and secondary minima of this star at the Ondřejev Observatory near Prague. The observations were performed with a CCD array in R.

During 1982–1985, Sandberg Lacy obtained a radial-velocity curve for IT Cas (Sandberg Lacy *et al.* 1997) and determined the components' masses.

ALGORITHMS AND MODELS

Light-Curve Solution. A Model and Minimization Method

We seek for the photometric parameters and orbital elements by using a simple model of two spherical stars with a linear limb-darkening law that move around a common center of mass in elliptical orbits. The light curve of this model depends on the following parameters:

*E-mail: valq@sai.msu.ru

1063-7737/01/2711-0712$21.00

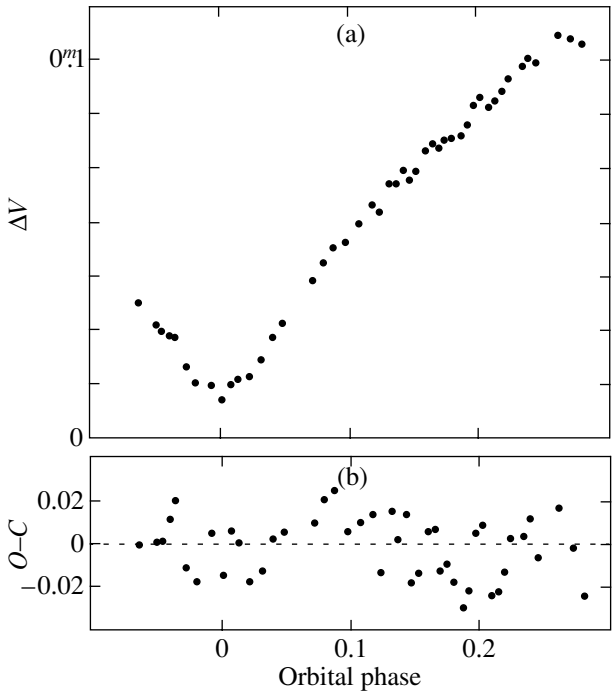

Fig. 1. (a) V light curve for IT Cas at primary minimum. Residuals from the theoretical light curve that was calculated with the photometric elements from Table 3 are shown in panel (b).

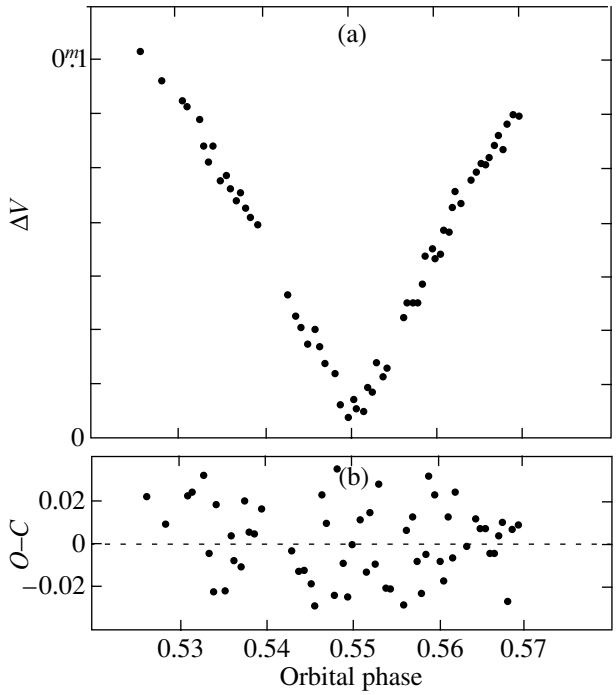

Fig. 2. Same as Fig. 1 for the secondary minimum.

$r_{1,\,2}$, the radii of the primary and secondary components;

$u_{1,\,2}$, the limb-darkening coefficients for the components;

$L_{1,\,2}$, the components' luminosities in fractions of the system's total luminosity;

i, the orbital inclination;

e, the orbital eccentricity;

ω, the longitude of periastron of the primary orbit;

$E_{\rm I}$, the epoch of the primary minimum in $JD_\odot$ corresponding to the epoch of the observations analyzed;

L_3, the parameter of the "system's third-light parameter" (which is related to the system's magnitude outside the minimum as $-2.5\log(L_1+L_2+L_3)+\mathrm{const}=m_0$).

The brightness during an eclipse can be determined at any JD by analytic integration. At the contact times of the stellar disks, when the second derivatives abruptly change, the derivatives are calculated from analytic expansions in a small parameter. This allowed us to use a quasi-Newtonian method with an analytic calculation of the derivatives of the functional (Gill and Murray 1978) as a minimizing algorithm.

The functional to be minimized contains a sum of the squares of the difference between the observed and theoretical magnitudes at each point and the Lagrange function that includes simple and linear constraints on the sought-for parameters.

Analyses of the light curves for several eclipsing binaries show that the iterations converge to the minimum even from a very distant initial point when certain constraints are imposed on the initial conditions, for example, when the correct quadrant is chosen for the periastron longitude.

The effect of the limb-darkening coefficients u_1 and u_2 on the system's brightness manifests itself in the light-curve segments immediately adjacent to the contact points of the stellar disks. We find that because these parameters weakly affect the light curve, they can be reliably determined only from high-accuracy ($\delta \le 0\overset{m}{.}005$) observations with the required completeness in these light-curve segments. Since, in general, the accuracy of the light curves for most systems under study is considerably lower, we recommend to use the appropriate theoretical values for u_1 and u_2 (Wade and Rucinski 1985).

We imposed the following constraints on the sought-for parameters:

$$0 < r_{1,\,2} < 0.5,$$
$$0 < e < 0.9,$$
$$\pi/4 < i < \pi/2,$$
$$0 < \omega < 2\pi,$$
$$0 < L_{1,2} < 1,$$
$$0 < u_{1,2} < 1,$$

$$-1/4P < \Delta E_{\rm I} < 1/4P,$$

where $\Delta E_{\rm I}$ is the difference between the initial approximation and the actual epoch of the primary minimum.

With additional information, more stringent constraints can be used.

To avoid obtaining a false minimum, one of the following two inequalities was included in the Lagrange function:

$$0 \le r_1 - r_2 \le 1$$

or

$$0 \le r_2 - r_1 \le 1.$$

A condition is chosen if additional information is available on the components' radii. If there is no such information, then the calculation is performed by two independent methods and the method with smaller residuals between the theoretical and observed light curves is chosen.

Computational experience shows that the quasi-Newtonian method with an analytic calculation of the derivatives of the functional is a very reliable and quick way of analyzing the light curves of eclipsing systems, despite the large number of parameters and constraints.

Determining the Apsidal Motion

Subsequently, we modified the algorithm for calculating the elements to simultaneously use all light curves of the system. To this end, we added the following parameters to the set of variables:

$\dot{\omega}$, the apsidal motion;

dP, the correction to the period of primary minimum;

L_3^i, the third-light parameters for each light curve involved in the solution.

Using the third-light parameters for each light curve compensates for the change in the system's brightness outside the minimum that can result from physical variability of the star or the comparison star and from the errors in the light-curve correction for the Earth's atmosphere. These parameters are calculated only when the depth of the minimum can be reliably determined from the light curve. Therefore, observations that cover only one branch of the minimum are not used for the analysis.

The small value and the absence of systematic variations in the residuals for each light curve serve as a check on the solution.

Note the following advantages of the method:

(1) All light curves are taken into account;

(2) The velocity of apsidal rotation enters into the functional as a free parameter;

(3) The systematic errors attributable to the long-period variability of the observed stars are compensated; and

(4) Apart from the epoch of minima, i.e., the information used in the method of analyzing $O-C$ diagrams (Gimenez and Garsio-Pelayo 1983; Sandberg Lacy 1992), the widths of the minima are also taken into account.

Estimating the Errors in the Close-Binary's Photometric Parameters and in Its Orbital Elements

Note that the errors can be considered only for the chosen binary model. Analyzing the behavior of the residuals for different light curves of the system serves as a check on the adequacy of the model. In this way, we can detect the components' ellipticity or the reflection effect that was disregarded in the model.

In the chosen model, it must be verified that the residuals from the theoretical model have a nearly normal distribution. This is true if the systematic measurement errors and the physical fluctuations of the stars under study or the comparison stars are taken into account. We used the Kolmogorov–Smirnov criterion to test the hypothesis of a normal distribution of the residuals. The light curves whose residuals showed significant deviations from the normal distribution were rejected.

In searching for errors in the parameters, we superimposed a normally distributed noise signal with a variance equal to the estimated variance of the observed light curve on the theoretical light curve found by minimization. The curves obtained in this way were used to seek for new sets of parameters. Multiple application of the described procedure yielded sets of deviations of the sought-for parameters, which were used to determine the distributions of errors in the calculated parameters.

Figure 3 shows model distributions of the deviations of some parameters for the star IT Cas under study.

PARAMETERS OF THE STARS AND ORBITAL ELEMENTS FOR IT CAS. THE APSIDAL MOTION

We used an algorithm based on the quasi-Newtonian minimization method to determine the components' parameters, orbital elements, and the apsidal motion for IT Cas.

For the solution, we used our 1982 and 1993 observations at Tien-Shan and Zakirov's V observations in 1995 at Mount Maidanak (Sandberg Lacy *et al.* 1997). Zakirov's 1994 observations were not used in our analysis, because their accuracy was severalfold lower.

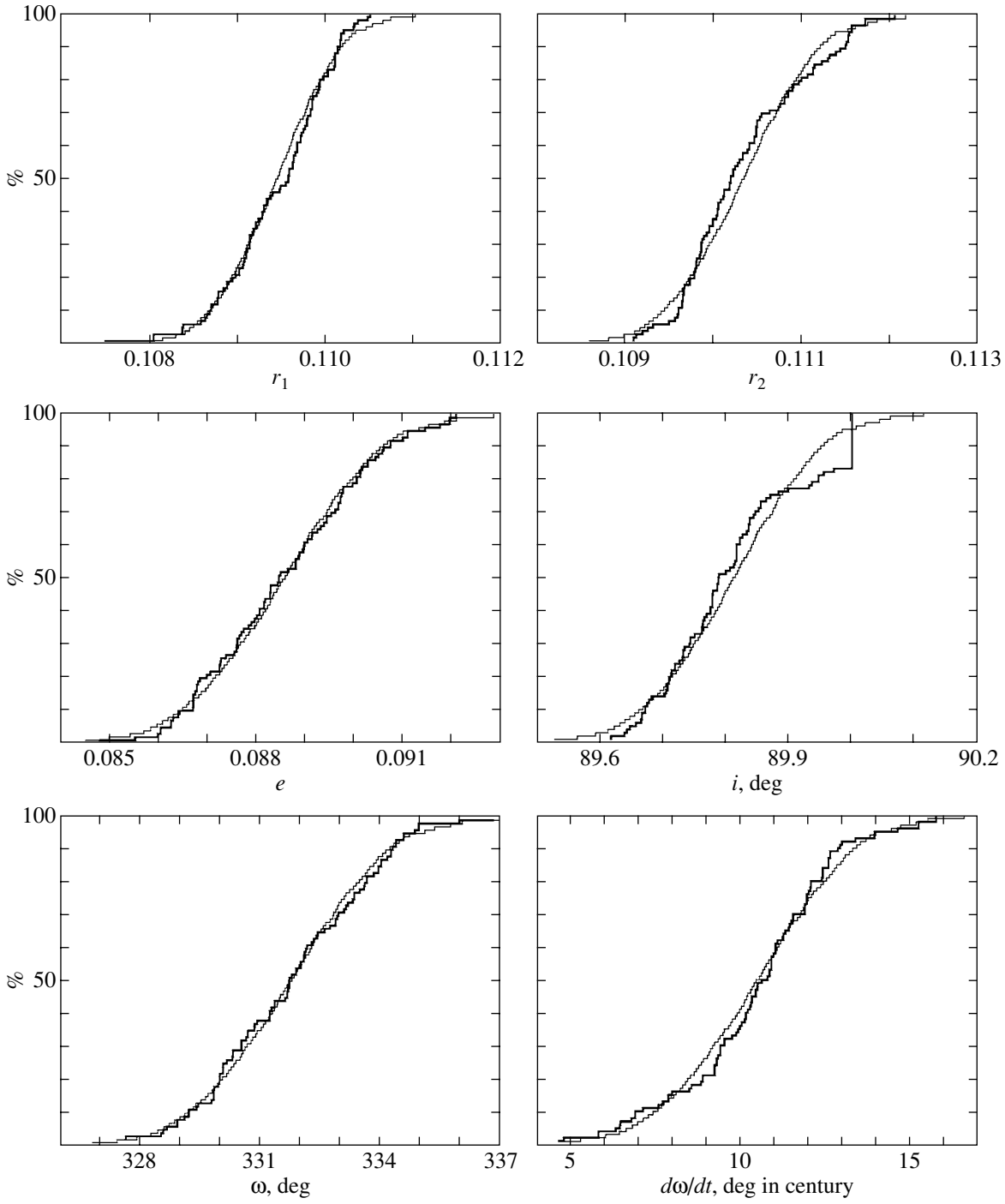

Fig. 3. The distribution functions for r_1, r_2, i, e, ω, and $\dot{\omega}_{\rm obs}$ obtained by varying a model light curve. The thin line represents the normal distributions functions with the appropriate means and variances of these parameters (Table 2).

From the large series of 1995 observations, we chose only those with a sufficient number of points on both branches of the minima. We required that the branches of the minima be generally undistorted by the systematic errors due to variations in the atmospheric transparency.

The analyzed minima are listed in Table 1. The stars' parameters and the system's orbital elements determined by using the entire set of light curves are given in Table 2.

In our search for the epochs of the minima given in Table 1, we performed calculations using each individual light curve. According to Table 2, we fixed the components' relative radii (r_1 and r_2), limb-

Table 1. The heliocentric epochs of minima for IT Cas as derived from measurements of different authors

$JD_\odot - 2440000$	$O-C$	Min	Authors
5167.3158	$0^d.0000$	I	Kozyreva and Zakharov (this paper)
5173.3542	0.0000	II	Kozyreva and Zakharov (this paper)
9239.3141	0.0002	I	Kozyreva and Zakharov (this paper)
9245.3534	−0.0010	II	Kozyreva and Zakharov (this paper)
9923.3716	−0.0001	II	Sandberg Lacy *et al.* (1997)
9927.2687	0.0004	II	Sandberg Lacy *et al.* (1997)
9948.5032	−0.0008	I	Holmgren and Wolf (private communication)
9954.5441	−0.0009	II	Holmgren and Wolf (private communication)
9956.2972	−0.0001	I	Sandberg Lacy *et al.* (1997)
9962.3382	0.0000	II	Sandberg Lacy *et al.* (1997)

Table 2. Parameters of the components and orbital elements for IT Cas as inferred from the 1982–1995 photoelectric light curves

Element or parameter	Value	Element or parameter	Value
r_1	0.1096^{+5}_{-8}	u_1	0.58 (adopted)
r_2	0.1102^{+9}_{-6}	u_2	0.58 (adopted)
i	$89^\circ.8^{+2}_{-1}$	$E_{\rm I}$	$JD_\odot\ 2445167^d.3158^{+3}_{-3}$
e	0.089 ± 0.002	$E_{\rm II}$	$JD_\odot\ 2445169^d.4576^{+6}_{-6}$
ω_0	$332^\circ \pm 2^\circ$	$\varphi_{\rm II}$	$0^p.5497 \pm 0.0002$
$\dot\omega_{\rm obs}$	$11^\circ{}^{+2}_{-3}$/100 yrs	$P_{\rm I}$	$3^d.8966489^{+3}_{-3}$
L_1	0.496^{+3}_{-7}	$P_{\rm II}$	$3^d.8966509^{+5}_{-5}$
L_2	0.497^{+5}_{-3}	σ	$0^m.0155$

darkening coefficients (u_1 and u_2), orbital inclination (i), eccentricity (e), the initial longitude of periastron (ω_0), and the period of the primary minimum (P_I). In view of the detected physical light fluctuations in the system, we varied L_3, the third-light parameter. We sought for the times of conjunction of the components during a primary eclipse (T_I) as free parameters. The absence of appreciable systematic deviations of the residuals (the difference between observed and theoretical brightnesses) for points of the minimum as a function of eclipse phase served as a check on the derived epoch of the minimum. The times of conjunction for the secondary minima (T_{II}) were calculated from the well-known relation in Kopal (1978) by assuming that the rate of change in the longitude of periastron ($\dot\omega$) was constant:

$$T_2 = T_1 + \frac{P}{2} + \frac{2Pe\cos\omega}{\pi} - \frac{2Pe^3(1+3\sqrt{1-e^2})}{3\pi(1+\sqrt{1-e^2})^3}\cos 3\omega + \ldots,$$

$$\omega = \omega_0 + \dot\omega(t - t_0).$$

Here, P is the orbital period of the close binary, t is the time of the corresponding eclipse, and t_0 is the time when the periastron longitude was ω_0.

To calculate $O-C$ (Table 1), we used the ephemerides of the primary and secondary minima (Table 2) computed with the derived elements.

The stars' parameters and orbital elements match, within the error limits, the solution obtained for this system by other authors (Sandberg Lacy *et al.* 1997). The system IT Cas consists of two F5 V stars with nearly equal radii and luminosities.

When analyzing a large series of published observations (Sandberg Lacy *et al.* 1997), we found that IT Cas exhibited quasi-periodic (about a month) light variations with an amplitude of $\sim 0^m.03$ in V outside the minimum. Such light variations outside the minimum are also characteristic of our observations of this star. Since the observations were carried out with different comparison stars, the above variations

refer to the long-period light variations in the IT Cas itself. We emphasize that, apart from other elements, our method of seeking for the elements and the apsidal motion includes the set of parameters L_3^i that normalizes the brightness outside the minimum for each light curve used in the analysis. This parameter compensates for the star's light variations caused by its long-period variability.

The apsidal motion obtained simultaneously with the remaining parameters in a free search is

$$\dot{\omega}_{\rm obs} = (11\overset{\circ}{.}0^\circ \pm 2\overset{\circ}{.}5)/100 \text{ years}.$$

CONCLUSIONS AND DISCUSSION

We theoretically calculated the classical and relativistic terms of apsidal motion by using the system's absolute parameters (Sandberg Lacy *et al.* 1997) and the corresponding constants of apsidal motion (Claret and Gimenez 1992). The stars' relative parameters and orbital elements were taken from Table 2. The theoretical apsidal motion for this system is

$$\begin{aligned}\dot{\omega}_{\rm th} = \dot{\omega}_{\rm cl} + \dot{\omega}_{\rm rel} &= (10^\circ \pm 3^\circ)/100 \text{ years} \\ &+ (4.0^\circ \pm 0\overset{\circ}{.}2)/100 \text{ years} \\ &= (14^\circ \pm 3^\circ)/100 \text{ years}.\end{aligned}$$

Thus, within the accuracy, the observed apsidal motion $\dot{\omega}_{\rm obs}$ for IT Cas agrees with its theoretical value. This result is yet another confirmation that the calculations of the internal structure for main-sequence stars (Claret and Gimenez 1992) are correct.

The method of analyzing an $O-C$ diagram, the time dependence of the difference between the observed and calculated epochs of minima (Gimenez and Garsio-Pelayo 1983, Sandberg Lacy 1992), is commonly used to determine the apsidal motion. The errors of this method depend on the accuracy of determining the epochs of minima from light curves. Because of the asymmetry in the light curves for systems with eccentric orbits, light fluctuations, and measurement errors, different methods for determining the epochs of minima yield differing results. To obtain a correct estimate for the apsidal motion, it is not enough to compare the epochs of minima derived by different authors; it is also necessary to make sure that the systematic errors are negligible or equal.

Let us compare the result for IT Cas from Sandberg Lacy *et al.* (1997),

$$\dot{\omega}_{\rm obs} = (23\overset{\circ}{.}1 \pm 22\overset{\circ}{.}2)/100 \text{ years}$$

with that published by Holmgren and Wolf (1996),

$$\dot{\omega}_{\rm obs} = (93\overset{\circ}{.}2 \pm 14\overset{\circ}{.}6)/100 \text{ years}.$$

The two results were obtained by analyzing $O-C$ diagrams (Sandberg Lacy 1992). In both cases, all the known epochs of minima for IT Cas, even the photographic ones, were used. The list of the epochs of minima used in the former case was supplemented with the 1995 observations in Uzbekistan. The difference by a factor of 4 suggests that the method is unreliable. For IT Cas, this is explained by peculiarities of the system's geometry. First, the longitude of the orbital periastron ($\sim 330^\circ$) is close to a position at which the time derivative of $O-C$ is small (the slopes of $O-C$ for the primary and secondary minima on the plot), causing the error of the method to double. Second, at a low eccentricity (0.089), the amplitude of variations in the $O-C$ differences for the epochs of the primary and secondary minima over the entire observing period is comparable to the errors of photographic observations. All of these factors determine the incorrect result of Holmgren and Wolf (1996) and the large error in the apsidal motion found by Sandberg Lacy *et al.* (1997).

Another method of determining the apsidal motion is based on calculating the difference between the longitudes of periastron obtained for two different epochs of observations. In this method, one of the necessary conditions is the availability of highly accurate light curves for two pairs of primary and secondary minima closely spaced in time for each epoch; one pair must be sufficiently far from the other.

During one season, high-quality observations can be obtained only for one minimum, with the apsidal motion being determined by assuming that the system's geometry is unchanged. This assumption for the light curve at a different, much later epoch can lead to systematic variations in the residuals between the calculated and observed curves due to the variations in the orbital inclination or eccentricity. Since the calculated apsidal motion will be erroneous, this method requires a mandatory check on the behavior of the residuals.

To illustrate the method of comparing two epochs, we took the R light curves for IT Cas obtained by Wolf in 1995. These data were kindly made available to us by the author. As the first epoch, we took our 1982 observations. For both light curves, the elements were determined with the fixed orbital eccentricity ($e = 0.0893$) and inclination ($i = 90\overset{\circ}{.}0$) calculated when freely seeking for the elements by using the 1982 light curves. The limb-darkening coefficients u_1 and u_2 were fixed according to their theoretical values, 0.58 in V and 0.46 in R for the two components (Wade and Rucinski 1985).

The apsidal motion calculated from these two pairs of light curves is

$$\dot{\omega}_{\rm obs} = (10^\circ \pm 3^\circ)/100 \text{ years}.$$

This value agrees, within the error limits, with our main result.

The apsidal motion that we derived for IT Cas agrees with its theoretical value, but it is considerably lower and more accurate than that in Sandberg Lacy *et al.* (1997)

ACKNOWLEDGMENTS

We wish to thank M. Wolf, who kindly provided the observations, and V.G. Moshkalev for help in the observations.

REFERENCES

1. H. Busch, Hartha Mitt. **9**, 10 (1975).
2. A. Claret and A. Gimenez, Astron. Astrophys., Suppl. Ser. **96**, 255 (1992).
3. N. F. Florya, Perem. Zvezdy **6**, 34 (1946).
4. P. E. Gill and W. Murray, Math. Program. **14**, 349 (1978).
5. A. Gimenez and J. M. Garsio-Pelayo, Astrophys. Space Sci. **92**, 203 (1983).
6. D. Holmgren and M. Wolf, Observatory **116**, 307 (1996); Bull. Astron. Inst. Czech. **23**, 147.
7. Kh. F. Khaliullin and V. S. Kozyreva, Astrophys. Space Sci. **155**, 53 (1989).
8. Kh. F. Khaliullin, A. V. Mironov, and V. G. Moshkalyov, Astrophys. Space Sci. **111**, 291 (1985).
9. Z. Kopal, *Dynamics of Close Binary Systems* (D. Reidel, Dordrecht, 1978).
10. V. G. Kornilov, I. M. Volkov, A. I. Zakharov, *et al., A Catalogue of WBVR Magnitudes of Bright Northern-Sky Stars* (Gos. Astron. Inst., Moscow, 1991), Tr. Gos. Astron. Inst., Mosk. Gos. Univ. **63** (1991).
11. V. G. Kornilov and A. V. Krylov, Astron. Zh. **67**, 173 (1990) [Sov. Astron. **34**, 90 (1990)].
12. R. R. Parenago, Perem. Zvezdy **5**, 157 (1938).
13. C. H. Sandberg Lacy, Astron. J. **104**, 801 (1992).
14. C. H. Sandberg Lacy, G. Torres, D. W. Latham, *et al.*, Astron. J. **114**, 1206 (1997).
15. R. A. Wade and S. M. Rucinski, Astron. Astrophys. **60**, 471 (1985).

Translated by V. Astakhov

Astronomy Letters, Vol. 27, No. 11, 2001, pp. 719–727. Translated from Pis'ma v Astronomicheskiĭ Zhurnal, Vol. 27, No. 11, 2001, pp. 841–849.

Photometric Variability and Spectral Features of the Protoplanetary Nebula LSII + 34°26 = V1853 Cyg

V. P. Arkhipova[1, *], N. P. Ikonnikova[1], R. I. Noskova[1], G. V. Komissarova[1], V. G. Klochkova[2], and V. F. Esipov[1]

[1]*Sternberg Astronomical Institute, Universitetskiĭ pr. 13, Moscow, 119899 Russia*
[2]*Special Astrophysical Observatory, Russian Academy of Sciences, pos. Nizhniĭ Arkhyz, 357147 Russia*

Received June 15, 2001

Abstract—We present photoelectric and spectroscopic observations of the protoplanetary object V1853 Cyg, a B supergiant with an IR excess. Over two years of its observations, the star exhibited rapid irregular light variations with amplitudes $\Delta V = 0\overset{m}{.}3$, $\Delta B = 0\overset{m}{.}3$, $\Delta U = 0\overset{m}{.}4$ and no correlation between color and magnitude. Its mean magnitude has not changed since the first *UBV* observations in 1973 (Drilling 1975). Low-resolution spectroscopic observations show that the spectrum of V1853 Cyg in 2000 corresponded to that of a B1–B2 star with $T_{\rm eff} \sim 20000$ K. High-resolution spectroscopic observations confirm the conclusion that the profiles of absorption and emission lines are variable. We identified the star's spectral lines and measured the equivalent widths of more than 40 lines. The star's radial velocity is $\langle V_r \rangle = -49 \pm 5$ km s^{-1}, as measured from absorption lines, and ranges from -50 to -85 km s^{-1} for different lines, as measured from shell emission lines. The velocity of the dust clouds on the line of sight determined from diffuse interstellar bands (DIBs) and from interstellar Na I lines is $\langle V_r \rangle = -16 \pm 5$ km s^{-1}. The P Cyg profiles of the He I λ5876 Å and λ6678 Å lines suggest an ongoing mass loss by the star. An analysis of the observational data confirms the conclusion that the star belongs to the class of intermediate-mass protoplanetary objects. © 2001 MAIK "Nauka/Interperiodica"

Key words: *protoplanetary objects, photoelectric and spectroscopic observations*

INTRODUCTION

LSII + 34°26 is a star from the Catalog of Luminous Stars (Stok *et al.* 1960). Turner and Drilling (1984) estimated its distance to be ~ 17.8 kpc by assuming that this star was a massive B1.5 Ia–Iabe supergiant. Its magnitude variations over five nights with amplitudes of $0\overset{m}{.}1$ in B and V and $0\overset{m}{.}2$ in U (Turner and Drilling 1984) gave grounds to include it in the 68th list of variable stars (Kholopov *et al.* 1987), where it was designated as V1853 Cyg and classified as an α Cygni variable. Since the *IRAS* satellite detected far-IR radiation from the object, Parthasarathy (1993) suggested that V1853 Cyg = IRAS 20462 + 3416 is a low-mass post-AGB B-type supergiant surrounded by a cold dust envelope with $T_{\rm dust} \sim 100$ K located at a distance of 3–4.6 kpc, rather than a massive population I B star. The spectrum of V1853 Cyg consists of absorption lines typical of an early B supergiant and the emission-line spectrum of a gaseous shell. The H I and He I lines have P Cyg profiles, which, together with the presence of shifted C IV and Si IV absorption lines in the stellar UV spectrum, are indicative of mass outflow from the star (Garcia-Lario *et al.* 1997). The profiles of absorption lines and H I and He I emission lines change, which may be evidence for a variable stellar wind (Smith and Lambert 1994; Garcia-Lario *et al.* 1997). Garcia-Lario *et al.* (1997) determined the electron density in the circumstellar envelope, $n_e \sim 10^4$ cm^{-3}, from the intensity ratio of the [S II] doublet emission lines $I(\lambda 6717)/I(\lambda 6731) = 0.5$. Ueta *et al.* (2000) discovered a large reflection nebula $\sim 3''$ in size around V1853 Cyg with the Hubble Space Telescope.

UBV OBSERVATIONS

Photometrically variable protoplanetary objects are the focus of our special attention (Arkhipova *et al.* 2000, 2001b). There are few published photometric observations of V1853 Cyg: two magnitude estimates in 1973 (Driling 1975) and five magnitude estimates in 1979 (Turner 1983). Therefore, in 1999,

*E-mail: vera@sai.msu.ru

Table 1. UBV observations of V1853 Cyg in 1999–2000

JD 2400000+	U	B	V	$U-B$	$B-V$	JD 2400000+	U	B	V	$U-B$	$B-V$
51336.503	10.262	11.114	10.909	−0.852	0.205	51746.435	10.618	11.358	11.200	−0.740	0.158
51345.460	10.438	11.270	11.093	−0.832	0.177	51747.370	10.317	11.123	10.946	−0.806	0.177
51346.488	10.481	11.305	11.102	−0.824	0.203	51750.447	10.527	11.321	11.120	−0.794	0.201
51347.503	10.398	11.218	11.047	−0.820	0.171	51752.437	10.326	11.144	10.951	−0.818	0.193
51351.484	10.299	11.143	10.956	−0.844	0.187	51753.485	10.419	11.208	11.016	−0.789	0.192
51352.442	10.480	11.289	11.101	−0.809	0.188	51754.515	10.531	11.291	11.109	−0.760	0.182
51369.513	10.474	11.255	11.099	−0.781	0.156	51755.387	10.384	11.192	11.002	−0.808	0.190
51402.400	10.318	11.120	10.939	−0.802	0.181	51759.458	10.409	11.195	11.037	−0.786	0.158
51409.432	10.406	11.210	11.023	−0.804	0.187	51761.371	10.511	11.306	11.151	−0.795	0.155
51411.383	10.554	11.332	11.177	−0.778	0.155	51762.474	10.295	11.148	10.967	−0.853	0.181
51451.388	10.378	11.169	10.979	−0.791	0.190	51763.517	10.541	11.283	11.097	−0.742	0.186
51452.302	10.427	11.202	11.048	−0.775	0.154	51764.369	10.462	11.241	11.070	−0.779	0.171
51453.363	10.271	11.098	10.908	−0.827	0.190	51765.426	10.464	11.285	11.141	−0.821	0.144
51454.243	10.326	11.160	10.995	−0.834	0.165	51766.417	10.438	11.213	11.027	−0.775	0.186
51455.346	10.470	11.280	11.064	−0.810	0.216	51767.456	10.465	11.204	11.016	−0.739	0.188
51456.309	10.294	11.113	10.938	−0.819	0.175	51768.415	10.471	11.266	11.104	−0.795	0.162
51457.309	10.345	11.155	10.983	−0.810	0.172	51776.492	10.418	11.207	10.968	−0.789	0.239
51458.384	10.386	11.214	11.072	−0.828	0.142	51777.492	10.545	11.303	11.107	−0.758	0.196
51459.243	10.484	11.226	11.063	−0.742	0.163	51778.499	10.364	11.147	10.925	−0.783	0.222
51467.374	10.261	11.073	10.900	−0.812	0.173	51779.484	10.637	11.486	11.320	−0.848	0.166
51691.445	10.408	11.189	11.010	−0.781	0.179	51779.512	10.689	11.509	11.294	−0.820	0.215
51692.524	10.388	11.250	11.070	−0.862	0.180	51780.499	10.347	11.137	10.950	−0.790	0.187
51693.453	10.423	11.216	10.998	−0.793	0.218	51781.451	10.280	11.097	10.910	−0.817	0.187
51694.397	10.340	11.129	10.957	−0.789	0.172	51782.492	10.442	11.175	10.978	−0.733	0.197
51695.500	10.438	11.242	11.064	−0.804	0.178	51789.464	10.557	11.396	11.163	−0.839	0.233
51701.500	10.321	11.211	10.933	−0.890	0.278	51791.474	10.491	11.293	11.104	−0.802	0.189
51702.424	10.587	11.298	11.114	−0.711	0.184	51806.347	10.292	11.142	10.969	−0.850	0.173
51703.437	10.350	11.129	10.941	−0.779	0.188	51815.367	10.378	11.192	11.036	−0.814	0.156
51705.485	10.422	11.158	10.994	−0.736	0.164	51815.372	10.358	11.210	11.046	−0.852	0.164
51706.465	10.382	11.182	11.007	−0.800	0.175	51816.372	10.320	11.113	10.940	−0.793	0.173
51707.456	10.353	11.179	11.029	−0.826	0.150	51817.482	10.416	11.225	11.029	−0.809	0.196
51708.412	10.402	11.184	11.019	−0.782	0.165	51818.459	10.411	11.219	10.982	−0.808	0.237
51709.492	10.548	11.200	11.019	−0.742	0.181	51818.476	10.395	11.190	10.984	−0.795	0.206
51710.475	10.445	11.210	11.060	−0.765	0.150	51820.387	10.578	11.304	11.121	−0.726	0.183
51720.456	10.464	11.263	11.090	−0.799	0.173	51821.273	10.443	11.219	11.081	−0.776	0.138
51721.441	10.497	11.264	11.073	−0.767	0.191	51822.413	10.400	11.128	10.965	−0.728	0.163
51722.495	10.423	11.196	11.013	−0.773	0.183	51823.426	10.380	11.170	11.012	−0.790	0.158
51724.499	10.327	11.116	10.944	−0.789	0.172	51824.313	10.343	11.158	10.990	−0.835	0.168
51725.499	10.329	11.129	10.936	−0.801	0.193	51824.321	10.341	11.152	10.970	−0.811	0.182
51728.481	10.385	11.193	11.022	−0.808	0.171	51836.364	10.322	11.112	10.934	−0.790	0.178
51729.490	10.389	11.149	10.995	−0.760	0.154	51841.363	10.318	11.130	10.949	−0.812	0.181
51730.497	10.340	11.156	10.982	−0.816	0.174	51849.358	10.551	11.289	11.073	−0.738	0.216
51732.485	10.402	11.210	11.044	−0.808	0.166	51850.302	10.664	11.350	11.177	−0.686	0.173
51734.488	10.385	11.142	10.988	−0.757	0.154	51853.321	10.602	11.279	11.089	−0.677	0.190

we included this star in our program of research on the variability of protoplanetary objects. During two observing seasons (1999–2000), we obtained ~90 UBV observations for the star. Our observations were carried out with a UBV photometer attached to a 60-cm Zeiss telescope at the Crimean Station of the Sternberg Astronomical Institute. The comparison stars were BD +34°4152 ($V =$

$9^m.95$, $B = 10^m.24$, $U = 10^m.34$, Appenzeller 1966) and GSC no. 2695.1362, whose magnitudes were determined by using BD +34°4152 for reference: $V = 11^m.24$, $B = 11^m.64$, $U = 11^m.83$. Table 1 gives our UBV observations, and Fig. 1 shows the star's UBV light curves. V1853 Cyg exhibits rapid erratic light variations with amplitudes of $\Delta V \sim 0^m.3$, $\Delta B \sim 0^m.3$, and $\Delta U \sim 0^m.4$. There is no correlation between color and magnitude (Fig. 2) and no periodicity with $P > 1^d$. The variability amplitude $\sim 0^m.3$ suggests flux variations by a factor of 1.3; since the gas continuum emission $E_c \sim n_e^2$, the electron density must vary by a factor of 1.14, which is quite possible for a variable mass-loss rate. Therefore, the photometric variability seems to be caused by a variable stellar wind. However, during some observing intervals (e.g., JD 2451703–2451734), the star exhibited smooth, monotonic night-to-night brightness changes; accordingly, pulsations with close short periods cannot be ruled out. Both a variable stellar wind and rapid low-amplitude pulsations appear to be responsible for the variability. The star's mean brightness estimated from the 1999–2000 observations, $\langle V \rangle = 11^m.03$, $\langle B \rangle = 11^m.21$, $\langle U \rangle = 10^m.42$, has been virtually constant since 1973 ($V = 11^m.07$, $B = 11^m.24$, and $U = 10^m.48$) (Drilling 1975).

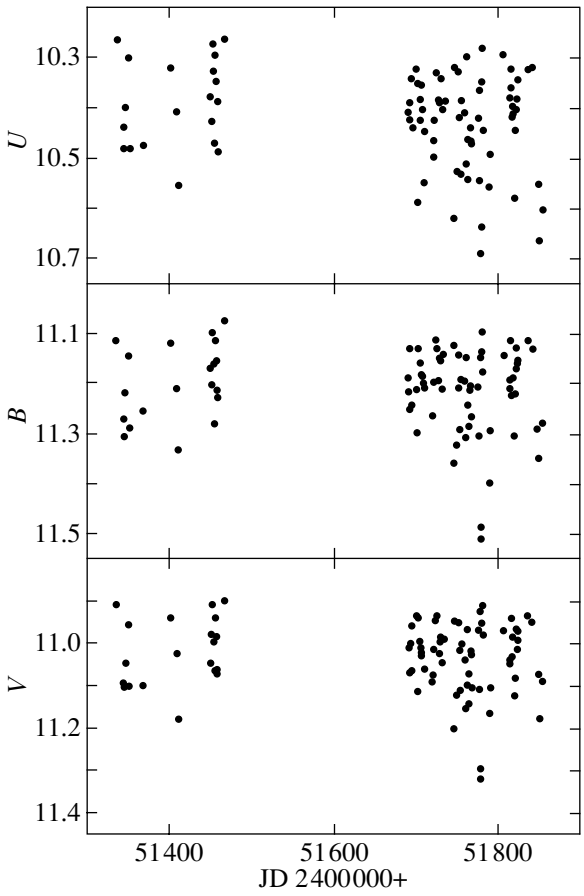

Fig. 1. UBV light curves of V1853 Cyg in 1999–2000.

EXTINCTION

Turner (1983) estimated the color excess of the star to be $E(B-V) = 0^m.38$ by assuming that its spectral type was B1.5 I. For neighboring stars, $E(B-V) = 0^m.21$–$0^m.27$ (Turner 1983). The extinction inferred from the intensity of the λ2200 Å band was estimated to be $E(B-V) = 0^m.24 \pm 0^m.05$ (Parthasarathy 1993). As in many protoplanetary objects (Arkhipova *et al.* 2000), the color excess of V1853 Cyg appears to be partly ($\geq 0^m.1$) attributable to the circumstellar dust envelope whose extinction law differs from the interstellar one.

SPECTROSCOPIC OBSERVATIONS

In 2000, three low-resolution spectrograms of V1853 Cyg were obtained in the wavelength range 4300–10000 Å. The observations were carried out with a 125-cm reflector at the Crimean Station of the Sternberg Astronomical Institute using a fast spectrograph. The detector was a SBIG ST6 274 × 375 CCD array, which, in combination with a 600 line mm^{-1} grating, yielded a resolution of 5.5 Å $pixel^{-1}$. The spectrum of V1853 Cyg exhibits the Hα and Hβ emission lines and He I lines; the most intense absorption features belong to Na I and O II.

The He I λ6678 Å line is also seen in absorption. We transformed the fluxes in the spectra taken on July 4 and 29, and on October 20, 2000, to absolute fluxes. The standard star was 3 Vul (B9 V) (Voloshina *et al.* 1982). Figure 3 shows portions of the spectra in the wavelength range 6500–7100 Å. Noteworthy are the different continuum levels and variability of the Hα, He I λ6678 Å, and λ7065 Å line profiles. The energy distribution in the wavelength range 4300–10000 Å corrected for the interstellar extinction with $E(B-V) = 0^m.38$ corresponds to the radiation from a star with $T_{\rm eff} \sim 20000$ K. The equivalent widths of the Balmer lines vary within $W(\mathrm{H}\beta) = 1.3$–2.6 Å, $W(\mathrm{H}\alpha) = 11.5$–$16.2$ Å.

A CCD spectrum of V1853 Cyg was taken at the Special Astrophysical Observatory on June 12/13, 2000, with the PFES echelle spectrometer (Panchuk *et al.* 1998) at the prime focus of the 6-m telescope. The 4290–7220 Å spectrum consists of 22 $\sim$200 Å echelle orders with a $\sim$25 Å overlap. The three-pixel resolution (projected entrance-slit width)

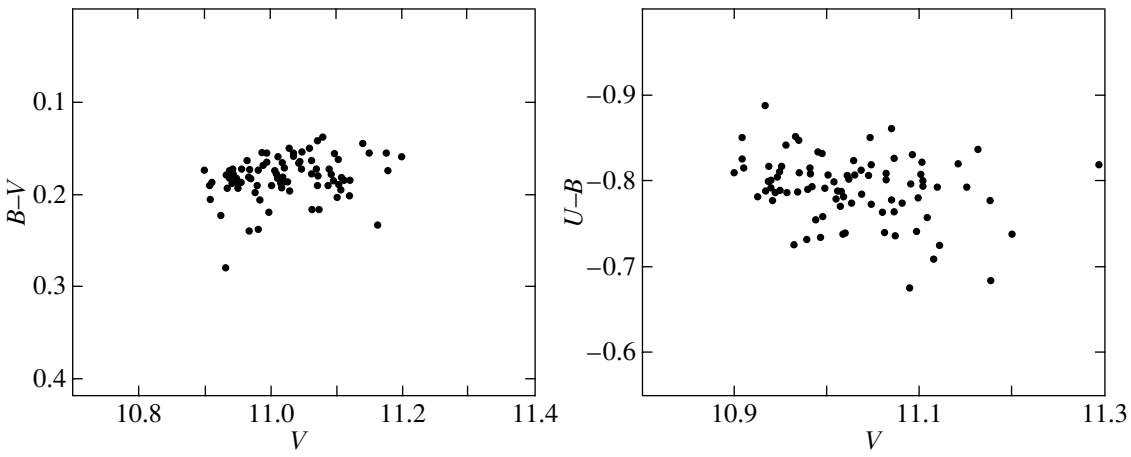

Fig. 2. Color–magnitude diagrams for V1853 Cyg.

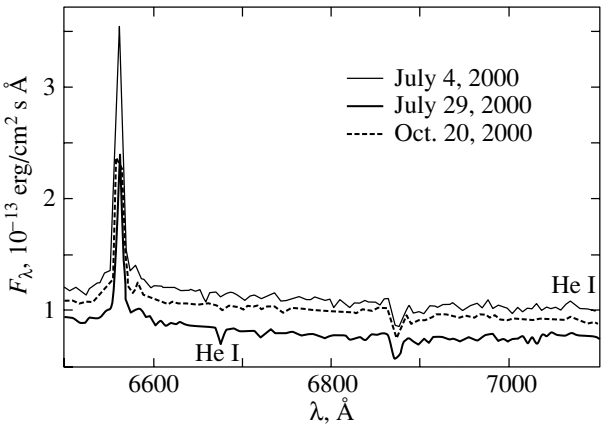

Fig. 3. Low-resolution spectrum of V1853 Cyg in the wavelength range λ6500–7100 Å.

is $R \sim 15000$. We performed the standard reduction of echelle spectra (dark-current subtraction, cosmic-ray hit removal, echelle-order extraction, and linearization) using the ECHELLE context of the ESO-MIDAS package (version 98NOV).

As has been noted previously (Smith and Lambert 1994, Garcia-Lario *et al.* 1997), the line spectrum of V1853 Cyg is represented by two components: the absorption spectrum of a B1.5 supergiant and the emission spectrum of a low-excitation gaseous shell superimposed on it. We identified lines in the spectrum of V1853 Cyg using the tables of Moore (1945) and the catalog of emission lines by Meinel *et al.* (1969). Table 2[1] lists the lines in the wavelength range λ4290–7200 Å. The first column gives instrumental wavelengths of the spectral lines. The subscripts a and e denote absorption and emission features, respectively. The second column contains laboratory wavelengths of the lines, and the third column contains species and multiplet numbers. Figure 4 shows portions of the spectrum taken on June 12/13, 2000. The star's spectrum exhibits the entire set of lines typical of a B supergiant. In addition to H I and He I lines, these include numerous O II, N II, and C II absorption features. Also present are Si III, Al III, and Fe II lines. Note that there are very weak He II λ4686 Å and λ6171 Å absorption lines in the spectrum. The star's spectrum clearly shows numerous diffuse interstellar bands (DIBs), as well as strong Na I D_1 and D_2 interstellar lines (Fig. 4d): $W_\lambda(D_1) = 0.76$ Å and $W_\lambda(D_2) = 0.65$ Å. The hydrogen- and helium-line profiles are complex. The stellar Hα and Hβ absorption lines are filled with shell emission lines; a narrow emission feature is superimposed on the broad Hγ absorption line. The He I λ4387.9 Å and λ5047.7 Å lines are in absorption, whereas the λ4921 Å, λ4471 Å, and λ5016 Å absorption lines have emission components. The λ7065 Å line is in emission, while the λ5876 Å and λ6678 Å lines have P Cyg profiles. The emission spectrum of the gaseous shell is also represented by [N II], [S II], and Si II lines. Also present is a weak Na I D_2 emission feature, which is distorted by a strong Na I D_2 absorption. There are no [O III] lines. The intensity ratio of the [S II] doublet $I(\lambda6717)/I(\lambda6731) = 0.51$ corresponds to $n_e = 1.1 \times 10^4$ cm^{-3}. Table 3 gives equivalent widths of the most prominent absorption lines in the spectrum and compares them with the previously determined values. As we see from Table 3, our equivalent widths of the N II lines exceed those determined by Garcia-Lario *et al.* (1997) by a factor of two or more, whereas the O II, Al III, and S III lines

[1] Table 2 is published in electronic form only and is accessible at ftp cdsarc.u-strasbf/fr/pub/cats/J (130.79.128.5) or http://cdsweb.u-strasbg.fr/pub/cats/J.

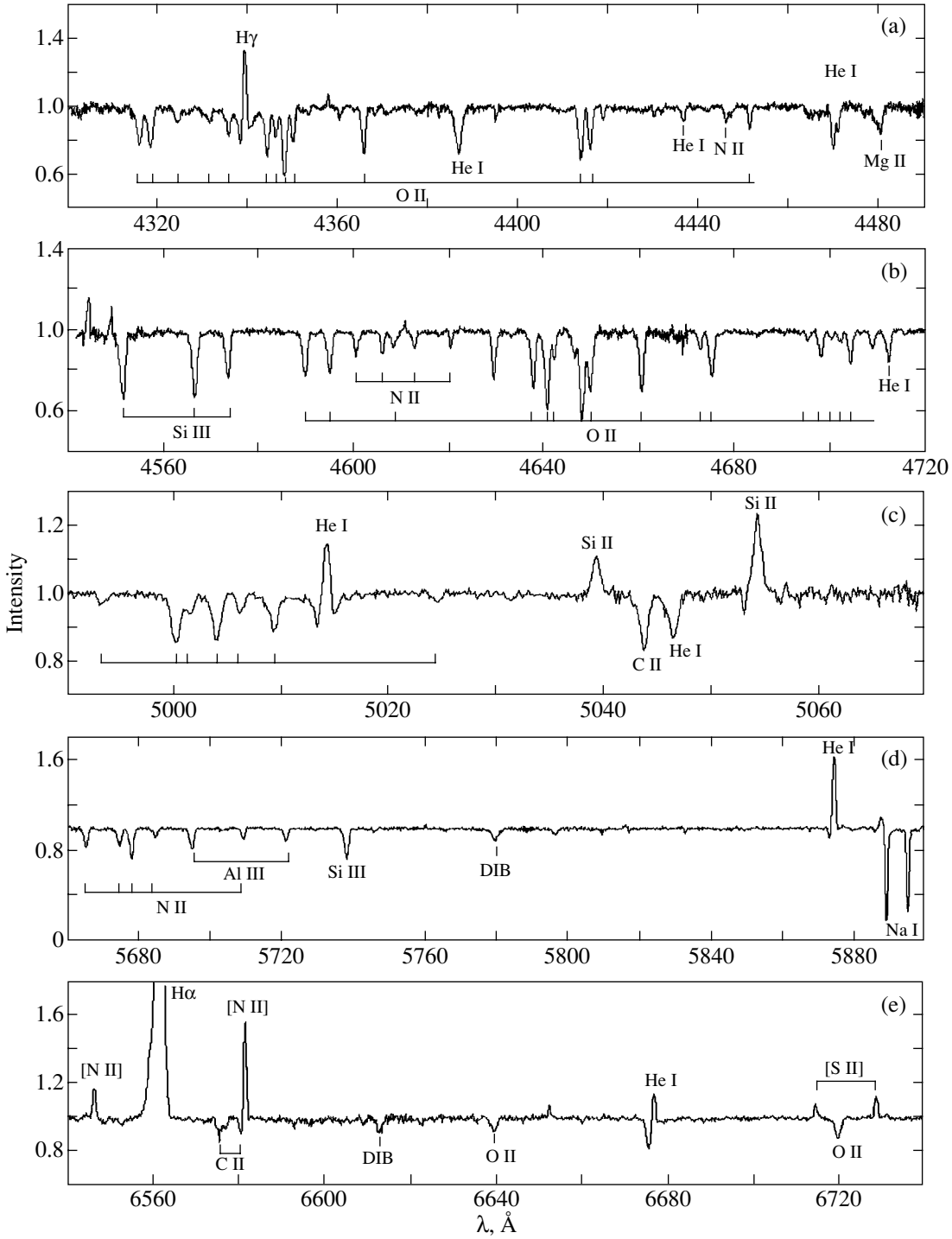

Fig. 4. Portions of the echelle spectrum for V1853 Cyg taken on June 12/13, 2000.

show much smaller differences. Equivalent widths of the emission lines are given in Table 4.

Numerous radial-velocity determinations are available for V1853 Cyg. As was noted previously (Smith and Lambert 1994; Garcia-Lario *et al.* 1997), the star's radial velocities exhibit large and rapid variations. Table 5 gives the heliocentric velocities inferred from many absorption and emission lines. The mean velocity derived from O II, N II, C II, Si III, and Al III absorption lines was $\langle V_r \rangle = -49 \pm 5$ km s^{-1} and corresponds to the radial velocity of the star itself. The mean radial velocities differ for

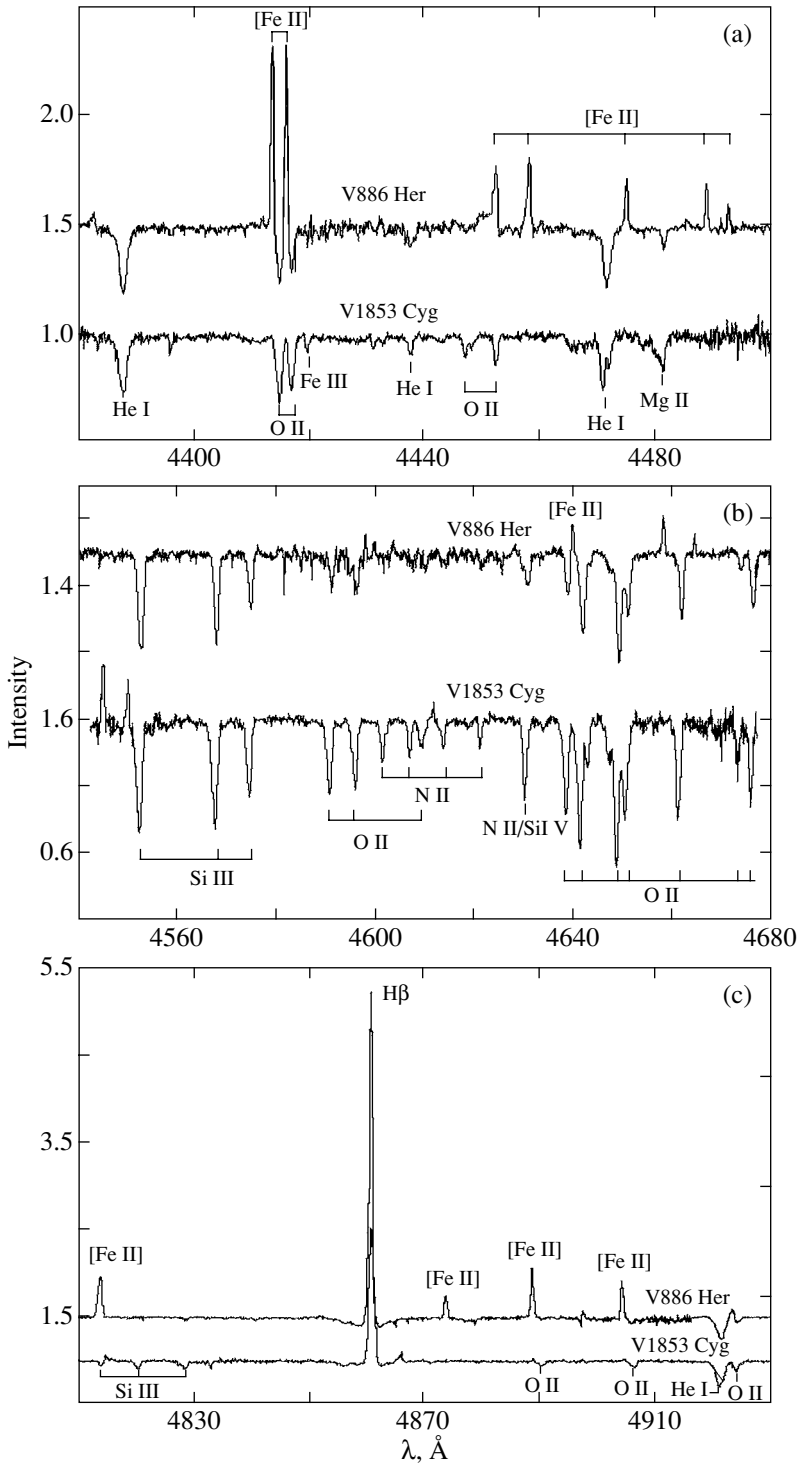

Fig. 5. Comparison of the echelle spectra for V1853 Cyg and V886 Her.

different emission lines. Thus, the heliocentric radial velocities determined from [N II] and Si II lines are -68 ± 2 km s^{-1}, which is in excellent agreement with those determined by Smith and Lambert (1994). However, [S II] lines yield $V_r = -85 \pm 1$ km s^{-1}, which may result from the stratification of emissions in the gaseous shell. The radial velocities determined from diffuse Na I D_1 and D_2 interstellar lines and from diffuse interstellar bands (DIBs) are similar, -12 and -16 km s^{-1}, respectively.

Table 3. Equivalent widths of absorption lines in the spectrum of V1853 Cyg

λ, Å	Species	W_λ, mÅ (Garcia-Lario *et al.* 1997)	W_λ, mÅ
4906.817	O II	99	104
4921.931	He I	200	530
4925.343	S II	150	147
4943.006	O II	73	133
5002.703	N II	41	165
5005.150	N II	49	145
5010.621	N II	42	130
5015.678	He I	70	63
5045.099	N II	109	228
5160.026	O II	77	92
5639.477	Si II	61	59
5666.629	N II	101	212
5676.017	N II	111	226
5679.558	N II	153	376
5686.213	N II	33	115
5696.604	Al III	176	254
5710.766	N II	78	110
5722.730	Al III	134	159
5739.734	Si III	247	375
6402.246	Ne I	210	187
6578.052	C II	303	191
6678.154	He I	330	88
6721.358	O II	137	219

It was of interest to test the conclusion by Garcia-Lario *et al.* (1997) about the mass-loss episode that occurred in 1993–1995. To this end, we compared the profile of the He I λ6678 Å line observed on June 12/13, 2000, with the 1992–1995 observations of the above authors. In Fig. 4e, we clearly see an intense emission component of the He I λ6678 Å line; thus, mass outflow from the star was also observed in 2000. In our view, there is a variable stellar wind on short (of the order of several days) time scales, as confirmed by photometric variability and by variability of the radial velocities determined from emission lines.

COMPARISON OF V1853 Cyg WITH V886 Her

The photometric behavior of V1853 Cyg on a time scale of several years bears a striking similarity to that of another protoplanetary object, the B1-supergiant V886 Her (Arkhipova *et al.* 1996, 1998, 2001a). Like V1853 Cyg, V886 Her exhibits rapid erratic light variations with amplitudes $\Delta V \sim 0\overset{m}{.}3$, $\Delta B \sim 0\overset{m}{.}3$, and $\Delta U \sim 0\overset{m}{.}4$ and no correlations between color and magnitude. However, a trend in the mean brightness is observed in V886 Her: the star has dimmed by $\sim 0\overset{m}{.}5$ in V since the 1970s, whereas the mean brightness of V1853 Cyg has not changed in 27 years. V886 Her also exhibited rapid spectral evolution, while V1853 Cyg has remained an early-B star at least for the last 30 years.

Table 4. Equivalent widths of emission lines in the spectrum of V1853 Cyg

λ, Å	Species	W_λ, mÅ
4861.33	H I	1530
5041.06	Si II	85
5056.02	Si II	203
5158.80	[Fe II]	45
5875.6	He I	568
5889.95	Na I D_2	86
5957.61	Si II	157
5978.97	Si II	338
5999.47	N I	53
6032.30	Fe III	91
6347.09	Si II	371
6371.36	Si II	178
6449.21	[Zr II]	53
6548.1	[N II]	153
6562.8	H I	1150
6583.6	[N II]	>378
6633.78	O I	43
6678.15	He I	81
6717.0	[S II]	65
6731.30	[S II]	117
7065.19	He I	630

The absorption spectrum of V886 Her corresponds to a B1 supergiant with a temperature $T_{\rm eff} = 22000 \pm 500$ K (Partharathy *et al.* 2000). In contrast to the spectrum of V1853 Cyg, its emission spectrum is richer and contains numerous forbidden and permitted lines of ionized metals [Fe II], Fe II, [Fe III], [Cr II], [Ti II], Ti II, [V II], V II, [Zr II], [Ni II], [Cu II], [Mn II], neutral metals [Ni II], [Cr I], [Ti I], an intense [N II] λ5755 Å auroral line, as well as [O I] lines and an intense O I λ7002 Å line, which is absent from the spectrum of V1853 Cyg. Figure 5 shows portions of echelle spectra for V1853 Cyg and V886 Her. The difference between the emission

Table 5. Mean heliocentric radial velocities of V1853 Cyg as inferred from lines of various species

Species	Number of lines	V_r, km s^{-1}	$\sigma(V_r)$, km s^{-1}
O II a^*	29	−54	4
N II a	12	−51	3
C II a	6	−43	4
Si III a	5	−56	5
Al III a	3	−43	3
He II a	1	−49	0
H I e^{**}	3	−50	3
He I e	3	−54	10
[N II] e	2	−68	1
[S II] e	2	−85	0
Si II e	5	−68	2
Na I D_2 e	1	−85	0
Na I a	2	−12	0
DIB a	7	−16	5

Note: a^* is absorption, e^{**} is emission.

spectra stems from the fact that the shell of V886 Her, first, is excited by a hotter star and, second, has a higher density, which is estimated from [S II] lines to be $n_e = 2 \times 10^4$ см$^{-3}$, and is apparently more extended. Both stars exhibit variable H I and He I line profiles (Arkhipova *et al.* 2001a). As has been pointed out previously, the variations of the H I and He I line profiles in the spectrum of V886 Her may be related to the spectral evolution of the star. However, when comparing V886 Her and V1853 Cyg, we may assume the variations of the hydrogen- and helium-line profiles in the spectrum of V886 Her on a short time scale to be most likely the result of a variable stellar wind.

Given the similarity in photometric behavior and some spectral characteristics of V1853 Cyg and V886 Her, it may be assumed that these are related objects at the same stage of stellar evolution—on the way from AGB supergiants to young planetary nebulae. However, the times it take them to traverse this path differ markedly. As a more massive star ($M = 0.7M_\odot$), V886 Her evolves "before our eyes," traversing the path from A to early-B star in a hundred years. At the same time, in 30 years, V1853 Cyg did not approach on the Hertzsprung–Russell diagram to the hotter progenitors of planetary nebulae and, according to the theory of stellar evolution at late stages (Blocker 1995), must be less massive. We estimate it to be $\sim 0.6 M_\odot$.

CONCLUSIONS

Our photometric and spectroscopic observations of V1853 Cyg in 1999–2000 have led us to the following conclusions:

(1) Since the star is not a massive supergiant, it does not belong to the α Cygni type of variables; being most likely a post-AGB star together with another related object, V886 Her, it represents a new type of variables whose variability is associated with their evolutionary status.

(2) Given the peculiarities of its photometric variability, which cannot be explained by the short-period pulsations alone, and the P Cyg profiles of He I lines in the spectrum of V1853 Cyg, we assume that mass outflow from the star continues and that the time scale of stellar-wind intensity variations is of the order of a day.

(3) The star's mean brightness has not changed in 30 years, neither its spectral type and, consequently, its temperature characteristics — the star did not show any rapid evolutionary changes, in contrast to V886 Her. Therefore, we believe it to be a protoplanetary object of intermediate mass ($M \sim 0.6 M_\odot$).

Given the short time scales of light variations in V1853 Cyg, it is desirable to carry out further photometric observations of the star in an effort to reveal a possible periodic variability with $P < 1$ days and spectroscopic observations to confirm the stellar-wind variability as one of the causes of the star's rapid variability.

ACKNOWLEDGMENTS

This work was supported by the Russian Foundation for Basic Research [project nos. 99-02-18339 (V.A., N.I., R.N., G.K., V.E.) and 01-02-16530 (V.K.)].

REFERENCES

1. I. Appenzeller, Z. Astrophys. **64**, 269 (1966).
2. V. P. Arkhipova, N. P. Ikonnikova, V. F. Esipov, and R. I. Noskova, Pis'ma Astron. Zh. **22**, 526 (1996) [Astron. Lett. **22**, 470 (1996)].
3. V. P. Arkhipova, N. P. Ikonnikova, R. I. Noskova, *et al.*, Pis'ma Astron. Zh. **25**, 30 (1999) [Astron. Lett. **25**, 25 (1999)].
4. V. P. Arkhipova, N. P. Ikonnikova, R. I. Noskova, and G. V. Sokol, Pis'ma Astron. Zh. **26**, 705 (2000) [Astron. Lett. **26**, 609 (2000)].
5. V. P. Arkhipova, G. V. Sokol, and G. V. Klochkova, Pis'ma Astron. Zh. **27**, 122 (2001a) [Astron. Lett. **27**, 99 (2001a)].
6. V. P. Arkhipova, N. P. Ikonnikova, R. I. Noskova, *et al.*, Pis'ma Astron. Zh. **27**, 187 (2001b) [Astron. Lett. **27**, 156 (2001b)].
7. T. Blocker, Astron. Astrophys. **299**, 755 (1995).
8. J. S. Drilling, Astron. J. **80**, 128 (1975).
9. P. Garcia-Lario, M. Parthasarathy, D. De Martino, *et al.*, Astron. Astrophys. **326**, 1103 (1997).

10. P. N. Kholopov, N. N. Samus, E. V. Kazarovets, and N. N. Kireeva, Inf. Bull. Var. Stars, No. 3058, 1 (1987).
11. A. B. Meinel, A. F. Aveni, and M. W. Stockton, *Catalog of Emission Lines in Astronomical Objects* (Optical Scientific Center and Steward Observatory, Tucson, 1969).
12. Ch. E. Moore, *A Multiplet Table of Astrophysical Interest* (The Observatory, Princeton, 1945), Contrib. Princeton Univ. Obs., No. 20.
13. V. E. Panchuk, I. D. Najdenov, V. G. Klochkova, *et al.*, Bull. Spec. Astrophys. Obs. **44**, 127 (1998).
14. M. Parthasarathy, Astrophys. J. Lett. **414**, L109 (1993).
15. M. Parthasarathy, P. Garcia-Lario, T. Sivarani, *et al.*, Astron. Astrophys. **357**, 241 (2000).
16. V. V. Smith and D. L. Lambert, Astrophys. J. Lett. **424**, L123 (1994).
17. J. Stok, J. J. Nassau, and C. B. Stephenson, Hamburger Sternw., Warner and Swasey Obs. **2**, 1 (1960).
18. D. G. Turner, Astrophys. J. **88**, 650 (1983).
19. D. G. Turner and J. S. Drilling, Publ. Astron. Soc. Pac. **96**, 292 (1984).
20. T. Ueta, M. Meixner, and M. Bobrowsky, Astrophys. J. **528**, 861 (2000).
21. I. B. Voloshina, I. N. Glushneva, and V. T. Doroshenko, *Spectrophotometry of Bright Stars* (Nauka, Moscow, 1982).

Translated by A. Dambis

Astronomy Letters, Vol. 27, No. 11, 2001, pp. 728–731. Translated from Pis'ma v Astronomicheskiĭ Zhurnal, Vol. 27, No. 11, 2001, pp. 850–853.

Estimation of Errors in the Distances to Intrinsically Reddened Stars

R. M. Raznik and O. V. Agafonova*

Ulyanovsk State University, Ulyanovsk, Russia

Received May 11, 2001

Abstract—We show that adding the intrinsic color excess ΔE_{B-V} of a star to the interstellar E_{B-V} can significantly change the estimate of its distance r. When ΔE_{B-V} changes from $0\overset{m}{.}0$ to $0\overset{m}{.}5$, the relative error δ in the estimated distance rapidly increases to 99.5%. For $\Delta E_{B-V} > 0\overset{m}{.}5$, r cannot be determined from the distance modulus. The error δ depends neither on absolute magnitude M_V, nor on apparent magnitude m_V, nor on interstellar extinction but depends only on the star's intrinsic reddening ΔE_{B-V}. We provide quantitative estimates of the intrinsic reddening in stars. The mean values of $\overline{\Delta E_{B-V}}$ for B0 stars in open clusters and associations are $0\overset{m}{.}2$ and $0\overset{m}{.}35$, respectively; $\overline{\Delta E_{B-V}}$ for Be stars is $0\overset{m}{.}1$–$0\overset{m}{.}2$; the effect of cooler companions on the color indices of OB stars can vary. The individual values of ΔE_{B-V} for separate OB stars exceed $0\overset{m}{.}5$ and reach $0\overset{m}{.}6$–$0\overset{m}{.}7$. We show that the intrinsic reddening of cluster stars produced by circumstellar gas–dust envelopes can be separated from the interstellar reddening even for the same extinction law. © 2001 MAIK "Nauka/Interperiodica"

Key words: *star clusters and associates, circumstellar envelopes, interstellar extinction*

INTRODUCTION

The practical importance of accurately estimating the distances to stars, particularly to OB stars, is difficult to overestimate. Large errors in the estimated distances arise when the star has an intrinsic reddening mistaken for an interstellar one. There are methods that allow intrinsic reddening in some stars to be revealed and quantitatively estimated. Here, our goal is to estimate the possible errors in the distances to stars whose intrinsic reddening is disregarded.

RELATIVE ERRORS IN THE DISTANCES TO INTRINSICALLY REDDENED STARS

The relative error in the distance to a star when its intrinsic reddening is ignored is

$$\delta = \frac{r_1 - r}{r} \times 100\%, \qquad (1)$$

where r_1 is the distance to the star calculated from the actual interstellar reddening E_{B-V},

$$\log r_1 = 1 + 0.2\,(m_V - 3E_{B-V} - M_V)\,, \qquad (2)$$

and r is the distance calculated under the erroneous assumption that all of the reddening (both actual interstellar E_{B-V} and intrinsic circumstellar ΔE_{B-V}) is interstellar:

$$\log r = 1 \qquad (3)$$
$$+ 0.2[m_V - (3E_{B-V} + 3\Delta E_{B-V}) - M_V].$$

Our calculations show that the relative error rapidly increases and reaches 100% even at $\Delta E_{B-V} = 0\overset{m}{.}5$:

$$0 < \Delta E_{B-V} < 0\overset{m}{.}5, \quad 0 < \delta < 100\%. \qquad (4)$$

Figure 1 shows an increase of the relative error in the distance δ with intrinsic reddening of a star ΔE_{B-V}. We see from Fig. 2 that as the star's intrinsic reddening ΔE_{B-V} increases, its calculated distance r decreases, while the difference $\Delta r = r_1 - r$ increases. At $\Delta E_{B-V} = 0\overset{m}{.}5$, the error Δr is equal to the distance r to be determined. For $\Delta E_{B-V} > 0\overset{m}{.}5$, the difference Δr is larger than r, and the distance determination without allowance for the star's intrinsic reddening loses its meaning altogether.

In addition, it has emerged that δ calculated from the apparent magnitude m_V, absolute magnitude M_V, interstellar reddening E_{B-V}, and intrinsic reddening ΔE_{B-V} of a star is by no means a function of all these quantities but depends solely on the star's intrinsic reddening. Indeed, substituting (2) and (3) in (1) yields

$$\delta = \frac{10^{1+0.2m_V-0.6E_{B-V}-0.2M_V}(1 - 10^{-0.6\Delta E_{B-V}})}{10^{1+0.2m_V-0.6E_{B-V}-0.2M_V} \times 10^{-0.6\Delta E_{B-V}}} \qquad (5)$$
$$\times 100\% = \left(10^{0.6\Delta E_{B-V}} - 1\right) \times 100\%,$$

i.e.,

$$\delta = f(\Delta E_{B-V}). \qquad (6)$$

Thus, it follows that the error δ depends neither on the spectral type, nor on the luminosity class

*E-mail: maxag@mail.uln.ru

1063-7737/01/2711-0728$21.00

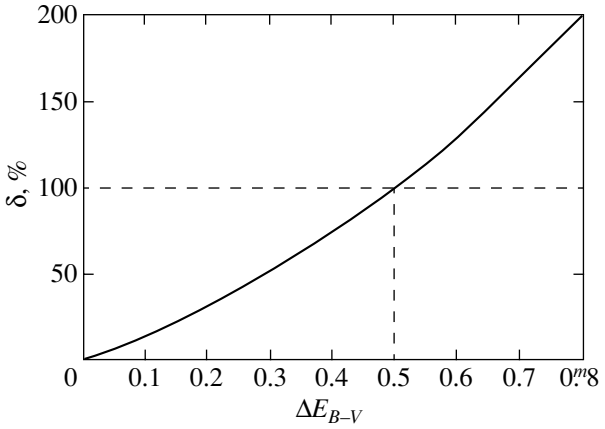

Fig. 1. Relative error δ in the distance to a star *versus* intrinsic color excess ΔE_{B-V}.

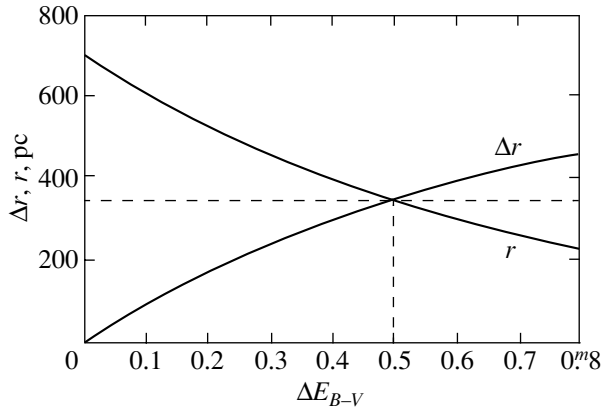

Fig. 2. The distance r to a star calculated with its intrinsic reddening ignored and the associated error Δr *versus* intrinsic color excess ΔE_{B-V}.

expressed by the absolute magnitude, nor on the apparent brightness of a star, nor on the interstellar extinction but depends solely and significantly on the star's intrinsic reddening.

QUANTITATIVE ESTIMATES OF THE INTRINSIC REDDENING IN OB STARS

The interstellar extinction from the Sun to a cluster is determined, on average, from all cluster stars. However, it was noticed that the reddening of O–B3 stars is larger than that of later-type cluster members, i.e., many OB stars exhibit an intrinsic excess reddening (Raznik 1965a). The excess reddening averaged within each spectral subtype reaches a maximum in the subtype B0, falls off to the subtypes B3 and O9, O8, and again increases in hotter O stars. For B0 stars of clusters and associations, $\Delta\overline{E_{B-V}} = 0\overset{m}{.}2$ and $\Delta\overline{E_{B-V}} = 0\overset{m}{.}35$, respectively. However, there are stars with a very large intrinsic reddening. For instance, ΔE_{B-V} of some stars in the cluster NGC 6530 reaches $0\overset{m}{.}6$; the largest ΔE_{B-V} in the cluster NGC 6531 is $0\overset{m}{.}5$; in the cluster χ Per, it is also $0\overset{m}{.}5$; in the cluster NGC 6611, it reaches $0\overset{m}{.}7$; and in the associations Cep III, Cep IV, and Cyg VI, it is $0\overset{m}{.}6$, $0\overset{m}{.}7$, and $0\overset{m}{.}7$, respectively (Raznik 1967a).

PHENOMENA RESPONSIBLE FOR THE INTRINSIC REDDENING OF STARS

Later-type stars with a large intrinsic reddening have been found near O5 stars that reddened only slightly or did not redden at all. Thus, for example, there is star no. 76 (B5, $\Delta E_{B-V} = 0\overset{m}{.}35$) in the cluster NGC 7510 near star no. 3, star no. 73 (B8, $\Delta E_{B-V} = 0\overset{m}{.}75$) in the cluster NGC 1893 near star no. 13, star no. 82 (B8, $\Delta E_{B-V} = 0\overset{m}{.}60$) near star no. 2, and star no. 104 (B4, $\Delta E_{B-V} = 0\overset{m}{.}65$) near star no. 49. The O stars listed above are located in different parts of the cluster (Raznik 1965b). The cluster stars are numbered according to the catalog of Hoag *et al.* (1961).

The observed phenomenon can be explained by the fact that the strong stellar winds from early O stars drive away both their circumstellar envelopes and the interstellar matter in the cluster. The nearest stars are located the gas–dust condensations formed around O5 stars. The sizes and masses of such rings reach 0.1 pc and $10^{-4}M_{\odot}$, respectively. Of considerable interest is the work on cooler O9.5V stars by Massa (1995). These stars were shown to produce winds that disperse the circumstellar envelopes, freeing the photospheric emission of O9.5V stars from additional reddening. However, no objects reddened under the effect of the dispersed remnants of circumstellar matter have been found near stars of this type.

It would be reasonable to assume that still cooler B0–B3 stars could not drive away the matter and, hence, are surrounded by gas–dust envelopes. This assumption is confirmed by the fact that the extinction law for early B stars, to a first approximation, proves to be the same as that for interstellar clouds. This is seen on the two-color $(U-B)$–$(B-V)$ diagram for young clusters in Fig. 3, which shows the change in the appearance of the two-color diagrams for open clusters. The points were obtained by averaging the color excesses $\overline{E_{B-V}}$ and $\overline{E_{U-B}}$ within each spectral subtype. All the points corresponding to the cluster stars are displaced along the reddening line because of the interstellar extinction. The displacement of the points corresponding to reddened early B stars in the same direction is larger, suggesting an additional intrinsic reddening that follows

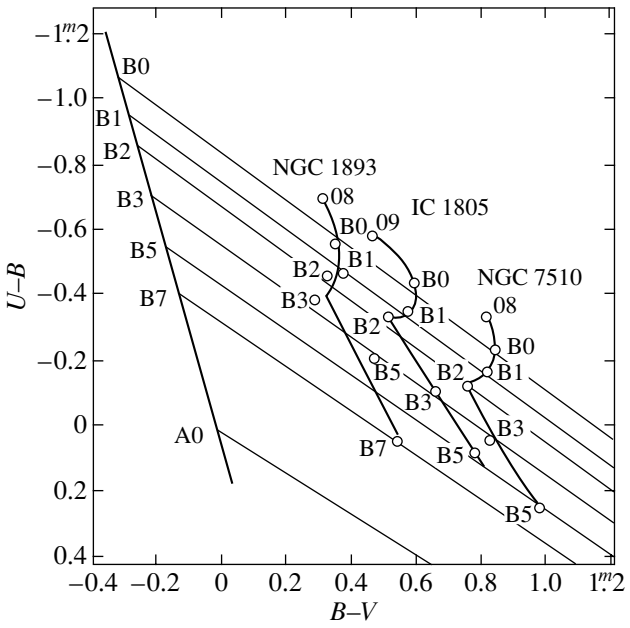

Fig. 3. Changes in the two-color diagrams for open clusters due to the displacement of the points corresponding to O8–B3 stars along the reddening lines.

the same law as in the interstellar medium. Thus, in clusters, the reddening of light from B stars in their circumstellar envelopes can be separated from the interstellar reddening even for the same extinction law.

The dispersion of points along the reddening line can be explained by the different orientation of the equatorward-flattened gas–dust envelopes relative to the line of sight. The displacement of the points perpendicular to the reddening lines is suggestive of different reddening mechanisms: the radiation from emission-line envelopes, the influence of close cooler companions on the continuum of the hot star, and others.

Be stars are known to be cooler and redder than B stars of the corresponding spectral subtypes; their $B-V$ and $U-B$ color indices do not change simultaneously and regularly. The mean $\overline{\Delta E_{B-V}}$ of B0e stars are a mere $0^m.1$, but in some stars, its value reaches $0^m.2$ and more (Raznik 1967b).

Of particular interest are close binary OB stars with cooler components. For example, a study of the star V1016 Ori has shown it to be a complex quadruple system containing a primary B0 star, an infrared companion, and an A0 companion with its dust envelope. Vitrichenko (1999) and Bondar' *et al.* (2000) emphasize that an A0 companion causes the system as a whole to redden. This effect is responsible for the abnormal reddening law.

One of the results of the detailed and comprehensive study of the star BM Ori by Vitrichenko and Larionov (1996) was the explanation of its excess reddening. The interstellar extinction A_V for BM Ori determined from its color excess is $1^m.37$ and turns out to be larger than that for the other Trapezium stars that form a spatial grouping. Allowance for the contribution to the continuum of the B3 V star from its close F0 companion accounts for the excess reddening of the star and results in a correction of its interstellar extinction. It proved to be a factor of 2 smaller: $A_V = 0^m.70$. Since this value is $0^m.2$ lower than the mean extinction for the other Trapezium stars, the authors do not rule out the possibility that the reddening of these stars is also related to the emission from their companions.

CONCLUSIONS

Adding the intrinsic color excess ΔE_{B-V} of a star to the interstellar excess E_{B-V} can significantly change the distance estimated from its modulus. When ΔE_{B-V} changes from $0^m.0$ to $0^m.5$, the relative error in the estimated distance δ rapidly increases to 99.5%.

The error δ depends neither on the star's spectral type, nor on its luminosity, nor on its apparent brightness, nor on the interstellar reddening but depends on ΔE_{B-V} alone. The derived law is of importance in determining the distances to OB stars, which are commonly used as distance indicators for the stellar systems containing them.

Below we provide quantitative estimates of the excess reddening in some stars. According to published data, the mean (within the spectral subtype) intrinsic reddening $\overline{\Delta E_{B-V}}$ of OB stars reaches a maximum in the subtype B0:

$$\overline{\Delta E_{B-V}} = 0^m.2 \quad \text{for cluster stars,}$$

$$\overline{\Delta E_{B-V}} = 0^m.35 \quad \text{for stars in associations.}$$

The excess reddening of some OB stars is larger than $0^m.5$ and reaches $0^m.6$–$0^m.7$ (Raznik 1965b, 1967a).

Among the excessively reddened stars, there are stars with gas–dust and emission-line envelopes, stars with close cooler companions, and others. The reddening of OB cluster stars with circumstellar gas–dust envelopes can be separated from the interstellar reddening even for the same extinction laws.

Our quantitative estimates of ΔE_{B-V} give an idea of the possible errors in the distances to stars whose intrinsic reddening is disregarded.

REFERENCES

1. N. I. Bondar', E. A. Vitrichenko, and M. M. Zakirov, Pis'ma Astron. Zh. **26**, 525 (2000) [Astron. Lett. **26**, 452 (2000)].
2. A. A. Hoag, H. L. Johnson, B. Iriarte, *et al.,* Publ. U. S. Naval Obs., Ser. 2 **17**, 7 (1961).
3. D. Massa, Astrophys. J. **438**, 376 (1995).
4. R. M. Raznik, Izv. Krym. Astrofiz. Obs. **33**, 301 (1965a).
5. R. M. Raznik, Izv. Krym. Astrofiz. Obs. **34**, 225 (1965b).
6. R. M. Raznik, Izv. Krym. Astrofiz. Obs. **36**, 264 (1967a).
7. R. M. Raznik, Izv. Krym. Astrofiz. Obs. **37**, 262 (1967b).
8. É. A. Vitrichenko, Pis'ma Astron. Zh. **25**, 220 (1999) [Astron. Lett. **25**, 179 (1999)].
9. É. A. Vitrichenko and V. M. Larionov, Pis'ma Astron. Zh. **22**, 178 (1996) [Astron. Lett. **22**, 157 (1996)].

Translated by G. Rudnitskiĭ

Astronomy Letters, Vol. 27, No. 11, 2001, pp. 732–736. Translated from Pis'ma v Astronomicheskiĭ Zhurnal, Vol. 27, No. 11, 2001, pp. 854–858.

Diffusion Tensor for Galactic Cosmic Rays in the Interplanetary Medium with a Magnetic Field

Ye. K. Kazkenov*

Kokshetau State University, Kokshetau, Kazakhstan

Received May 22, 2001

Abstract—The Boltzmann kinetic equation is analyzed in the MHD approximation. This analysis requires an explicit expression for the collision integral F_c. In the classical theory, $F_c = -\nu f_\mu^{(1)}\Omega_\mu$, where $f_\mu^{(1)}$ is the first spherical harmonic in the Galactic-cosmic-ray (GCR) distribution, Ω_μ are the components of a unit particle velocity vector, and the frequency ν of collisions between GCRs and interplanetary magnetic-field nonuniformities is assumed to be a scalar. The assumption that ν_{ij} is a tensor (which is the result of anisotropy in the interplanetary medium) distinguishes this study from others. Since the anisotropic GCR effects in the heliomagnetosphere are marginal, the nondiagonal elements of tensor ν_{ij} were set equal to zero. Our analysis has yielded the diffusion-tensor components $D_{||}$, $D_\perp$, and D_A, which are expressed in terms of interplanetary parameters. The energy dependencies of $D_{||}$, $D_\perp$, and D_A are in good agreement with the experimental data and calculations by other authors. © 2001 MAIK "Nauka/Interperiodica"

Key words: *cosmic rays, nonthermal emission*

INTRODUCTION

The interplanetary propagation of Galactic cosmic rays (GCRs) is generally described by the Boltzmann kinetic equation

$$\frac{\partial f}{\partial t} + \mathbf{V}\frac{\partial f}{\partial \mathbf{r}} + \omega\,[\mathbf{p}\times\mathbf{b}]\,\frac{\partial f}{\partial \mathbf{p}} = F_c, \qquad (1)$$

where f is the distribution function; $\mathbf{r}$, $\mathbf{V}$, $\mathbf{p}$, and ω are the radius vector, velocity, momentum, and Larmor frequency of the particle, respectively; $\mathbf{b}$ is a unit magnetic induction vector of the interplanetary magnetic field (IMF); and F_c is the collision integral. In Eq. (1), the convection and particle magnetic drift are disregarded to focus attention on the diffusion.

The components of the GCR diffusion tensor in interplanetary space are derived in Section 1. In Section 2, we show that the GCR diffusion tensor components can be expressed in principle in terms of interplanetary parameters. The applicability range of the derived relations are qualitatively analyzed in Section 3.

1. GCR DIFFUSION CURRENT IN THE MHD APPROXIMATION

The explicit form of F_c must be known to solve Eq. (1). Let us expand the function f in a series in small parameter $\mathbf{\Omega}$ (unit particle velocity vector) and restrict ourselves to the zeroth and first moments of the distribution function:

$$f = f^{(0)} + f_\alpha^{(1)}\Omega_\alpha, \qquad (2)$$

where Ω_α are the components of the unit velocity vector.

In the classical theory (Krymskiĭ and Transkiĭ 1973), the collision integral is postulated in the form $F_c = -\nu f_\mu^{(1)}\Omega_\mu$, where the frequency of collisions between GCRs and IMF nonuniformities ν is a scalar. This expression for F_c holds for a relatively dense plasma in a weak magnetic field.

However, the GCR density is so low that the magnetic-field effect on the particle motion is significant. This is confirmed by numerical simulations of the particle motion in the IMF, which show a large discrepancy between the classical theory and calculations (Giacolone *et al.* 1999). Therefore, we assume the collision integral to be a tensor, ν_{ij}.

The diagonal elements of tensor ν_{ij} are directly related to collisional processes, whereas the nonsymmetric part of ν_{ij} is related to anisotropic effects. Since the latter are negligible in the heliomagnetosphere, the nondiagonal elements of tensor ν_{ij} were assumed to be zero. In that case,

$$\nu_{ij} = \begin{pmatrix} \nu_{||} & 0 & 0 \\ 0 & \nu_\perp & 0 \\ 0 & 0 & \nu_\perp \end{pmatrix}.$$

*E-mail: space@mail.kz

1063-7737/01/2711-0732$21.00

Using expansion (2), let us write out Eq. (1) component by component, multiply it by Ω_σ, and average it over all directions. The quasi-steady-state Boltzmann kinetic equation then takes the form:

$$\frac{V}{3}\frac{\partial f^{(0)}}{\partial x_\sigma} + \omega e_{\alpha\sigma\gamma} b_\gamma f_\alpha^{(1)} = -\nu_{\sigma\sigma} f_\sigma^{(1)}. \qquad (3)$$

Below, we use the rule of summation over the dummy indices.

Since the differential particle density and the current density are, respectively,

$$n = 4\pi p^2 f^{(0)}, \quad j_\mu = \frac{4\pi p^2 V}{3} f_\mu^{(1)}, \qquad (4)$$

Eq. (3) can be written as

$$\frac{V^2}{3}\nabla n + \omega\,[\mathbf{b}\times\mathbf{j}] = -\nu_{||}\mathbf{j}_{||} - \nu_\perp \mathbf{j}_\perp. \qquad (5)$$

Equation (5) is a standard MHD equation in which abrupt changes in the GCR current are disregarded and the collection of cosmic-ray particles is represented as an incompressible fluid.

Solving Eq. (5) for $\mathbf{j}$ yields

$$\mathbf{j} = -\frac{V^2}{3\nu_{||}}\nabla_{||} n - \frac{V^2\nabla_\perp n}{3\nu_\perp\left(1+\left(\frac{\omega}{\nu_\perp}\right)^2\right)} + \frac{V^2\omega\,[\mathbf{b}\times\nabla n]}{3\nu_\perp^2\left(1+\left(\frac{\omega}{\nu_\perp}\right)^2\right)}.$$

Assuming that $\mathbf{j} = -D_{||}\nabla_{||} n - D_\perp \nabla_\perp n - D_A\,[\mathbf{b}\times\nabla n]$, $\lambda_{||} = V/\nu_{||}$, $\lambda_\perp = V/\nu_\perp$, and $\rho = V/\omega$, we obtain

$$D_{||} = \frac{\lambda_{||} V}{3}, \quad D_\perp = \frac{1}{3}\frac{\lambda_\perp V}{1+\left(\frac{\lambda_\perp}{\rho}\right)^2}, \qquad (6)$$

$$D_{\rm A} = -\frac{1}{3\rho}\frac{\lambda_\perp^2 V}{1+\left(\frac{\lambda_\perp}{\rho}\right)^2} = -\frac{\lambda_\perp}{\rho}D_\perp,$$

where $D_{||}$, $D_\perp$, and $D_{\rm A}$ are, respectively, the diffusion tensor components along and across the IMF and the antisymmetric part of the diffusion tensor.

Thus, for the diffusion tensor components to be derived, we must determine the scattering mean free paths $\lambda_\perp$ and $\lambda_{||}$.

2. DETERMINING $\lambda_\perp$ AND $\lambda_{||}$

2.1. Models

The GCR propagation in the heliomagnetosphere in our approximation can be represented as the deflection of particles by a regular helical magnetic field and the scattering by nonuniformities.

The regular field deflects charged particles. Consequently, the scattering mean free path (this term is something of a misnomer; here it should be understood as the mean free path before the particle deflection by the field through an angle $\pi/2$) $\lambda_{\rm p} = \rho$, where ρ is the particle Larmor radius.

Let us now consider the effect of IMF nonuniformities with a scale size l. Their action is scattering in nature. In the case of magnetic-field fluctuations in absolute value, the particle scattering mean free path is $\lambda_{\rm h} \sim \dfrac{N}{n\sigma}$, where the number of particle collisions with nonuniformities for a deflection through $\pi/2$ is

$$N = \frac{\pi^2}{16\arctan^2\dfrac{\alpha l}{2\rho}}, \qquad (7)$$

$n \sim d^{-3}$ is the density of nonuniformities, d is the separation between them, $\sigma \sim l^2$ is the cross section for particle interaction with a nonuniformity, $\alpha = 1 + \dfrac{\delta B}{B}$, δB is the magnetic-field fluctuation in nonuniformities, and B is the induction of the regular IMF. Below, we assume, for definiteness, that $\alpha = 1.5$.

Since l and d are of the same order of magnitude, we obtain

$$\lambda_n = \frac{Cl}{\arctan^2\dfrac{\alpha l}{2\rho}},$$

where $C \sim \dfrac{\pi^2}{16}\left(\dfrac{d}{l}\right)^3$ is the proportionality factor, which generally depends on the radial distance.

Joining the two cases yields the scattering mean free path for the particle propagation across a regular magnetic field:

$$\lambda_\perp = \frac{\rho}{1+\dfrac{\rho}{Cl}\arctan^2\dfrac{\alpha l}{2\rho}}.$$

For the particle propagation along a regular magnetic field, the latter will not affect the scattering mean free path:

$$\lambda_{||} = \frac{Cl}{\arctan^2\dfrac{\alpha l}{2\rho}}.$$

Table 1. Calculation of $\gamma_1(R)$ for $R_0 = 1$ GV and $\gamma_2(R)$ for $R_1 = 5$ GV

R, GV	0.10	0.16	0.25	0.40	0.63	1.0	1.6	2.5	4.0	6.3	10	16	25
$\gamma_1(R)$	0.40	0.47	0.55	0.67	0.82	1.05	1.19	1.36	1.50	1.60	1.67	1.72	1.76
$\gamma_2(R)$	0.61	0.62	0.64	0.67	0.71	0.75	0.80	0.87	0.94	1.02	1.10	1.18	1.25

Table 2. Calculation of $\gamma_1(R)$ for $R_0 = 1.4$ GV and $\gamma_2(R)$ for $R_1 = 13$ GV

R, GV	0.10	0.16	0.25	0.40	0.63	1.0	1.6	2.5	4.0	6.3	10	16	25
$\gamma_1(R)$	0.30	0.32	0.40	0.47	0.58	0.65	0.90	1.08	1.25	1.39	1.50	1.58	1.63
$\gamma_2(R)$	0.54	0.55	0.56	0.57	0.59	0.61	0.63	0.67	0.71	0.76	0.82	0.89	0.97

Passing to the particle rigidity using the relation $\rho[\text{cm}] = \dfrac{R\,[\text{volts}]}{300 \cdot B\,[\text{oersteds}]}$, we obtain

$$\lambda_{||} = \frac{1}{150B}\frac{CR_0}{\arctan^2\dfrac{\alpha R_0}{R}}, \qquad (8)$$

$$\lambda_{\perp} = \frac{1}{300B}\frac{R}{1+\frac{R}{2CR_0}\arctan^2\dfrac{\alpha R_0}{R}},$$

where $R_0 = 150lB$ is a parameter, the quantities R and R_0 are given in volts, B is in oersteds, and $\lambda_{\perp}$ and $\lambda_{||}$ are in cm.

Let us now determine C and R_0 based on interplanetary magnetic measurements (Hedgecock 1975; NASA NSSDC 1998).

2.2. Determining R_0

Having analyzed the frequency spectra of magnetic-field fluctuations, Hedgecock (1975) obtained

$$D_{||} \sim R^{2-\nu}\beta \quad \text{for} \quad R \ll R_1,$$
$$D_{||} \sim R^2\beta \quad \text{for} \quad R \gg R_1,$$

and

$$D_{\perp} \sim R^{\nu}\beta \quad \text{for} \quad R \ll R_1,$$
$$D_{\perp} \sim R^2\beta \quad \text{for} \quad R \gg R_1.$$

Here, R_1 is a parameter that varies with solar cycle, and $1 < \nu \le 2$ is the power-law index of the frequency spectrum for IMF fluctuations. To describe both cases, the following relation (Ashirov 1983) was used:

$$D_{||} \sim R^{0.5}\left(1+\frac{R}{R_1}\right)^{1.5}\beta. \qquad (9)$$

Representing $D_{||} \sim R^{\gamma(R)}\beta$, we find $\gamma_1(R)$ from formula (6) and $\gamma_2(R)$ from formula (9). The results for the minimum value of $R_1 = 5$ GV from Hedgecock (1975), which corresponds to $R_0 = 1$ GV (these values are apparently typical of low solar activity) are presented in Table 1, while the results for the maximum value of $R_1 = 13$ GV and the corresponding $R_0 = 1.4$ GV (these values are apparently typical of relatively high solar activity) are presented in Table 2.

As we see, $R_0 \sim 1$–2 GV changes only slightly with solar cycle. Assuming the nonuniformity scale size l to be independent of solar activity and equal to 1.5×10^{11} cm, we obtain the IMF strength near the Earth's orbit $H_0 = 4.4\gamma$ at solar minimum and $H_0 = 6.2\gamma$ at solar maximum, in agreement with the NASA NSSDC results (1998).

It can be shown that for $R \ll R_1$, $D_{\perp}$ also has a satisfactory energy dependence, whereas for $R \gg R_1$, $D_{\perp}$ is proportional to R rather than to R^2. Consequently, for such energetic particles (50 GeV or more), the formula for $D_{\perp}$ is inapplicable (see Section 3).

2.3. Determining the Coefficient C

It follows from (6) that the degree of IMF nonuniformity is

$$\alpha = \frac{D_{\perp}}{D_{||}} = \left[1+\frac{2CR_0}{R\arctan^2\dfrac{\alpha R_0}{R}}\right]^{-1} \qquad (10)$$
$$\times\left[1+\left(1+\frac{R\arctan^2\dfrac{\alpha R_0}{R}}{2CR_0}\right)^{-2}\right]^{-1}.$$

Given R_0 and α_0 (the degree of IMF nonuniformity for particles with $R = 1$ GV) (Hedgecock 1975), we can determine C at the Earth's orbit: $C \sim 1.5$ at solar minimum and $C \sim 3$ at solar maximum. If l depends linearly on r (uniform expansion), then C does not change with distance from the Sun.

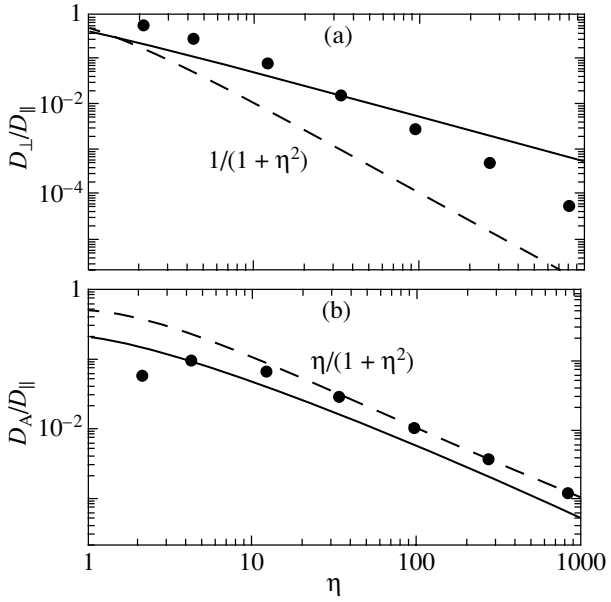

Fig. 1. Calculation of (a) $D_\perp/D_{||}$ and (b) $D_A/D_{||}$ (the solid line, dots, and the dotted line represent our calculations with formula (6), the calculations by Giacolone *et al.* (1999), and the calculations using the classical theory [formulas (11)], respectively).

3. APPLICABILITY RANGE

The reasoning of this section is qualitative, because it is difficult to accurately describe the conditions under which the MHD treatment is valid.

(1) The MHD approximation assumes that the macroscopic quantities used to describe the phenomenon under consideration change only slightly on the mean free path (Pikel'ner 1966)

$$\frac{\lambda}{n}|\nabla n| \ll 1, \quad \frac{\lambda}{\bar{\varepsilon}}|\bar{\varepsilon}| \ll 1, \quad \frac{\lambda}{B}|\nabla B| \ll 1,$$

where $\bar{\varepsilon}$ is the mean energy of the particles.

(2) We disregard the term $\dfrac{\partial f}{\partial t}$ when deriving Eq. (5), because our treatment is quasi-steady-state and requires the absence of any abrupt changes in the cosmic-ray current (in particular, Forbush effects), which is true for the model of a quiet solar wind (Parker 1965).

(3) When deriving formula (7), we used the model of a leading center, which is applicable for

$$\frac{T}{n}\left|\frac{\partial B}{\partial t}\right| \ll 1, \quad \frac{\rho}{B}|\nabla B| \ll 1, \quad \frac{V_{||}T}{B}|\nabla B| \ll 1,$$

where $T = \dfrac{2\pi}{\omega}$ is the period of particle gyration along a regular IMF line, and $V_{||}$ is the particle velocity component along the magnetic field (Alfven and Falthemmer 1967).

CONCLUSIONS

The diffusion tensor for GCRs in the heliomagnetosphere is described by Eqs. (6) for GCR particles with $R = 20$ GV. The derived expression (6) for $D_\perp$ and $D_{||}$ have energy dependencies that are in agreement with the experimental data obtained from measurements of the frequency spectrum for IMF fluctuations. In the approximation of a dense plasma in a weak magnetic field ($\lambda_\perp \approx \lambda_{||} = \lambda \ll \rho$), Eqs. (6) take the classical form

$$D_{||} = \frac{\lambda V}{3}, \quad D_\perp = \frac{1}{3}\frac{\lambda V}{1+\left(\dfrac{\lambda}{\rho}\right)^2}, \qquad (11)$$

$$D_A = -\frac{1}{3\rho}\frac{\lambda^2 V}{1+\left(\dfrac{\lambda}{\rho}\right)^2}.$$

The figure shows the plots of $\dfrac{D_\perp}{D_{||}}$ and $\dfrac{D_A}{D_{||}}$ against $\eta = \dfrac{\lambda_{||}}{\rho}$ calculated from Eqs. (6). Also shown for comparison are the results by Giacolone *et al.* (1999) and $\dfrac{D_\perp}{D_{||}}$ and $\dfrac{D_A}{D_{||}}$ calculated from formulas (11). The discrepancy between our $\dfrac{D_\perp}{D_{||}}$ curve and the calculations by Giacolone *et al.* (1999) for $\eta < 5$ is insignificant, because this case is virtually unrealizable in interplanetary space; the discrepancy for $\eta > 100$ stems from the fact that in this range, our approximation is inapplicable. The nonsymmetric diffusion tensor component D_A includes only the Hall diffusion, and, as a result, our $\dfrac{D_A}{D_{||}}$ curve lies below the computed points (Giacolone *et al.* 1999). Therefore, for the problems of GCR modulation in the heliomagnetosphere to be solved quantitatively, the particle drift attributable to a gradient in the large-scale IMF and to IMF-line curvature must also be taken into account.

The unsteady-state equation for GCR transport in the heliomagnetosphere is

$$\frac{\partial n}{\partial t} = \frac{\partial}{\partial x_i}\left(D_{ij}\frac{\partial n}{\partial x_j}\right) - (u_i + V_{d,i})\frac{\partial n}{\partial x_i} + \frac{1}{3}\frac{\partial Rn\partial u_i}{\partial R\partial x_i},$$

where u_i are the components of the solar-wind velocity vector, and $V_{d,i}$ are the velocity vector components for the magnetic GCR drift attributable to a gradient in the large-scale IMF and IMF-line curvature (Florinski and Jokipii 1999).

Rivin (1998) asserts that the GCR intensity correlates more closely with interplanetary parameters than with geomagnetic and heliomagnetic indices. In light of this assertion, our attempt to express the diffusion tensor components in terms of interplantary parameters appears logical. Good agreement with the experimental data and calculations by other authors confirm the possibility of using our results to solve the problems of moderate-energy ($0.1 < R < 20$ GV) GCR modulation.

ACKNOWLEDGMENTS

I wish to thank Prof. A.A. Aĭtmukhambetov and Prof. R.R. Ashirov for help in preparing the manuscript.

REFERENCES

1. H. Alfven and C.-G. Falthammer, *Cosmical Electrodynamics* (Oxford Univ. Press, London, 1963; Mir, Moscow, 1967).
2. R. R. Ashirov, Candidate's Dissertation in Mathematical Physics (Kaz. Gos. Univ. im. S. M. Kirova, Alma-Ata, 1983).
3. J. Giacolone, J. R. Jokipii, and J. Kota, in *Proceedings of the 26th International Cosmic Ray Conference, Utah, 1999,* Ed. by D. Kieda, p. 37.
4. V. Florinski and J. R. Jokipii, in *Proceeding of the 26th International Cosmic Ray Conference, Utah, 1999,* Ed. by D. Kieda.
5. R. C. Hedgecock, Sol. Phys. **42**, 497 (1975).
6. G. F. Krymskiĭ and I. A. Transkiĭ, in *The Distribution of Galactic Cosmic Rays and the Dynamics of Structural Formations in the Solar Wind* (YF SO IKFIA, Yakutsk, 1973), p. 146.
7. E. N. Parker, *Interplanetary Dynamical Processes* (Interscience, New York, 1963; Mir, Moscow, 1965).
8. S. B. Pikelner, *Fundamentals of Cosmic Electrodynamics* (NASA, Washington, DC, 1964; Nauka, Moscow, 1966).
9. Yu. R. Rivin, Int. J. Geomagn. Aeron. **1** (3), (1998); http://www.eos.wdcb.rssi.ru/2000/gai99306/gai993096.htm.
10. NASA NSSDC, A Compilation of 1963–1997 Solar Wind Field and Plasma Data, Near Earth and Deep Space, Helio 001, USA, 1998.

Translated by V. Astakhov

Astronomy Letters, Vol. 27, No. 11, 2001, pp. 737–744. Translated from Pis'ma v Astronomicheskiĭ Zhurnal, Vol. 27, No. 11, 2001, pp. 859–866.

Acoustic Damping of Fast Kink Oscillations of Coronal Loops

Yu. T. Tsap[1,*] and Yu. G. Kopylova[2,3]

[1]*Crimean Astrophysical Observatory, p/o Nauchnyĭ, Crimea, 334413 Ukraine*
[2]*Kalmyk State University, Elista, Russia*
[3]*Pulkovo Astronomical Observatory, Russian Academy of Sciences, Pulkovskoe sh. 65, St. Petersburg, 196140 Russia*

Received November 16, 2000; in final formMay 18, 2001

Abstract—The damping of fast kink oscillations of solar coronal loops attributable to the radiation of MHD waves into the surroundings is considered in the thin-tube approximation. The oscillation damping decrement is calculated both by using a new energy method and by solving the dispersion equation for magnetic-tube eigenmodes. The two approaches are in good agreement under appropriate assumptions. The damping is negligible if MHD waves are radiated perpendicular to the magnetic field. The low Q factor of the loop oscillations in active regions found with the TRACE space telescope is associated with the generation of running waves that propagate along magnetic field lines. © 2001 MAIK "Nauka/Interperiodica"

Key words: *Sun, coronal loops, MHD oscillations, acoustic damping*

INTRODUCTION

With the launch of the TRACE space telescope in April 1998, it has become possible to investigate the transition region and the solar corona with a high spatial resolution ($<1''$) in the far ultraviolet (171 Å). One of the most interesting results obtained with this instrument was the detection of quasi-periodic transverse displacements of coronal loops in active regions with an amplitude of several thousand kilometers and a period close to 5 min (Aschwanden *et al.* 1999; Schrijver *et al.* 1999; Nakariakov *et al.* 1999; Schrijver and Brown 2000). The oscillations were observed at the initial phase of flare development immediately after the propagation of a disturbance at a velocity of 700 km s^{-1} (Aschwanden *et al.* 1999). Thus, it has been convincingly shown that the coronal-loop oscillations excited through flare energy release actually exist.

An interesting feature of the observed quasi-periodic displacements was their rapid damping: their amplitude during a few periods decreased by more than 50%. Having compared the observed and theoretical periods, Aschwanden *et al.* (1999) concluded that the loop oscillations in the solar corona were produced by standing waves of the fast kink mode. However, these wave modes are subject to weak damping because of ion viscosity and electron heat conductivity (Tsap 2000). Consequently, the following question arises: What is the cause of such strong damping of fast kink loop oscillations in the solar corona? Nakariakov *et al.* (1999) associated the observed oscillation damping with the resonant absorption of magnetohydrodynamic (MHD) waves in a turbulent plasma. Their analysis was, to a greater extent, qualitative. An increase in the viscosity and resistivity of a turbulent plasma by eight or nine orders of magnitude compared to those for an ideal plasma also seems unlikely. Based on the idea of flare sunquakes by Kosovichev and Zharkova (1998), Schrijver and Brown (2000) suggested that the oscillations of coronal loops were caused by quasi-periodic displacements of their footpoints in the photosphere, which are rapidly damped due to perturbations of the dense surroundings. In our view, this scenario cannot be considered justifiable enough, because the large-scale MHD waves excited by flare energy release are completely reflected from the lower solar atmosphere. We consider this issue in more detail in Section 3.

The so-called acoustic mechanism (Kleczek and Kuperus 1969, Zaitsev and Stepanov 1975, Spruit 1982, Ryutova 1988) may play a significant role in the damping of MHD oscillations of magnetic tubes. Its essence is that an oscillating magnetic tube can lose energy through the radiation of MHD waves into the surroundings. This phenomenon is similar to the radiation of acoustic waves by an oscillating membrane. The acoustic damping mechanism in

*E-mail: yur@crao.crimea.ua

1063-7737/01/2711-0737$21.00

the solar atmosphere was first considered by Kleczek and Kuperus (1969). A model in which filaments were represented as valves radiating acoustic waves was proposed to interpret the damping of prominence oscillations. However, this approximation disregards the action of electromagnetic forces, which are of crucial importance in the upper solar atmosphere. A more justifiable and detailed analysis of the acoustic damping mechanism is contained in Zaitsev and Stepanov (1975). The damping decrement of radial coronal-loop oscillations was determined from the dispersion equation for magnetic-tube eigenmodes. Despite its appeal, this approach (see also Spruit 1982, Kopylova and Tsap 2000) can lead to errors, because the transcendental equation is complex. Therefore, in our view, the method based on an analysis of energy relationships appears more convincing. In particular, Ryutova (1988) used the energy transfer equation for a wave packet to estimate the acoustic damping decrement for MHD oscillations of magnetic tubes. However, it includes the wave group velocity, which cannot always be determined with the required accuracy from the dispersion equation. In addition, Ryutova (1988) restricted her analysis to the oscillations of magnetic tubes without an external magnetic field, which is unacceptable for coronal loops.

Here, we propose a new energy method to calculate the acoustic damping decrement for thin magnetic tubes, which we use to interpret the observed strong damping of coronal-loop oscillations in active regions. In Section 1, we present the equations that describe fast kink oscillations of magnetic tubes and the radiation of MHD waves into the surroundings produced by them; in Section 2, we estimate the acoustic damping decrement of oscillations by using both the energy conservation law and by solving the dispersion equation. Based on our results, in Section 3, we present our view of the problem of a low Q factor for fast kink loop oscillations.

1. FAST KINK OSCILLATIONS OF A THIN MAGNETIC TUBE AND THE RADIATION OF MHD WAVES

In single-fluid ideal magnetohydrodynamics, the equations of motion, induction, continuity, and entropy balance are

$$\rho\left(\frac{\partial \mathbf{v}}{\partial t}+(\mathbf{v}\nabla)\mathbf{v}\right)=-\nabla p+\frac{(\nabla\times\mathbf{B})\times\mathbf{B}}{4\pi}, \quad (1)$$

$$\frac{\partial \mathbf{B}}{\partial t}=\nabla\times(\mathbf{v}\times\mathbf{B}), \quad (2)$$

$$\frac{\partial \rho}{\partial t}+\nabla(\rho\mathbf{v})=0, \quad (3)$$

$$\frac{\partial S}{\partial t}+(\mathbf{v}\nabla)S=0. \quad (4)$$

where the entropy is $S=p\rho^{-\gamma}$, and the adiabatic constant is $\gamma=5/3$.

Let an axisymmetric magnetic tube [$\mathbf{B}_0=(0,0,B_z(r)$] be disturbed from the equilibrium by an external field. Assume that $\mathbf{v}=\mathbf{v}'$, $\rho=\rho_0+\rho'$, $p=p_0+p'$, and $\mathbf{B}=B_z\mathbf{e}_z+\mathbf{B}'$, where the subscript and the prime denote, respectively, the equilibrium and perturbed quantities, with the latter being proportional to $\delta f(r)\exp(-i\omega t+in\varphi+ikz)$. The following system of linearized equations can then be easily derived from Eqs. (1)–(4):

$$-i\omega\rho_0\delta v_r=-\frac{\partial}{\partial r}\left(\delta p+\frac{\delta B_zB_z}{4\pi}\right)+\frac{ikB_z}{4\pi}\delta B_r, \quad (5)$$

$$-i\omega\rho_0\delta v_\varphi=\frac{in}{r}\left(\delta p+\frac{\delta B_zB_z}{4\pi}\right)+\frac{ikB_z}{4\pi}\delta B_\varphi, \quad (6)$$

$$-i\omega\rho_0\delta v_z=-ik\delta p-\frac{kB_z}{4\pi\omega}\delta v_r\frac{\partial B_z}{\partial r}, \quad (7)$$

$$\delta B_r=-\frac{kB_z}{\omega}\delta v_r, \quad (8)$$

$$\delta B_\varphi=-\frac{kB_z}{\omega}\delta v_\varphi, \quad (9)$$

$$-i\omega\delta B_z=-\frac{1}{r}\frac{\partial}{\partial r}rB_z\delta v_r-\frac{inB_z}{r}\delta v_\varphi, \quad (10)$$

$$-i\omega\delta\rho+\frac{1}{r}\frac{\partial}{\partial r}r\rho_0\delta v_r+\frac{in}{r}\rho_0\delta v_\varphi+ik\rho_0\delta v_z=0, \quad (11)$$

$$-i\omega(\delta p-c_s^2\delta\rho)+\delta v_r\left(\frac{\partial p_0}{\partial r}-c_s^2\frac{\partial\rho_0}{\partial r}\right)=0, \quad (12)$$

where $c_s^2=\gamma p_0/\rho_0$ is the speed of sound.

Given the equilibrium condition

$$\frac{\partial}{\partial r}\left(p_0(r)+\frac{B_0^2(r)}{8\pi}\right)=0, \quad (13)$$

after simple but cumbersome transformations, relations (5)–(12) reduce to the system of equations that was first derived by Hain and Lüst (1958) (see also Appert *et al.* 1974):

$$i\rho_0(\omega^2-k^2v_A^2)\frac{1}{r}\frac{\partial}{\partial r}(r\delta v_r)=\omega\left(\mu^2-\frac{n^2}{r^2}\right)\delta P, \quad (14)$$

$$\omega\frac{\partial\delta P}{\partial r}=i\rho_0(\omega^2-k^2v_A^2)\delta v_r, \quad (15)$$

where $v_A=B_z/(4\pi\rho_0)^{1/2}$ is the Alfvèn velocity, $\delta P=\delta p+\delta B_zB_z/(4\pi)$ is the perturbation amplitude of the total pressure,

$$\mu^2=\frac{(k^2c_s^2-\omega^2)(\omega^2-k^2v_A^2)}{(v_A^2+c_s^2)(k^2c_T^2-\omega^2)}, \quad (16)$$

$$c_T^2 = \frac{v_A^2 c_s^2}{v_A^2 + c_s^2}.$$

If there is a whole number N of half-waves on the entire length of a magnetic tube with fixed ends, which corresponds to a coronal loop with its feet frozen in the photosphere, then a standing wave can be excited in it. In that case, representing the solution as

$$f' = \delta f(r)\exp(-i\omega t)(\exp(ikz + in\varphi) \pm \exp(-ikz - in\varphi)), \quad (17)$$

it can be concluded that Eqs. (14) and (15) will not change. This conclusion follows from the linear independence of the terms with the factors $\exp(ikz + in\varphi)$ and $\exp(-ikz - in\varphi)$, as well as from the invariance of Eqs. (14) and (15) when $-k$ and $-n$ are substituted for k and n.

Eliminating the perturbation in radial velocity v_r in (14) using (15) and assuming the plasma inside and outside the magnetic tube to be virtually homogeneous (thin-tube approximation), we obtain

$$\frac{1}{r}\frac{\partial}{\partial r}\left(r\frac{\partial \delta P}{\partial r}\right) - \left(\frac{n^2}{r^2} - \mu^2\right)\delta P = 0. \quad (18)$$

We write the solutions of the Bessel equation (18) for the internal (i) and external (e) parts of the magnetic tube as follows:

$$\delta P_i = C_1 Z_n(\mu_i r), \quad \delta P_e = C_2 Z_n(\mu_e r). \quad (19)$$

Here, C_1 and C_2 are constants, and the cylinder functions are

$$Z_n(\mu_i r) = \begin{cases} J_n(\mu_i r), & \mathrm{Re}\mu_i \gg \mathrm{Im}\mu_i \\ I_n(\mu_i r), & \mathrm{Re}\mu_i \ll \mathrm{Im}\mu_i, \end{cases}$$

$$Z_n(\mu_e r) = \begin{cases} H_n^{(1)}(\mu_e r), & \mathrm{Re}\mu_e \gg \mathrm{Im}\mu_e \\ K_n(\mu_e r), & \mathrm{Re}\mu_e \ll \mathrm{Im}\mu_e, \end{cases}$$

where $J_n(\mu_i r)$ and $I_n(\mu_i r)$ are the Bessel functions (of the first kind and modified); $H_n^{(1)}(\mu_e r)$ and $K_n(\mu_e r)$ are the Hankel and Macdonald functions, respectively. We emphasize that the behavior of the Macdonald function for a real argument is monotonic rather than oscillating. Therefore, if the solution in the external region is expressed in terms of $K_n(\mu_e r)$, the tube oscillations will not result in the generation of radially propagating waves.

We join the solutions inside and outside the tube based on the continuity conditions for the total pressure and radial velocity at the tube boundary, $r = a$, which suggests

$$\delta P_i(a) = \delta P_e(a), \quad v_{r_i}(a) = v_{r_e}(a). \quad (20)$$

The first equality follows from the equation of motion (1) (Trubnikov 1996), whereas the second equality follows from the integration of Eq. (14) from $(a - \xi)$ to $(a + \xi)$ and then letting ξ tend to zero.

Using (15) and (20), we derive the dispersion equation for the magnetic-tube eigenmodes

$$\rho_e(\omega^2 - k^2 v_{A_e}^2)\mu_i \frac{Z_n'(\mu_i a)}{Z_n(\mu_i a)} = \rho_i(\omega^2 - k^2 v_{A_i}^2)\mu_e \frac{Z_n'(\mu_e a)}{Z_n(\mu_e a)}, \quad (21)$$

where ρ_i and ρ_e are the equilibrium plasma densities inside and outside the tube, respectively, and $Z_n'(x) = dZ_n(x)/dx$. Let us expand the cylinder functions in a series by setting $n = 1$ (Watson 1949)

$$Z_1(\mu_i r) = \frac{\mu_i r}{2} - \frac{(\mu_i r)^3}{16} + \ldots, \quad (22)$$

$$Z_1(\mu_e r) = D\left(-\frac{1}{\mu_e r} + \frac{\mu_e r}{2}\ln\frac{\mu_e r}{2} + C\right) + \ldots,$$

where $C \approx 0.58$ is the Euler constant; and D is a coefficient, which is $2i/\pi$ for the Hankel function and 1 for the Macdonald function. Assuming the longitudinal component of the wave vector k to be real and setting $\omega = \omega_0$, we derive the dispersion relation for fast kink modes from (21) for $|\mu a| \ll 1$ using (22) (Spruit 1982, Roberts *et al.* 1984, Roberts 1995):

$$\omega_0^2 = k^2 \frac{\rho_i v_{A_i}^2 + \rho_e v_{A_e}^2}{\rho_i + \rho_e}. \quad (23)$$

Equation (23) describes the waves both inside and outside the tube. We emphasize that for $\mathrm{Re}\mu_e r \gg 1$ (Watson 1949),

$$H_n^{(1)}(\mu_e r) \approx \left(\frac{2}{\pi \mu_e r}\right)^{1/2} e^{i(\mu_e r - n\pi/2 - \pi/4)}; \quad (24)$$

i.e., the radial perturbations take the form of a running cylindrical wave with the wave vector component $k_r = \mu_e$. Consequently, for the region of space under consideration, we can determine the radial group velocity of the waves $v_{g_r} = \partial\omega_0/\partial\mu_e$. However, since, according to (16) and (21), the function ω_0 generally cannot be expressed in terms of the independent quantities μ_e and c_{s_e}, v_{g_r} is difficult to obtain from the dispersion equation (21). That is why using the energy transfer equation for a wave packet (Kadomtsev 1976)

$$\frac{\partial \varepsilon}{\partial t} + \nabla(\mathbf{v}_g \varepsilon) = 0,$$

where ε is the wave energy density, to determine the decrement of the acoustic damping attributable to the radial radiation of waves runs into serious difficulties. Below, we show that the approach based on an analysis of the energy conservation law is more fruitful.

2. CALCULATING THE ACOUSTIC DAMPING DECREMENT

In the MHD approximation, the energy conservation law without viscosity and heat conductivity can be represented as (Braginskiĭ 1963)

$$\frac{\partial \varepsilon}{\partial t} + \nabla \mathbf{q} = 0. \quad (25)$$

Here,

$$\varepsilon = \frac{1}{2}\rho v^2 + \frac{3}{2}p + \frac{B^2}{8\pi}, \quad (26)$$

$$q_\beta = \left(\frac{1}{2}\rho v^2 + \frac{5}{2}p\right) v_\beta + S_\beta, \quad (27)$$

where $\mathbf{S} = (c/(4\pi))\mathbf{E} \times \mathbf{B}$ is the Umov–Poynting vector. Taking into account the frozen-in condition for magnetic field lines

$$\mathbf{E} = -\frac{1}{c}\mathbf{v} \times \mathbf{B}$$

and substituting the last relation in (27), we derive the expression for the energy flux density

$$q_\beta = \left(\frac{1}{2}\rho v^2 + \frac{5}{2}p + \frac{B^2}{4\pi}\right) v_\beta - \frac{B_\alpha B_\beta}{4\pi} v_\alpha. \quad (28)$$

If running waves are excited in the equilibrium medium, then, because the perturbed quantities are small, taking $\omega = \omega_0 - i\nu$ and assuming $\nu \ll \omega_0$, we have instead of expressions (26) and (28)

$$\langle \varepsilon(t) \rangle = \frac{G}{2}\left(\frac{\rho_0 |\delta v|^2}{2} + \frac{c_s^2}{2}\,\frac{|\delta\rho|^2}{\rho_0} + \frac{|\delta B|^2}{8\pi}\right) e^{-2\nu t}, \quad (29)$$

$$\langle q_\beta(t) \rangle = G\left(|\delta P \delta v_\beta| - \frac{|\delta B_\alpha \delta v_\alpha|}{8\pi} B_\beta - \frac{|\delta B_\beta \delta v_\alpha|}{8\pi} B_\alpha\right) e^{-2\nu t}, \quad (30)$$

where $\langle \varepsilon(t) \rangle$ and $\langle q_\beta(t) \rangle$ are the period-averaged wave energy density and flux, respectively; $G = 1$; and the modulus sign denotes the product of complex conjugates. To derive relation (29), we expanded p in a small parameter ρ' using Eq. (4) and set $5/4\delta p \approx \delta p$. Including the coefficient G in (29) and (30) can be explained as follows.

Equations (29) and (30) were derived under the assumption that the waves could freely propagate in all directions. At the same time, when a standing wave is excited in the magnetic tube, Eqs. (26) and (27) must be averaged not only over time but also over space, in particular, over the z and φ coordinates. In this case, using relations (17), (26), and (27), we can show that the energy density $\langle \varepsilon(t) \rangle$ and the energy flux densities $\langle q_r(t) \rangle$ and $\langle q_\varphi(t) \rangle$ double compared to those for a running wave. Consequently, when a standing wave is excited in the tube, we must take $G = 2$ in (29) and (30).

Let the kink magnetic-tube oscillations generate radially propagating waves in the external medium ($\mathrm{Re}\mu_e \gg \mathrm{Im}\mu_e$). We separate a cylindrical volume that encloses a tube of length L, inside which the oscillation energy $W(t)$ far exceeds the wave energy. Integrating (25) over this volume using the obvious relations

$$\langle \varepsilon(t) \rangle = \langle \varepsilon \rangle e^{-2\nu t}, \quad \langle q_\beta(t) \rangle = \langle q_\beta \rangle e^{-2\nu t}, \quad (31)$$

we then obtain for the acoustic damping decrement

$$\nu = \frac{F_r}{2W}. \quad (32)$$

Here,

$$F_r = 2\pi r L \langle q_r \rangle \quad (33)$$

$$= 4\pi r L \left\{|\delta P \delta v_r| - \frac{|\delta B_r \delta v_z|}{8\pi} B_z\right\},$$

$$W = 2\pi L \int_0^\infty \langle \varepsilon \rangle r\, dr, \quad (34)$$

where W and F_r are the oscillation energy and the radial wave energy flux at time $t = 0$, respectively. Note that, as follows from (28), the radial energy flux is $\langle q_r \rangle = 0$ if the solution of the Bessel equation (18) can be expressed in terms of the Macdonald function $K_1(\mu_e r)$.

In the thin-tube approximation, assuming the terms of Eqs. (7) and (10)–(12) with the derivative of the unperturbed quantities with respect to r to be zero, we have

$$\delta v_z = \frac{\omega_0 k c_s^2}{\omega_0^2 - k^2 c_s^2}\,\frac{\delta B_z}{B_z}. \quad (35)$$

If the wave phase velocity is $v_p = \omega_0/k > c_s$, then we derive from (8), (33), and (35) for the radial wave flux

$$F_r = 4\pi r L |\delta P \delta v_r|. \quad (36)$$

We calculate the kink-oscillation energy W by using phase relations between perturbed quantities. Substituting (9) in (6) yields

$$\delta v \varphi = \frac{\omega_0 \delta P}{r\rho_0(k^2 v_A^2 - \omega_0^2)}. \quad (37)$$

For $|\mu r| \ll 1$, the cylinder functions Z_n and their derivatives $\partial Z_n/\partial r$ may be assumed to be either real or imaginary [see (22)]. Therefore, relations (7)–(9), (12), (15), (35), and (37) lead us to conclude that the perturbations in radial velocity v_r' and magnetic field B_r' vary in antiphase with the remaining perturbed parameters.

As follows from (26), the energy density of the standing waves in the magnetic tube averaged over z and φ can be represented as

$$\langle \varepsilon(t) \rangle \quad (38)$$

$$= 2e^{-2\nu t}\mathrm{Re}\left[\left(\frac{\rho_0 \delta v^2}{2} + \frac{c_s^2}{2}\,\frac{\delta\rho^2}{\rho_0} + \frac{\delta B^2}{8\pi}\right) e^{-2i\omega_0 t}\right].$$

Given the phase relations between the perturbed quantities, it follows from (38) that

$$\langle\varepsilon(t)\rangle = 2e^{-2\nu t}\left[\left(\rho_0\frac{|\delta v_r|^2}{2}+\frac{|\delta B_r|^2}{8\pi}\right)\cos^2\omega_0 t\right. \tag{39}$$
$$\left.+\left(\rho_0\frac{|\delta v_\varphi^2+|\delta v_z|^2}{2}+\frac{|\delta B_\varphi^2|+|\delta B_z|^2}{8\pi}\right)\sin^2\omega_0 t\right]$$

or, according to (31),

$$\langle\varepsilon\rangle = 2\left(\frac{\rho_0|\delta v_r|^2}{2}+\frac{|\delta B_r|^2}{8\pi}\right). \tag{40}$$

In view of (8) and (40), formula (34) gives

$$W = 4\pi L\int_0^\infty\left\{\frac{\rho_0|\delta v_r|^2}{2}\left(1+\frac{v_A^2}{v_p^2}\right)\right\}r\,dr. \tag{41}$$

Thus, taking into account (22) and (24), we derive from (36) and (41)

$$F_r = 8L|C_2|^2\frac{\omega_0}{\rho_e(k^2v_{A_e}^2-\omega_0^2)}, \tag{42}$$

$$W_i = \frac{\pi|C_1|^2L}{4}\,\frac{|\mu_i a|^2\omega_0^2}{\rho_i(\omega_0^2-k^2v_{A_i}^2)^2}\left(1+\frac{v_{A_i}^2}{v_p^2}\right), \tag{43}$$

$$W_e = \frac{4|C_2|^2L}{\pi} \tag{44}$$
$$\times\,\frac{\omega_0^2}{\rho_e|\mu_e a|^2(\omega_0^2-k^2v_{A_e}^2)^2}\left(1+\frac{v_{A_e}^2}{v_p^2}\right),$$

where

$$W_i = 2\pi L\int_0^a\langle\varepsilon\rangle r\,dr,\quad W_e = 2\pi L\int_0^\infty\langle\varepsilon\rangle r\,dr.$$

Note that during the integration, we assumed the arguments of the cylinder functions to be much smaller than unity and retained terms of the first order of smallness in their power expansion (22).

Using the joining condition (20) and the dispersion relation for fast kink modes (23), we obtain from (42)–(44)

$$\nu = \frac{F_r}{2(W_i+W_e)} \tag{45}$$
$$=\frac{\pi|v_{A_e}^2-v_{A_i}^2||\mu_e a|^2}{2(\rho_i+\rho_e)v_p^2}\omega_0\left(\frac{1}{\rho_e}+\frac{1}{\rho_i}\right)^{-1},$$

with

$$\frac{W_i}{W_e} = \frac{\rho_i}{\rho_e}\,\frac{v_p^2+v_{A_i}^2}{v_p^2+v_{A_e}^2}. \tag{46}$$

Relation (46) shows that the energy of the fast kink oscillations in the external region can exceed the oscillation energy inside the tube if

$$\frac{\rho_i}{\rho_e} < \frac{v_p^2+v_{A_e}^2}{v_p^2+v_{A_i}^2}.$$

Hence, tenuous magnetic tubes cannot be the source of free oscillations. Note that when calculating the acoustic damping decrement, Ryutova (1988) took into account only the tube internal energy W_i.

When $v_{A_e} > v_{A_i}$ or $v_{A_e} < v_{A_i}$, instead of (45), we derive, respectively,

$$\frac{\nu}{\omega_0} = \frac{\pi}{2}|\mu_e a|^2\frac{\rho_i}{\rho_i+\rho_e}\,\frac{B_e^2}{B_e^2+B_i^2} \tag{47}$$

or

$$\frac{\nu}{\omega_0} = \frac{\pi}{2}|\mu_e a|^2\frac{\rho_e}{\rho_i+\rho_e}\,\frac{B_i^2}{B_e^2+B_i^2}. \tag{48}$$

Thus, we see that when $\rho_i > \rho_e$ and $B_i \approx B_e$, the damping of loop oscillations is stronger if $v_{A_e} > v_{A_i}$.

Let us now compare the results obtained by using the energy method with the estimates that follow from the solution of the dispersion equation (21). Since the argument of the Bessel functions is complex, we have, according to (22),

$$\frac{H_1^{(1)'}(\mu_e a)}{H_1^{(1)}(\mu_e a)} = -\frac{1}{\mu_e a} \tag{49}$$
$$-\frac{\mu_e a}{2}\left(\ln\left(\frac{|\mu_e a|}{2}\right)\pm 2\pi\right).$$

Disregarding the term with a logarithmic dependence in Eq. (49) and substituting it in the dispersion equation (21) yields

$$\rho_e(k^2v_{A_e}^2-\omega^2)+\rho_i(k^2v_{A_i}^2-\omega^2)(1\pm i\pi\mu_e^2a^2)=0. \tag{50}$$

Setting the frequency $\omega=\omega_0-i\nu$ in (50) and making the real and imaginary parts equal between themselves, we obtain

$$\rho_e(k^2v_{A_e}^2-\omega_0^2)+\rho_i(k^2v_{A_i}^2-\omega_0^2) \tag{51}$$
$$=\pm 2\pi\nu\omega_0\rho_i|\mu_e a|^2,$$

$$\rho_i(k^2v_{A_i}^2-\omega_0^2) = \mp\frac{2\nu\omega_0(\rho_i+\rho_e)}{\pi|\mu_e a|^2}. \tag{52}$$

Since the right-hand part of Eq. (51) is negligible, the previously derived dispersion relation for kink modes (23) follows from it. In turn, Eq. (52) gives

$$\nu = \pm\frac{\pi(v_{A_e}^2-v_{A_i}^2)|\mu_e a|^2}{2(\rho_i+\rho_e)v_p^2}\omega_0\left(\frac{1}{\rho_e}+\frac{1}{\rho_i}\right)^{-1}. \tag{53}$$

We see that ν given by Eqs. (45) and (53) are equal in absolute value. It should be noted that Spruit (1982) used the dispersion equation to calculate the acoustic damping decrement for fast kink oscillations. It is easy to verify that Eq. (53) and the relation derived by Spruit (1982) differ by the coefficient 2π. The cause of this discrepancy cannot be elucidated, because Spruit (1982) gave no intermediate transformations.

3. THE GENERATION AND PROPAGATION OF RUNNING WAVES IN THE SOLAR ATMOSPHERE

Before analyzing the strong damping of coronal-loop oscillations in active regions detected with the TRACE space telescope, we note the following. According to observations, the plasma temperature and density inside oscillating loops are $\sim 10^6$ K and 10^9 cm^{-3}, respectively, whereas the magnetic-field strength lies within the range 5–60 G (Aschwanden *et al.* 1999). Although the question of the magnetic-field configuration is still an open question, it is well known that the radii of curvature of the loops are comparatively large, while their thicknesses change by a mere 10–20% (Schrijver *et al.* 1999). Since the transverse displacements of oscillating loops are an order of magnitude larger in amplitude than their lengths, we have reason to model these magnetic structures as thin tubes, restricting ourselves to the linear approximation when describing the wave processes (see also Aschwanden *et al.* 1999, Nakariakov *et al.* 1999).

In the preceding section, we derived relations to determine the acoustic damping decrement for oscillations of thin magnetic tubes ν in the case where they radiate radial MHD waves. According to relation (47), the decrement for $B_i \approx B_e$ and $\rho_i \gg \rho_e$ is $\nu \approx (\pi/4)|\mu_e a|^2\omega_0$, and, since $|\mu_e a| \ll 1$, the Q factor of the oscillations is $Q = \omega_0/(2\nu) \approx (2/\pi)|\mu_e a|^{-2} \gg 1$. Moreover, if $c_{s_e}^2/v_{A_e}^2 \ll 1$ in the external region, we find from the equilibrium condition (13) and from Eqs. (16) and (23) that

$$v_{A_e}^2 = \frac{\rho_i}{\rho_e}\left(\frac{3}{5}c_{s_i}^2 + v_{A_i}^2\right), \quad \mu_e^2 = \frac{v_{A_e}^2 - v_{A_e}^2}{v_{A_e}^2}k^2. \quad (54)$$

As we see from (54), $\mu_e^2 < 0$ for $\rho_i > \rho_e$, i.e., an oscillating loop cannot generate radially propagating MHD waves when the plasma $\beta = c_{s_e}^2/v_{A_e}^2 \ll 1$ in the external region. Nevertheless, the acoustic mechanism is capable of producing a strong damping of fast kink coronal-loop oscillations if the following factors are taken into account.

The appearance of coronal loops is currently believed to be associated with the emergence of a nonuniform (filamentary) magnetic flux on the solar surface (Parker 2000). It may therefore be assumed that the background coronal magnetic field differs in configuration from the loop itself, remaining, for example, open. As a result, the conditions for the generation of standing waves in the external region are violated, and the fast kink oscillations lead to the generation in the surroundings of running waves propagating upward along magnetic field lines. Let us estimate the acoustic damping decrement in the case under consideration.

According to (30), we represent the wave energy flux along the external magnetic field as

$$\langle q_z(t)\rangle = \left(|\delta p \delta v_r| - \frac{|\delta B_r \delta v_r|}{8\pi}B_z - \frac{|\delta B_\varphi \delta v_\varphi|}{8\pi}B_z\right)e^{-2\nu t}. \quad (55)$$

Assuming that $c_{s_e}^2/v_{A_e}^2 \ll 1$ and integrating (55) over the surface perpendicular to the tube axis and bounded below by radius a, in view of (8), (9), and (31), we have

$$F_z = 2\pi\int_a^\infty \langle q_z\rangle r\, dr \quad (56)$$
$$= 2\pi\int_a^\infty \left\{\rho_0\frac{v_A^2}{2v_p}(\delta v_r^2 + \delta v_\varphi^2)\right\} r\, dr.$$

It then follows from (15), (19), (37), and (56) that

$$F_z = \pi|C_2|^2\frac{v_{A_e}^2}{v_p}\,\frac{\omega_0^2}{\rho_e|\mu_e a|^2(\omega_0^2 - k^2 v_{A_e}^2)^2}. \quad (57)$$

As previously, we obtain for the acoustic damping decrement using (19), (20), (22), (41), and (57)

$$\nu = \frac{F_z}{W_i + W_e} = \frac{v_p}{2L}\,\frac{B_e^2}{B_i^2 + B_e^2}. \quad (58)$$

When standing waves are excited, the longitudinal component of the wave number is $k = N\pi/L$, and Eq. (58) reduces to

$$\frac{\nu}{\omega_0} = \frac{1}{2\pi N}\,\frac{B_e^2}{B_i^2 + B_e^2}. \quad (59)$$

For $B_e \approx B_i$ and $N = 1$, the Q factor of the oscillations, according to (59), is $Q \approx 2\pi$, i.e., the standing-wave amplitude decreases by a factor of e in time $\tau = Q/(\pi T) \approx 2T$. Thus, because of the excitation of running waves propagating along magnetic field lines by an oscillating coronal loop, the acoustic damping may turn out to be so strong that the loop will make only a few oscillations.

To conclude this section, let us consider in more detail the hypothesis of the photospheric nature of the observed transverse loop displacements proposed by by Schrijver and Brown (2000). Let an MHD wave be excited through flare energy release in the coronal part of the magnetic tube. It can reach the photosphere without being reflected if its length is (Pikelner 1966)

$$\lambda \ll 4\pi H, \quad (60)$$

where H is the scale height. Taking $H = 300$ km in the latter inequality, we obtain $\lambda \ll 3800$ km. This means that only small-scale MHD waves can penetrate into the lower solar atmosphere. Since the maximum standing-wave length in coronal loops is $\lambda = 2L = 3\times10^4$–$3\times10^5$ km, their internal region,

in view of (60), is an ideal resonator for waves with $N_t = N - 1 \ll L/(2\pi H) =$10–100 nodes.

Let us calculate the ratio of the perturbation amplitudes at various levels of the solar atmosphere when small-scale ($\lambda \ll 3800$ km) MHD waves propagate into the photosphere. We write the wave energy flux along the magnetic tube as

$$F = \frac{\rho \delta v^2}{2} v_A S_T, \tag{61}$$

where S_T is the tube cross section. Assuming that $F =$ const and $BS_T =$ const, we obtain, according to (61),

$$\frac{\delta v_p}{\delta v_c} = \left(\frac{n_p}{n_c}\right)^{1/4}, \tag{62}$$

where δv_p and δv_c are the velocity perturbation amplitudes in the photosphere and the corona, respectively; and n_p and n_c are the corresponding densities. Taking $n_p \approx 10^{17}$ cm^{-3} and $n_c \approx 10^9$ cm^{-3}, we find from (62) that $\delta v_p/\delta v_c \approx 10^{-2}$. Since the perturbation amplitude in the corona in the linear approximation is $\delta\xi_c \ll \lambda$, we derive for $\delta\xi_c \approx 100$ km at the photospheric level $\delta\xi_p = \delta\xi_c \delta v_p/\delta v_c \approx 1$ km, which is more than two orders of magnitude smaller than the values assumed by Schrijver and Brown (2000). Consequently, the large-scale MHD waves attributable to flare energy release are completely reflected from the lower solar atmosphere, whereas small-scale MHD waves cannot cause significant changes in the positions of the loop footpoints in the photosphere. As for the other possible perturbation sources (shock waves, accelerated particles, thermal fronts), their contribution to the feet perturbation due to substantial energy losses through the propagation from the corona to the photosphere must be even smaller than that for Alfvèn waves.

DISCUSSION AND CONCLUSIONS

We have considered the acoustic damping mechanism for fast kink oscillations of thin magnetic tubes. Two approaches were used to calculate the damping decrement: the first is based on the energy conservation law, and the second is based on an analysis of the dispersion relation for magnetic-tube eigenmodes. The proposed energy method for calculating the acoustic damping decrement allowed us to obviate the main difficulty that arises when using the transfer equation for a wave packet: the need to determine the transverse wave group velocity from the dispersion equation. Each of the two methods has its own shortcomings. At the same time, detailed analytic calculations show that under appropriate assumptions, the methods are in good agreement.

As follows from our results, the radiation of radial MHD waves does not lead to a significant damping of kink magnetic-tube oscillations. This is because an oscillating magnetic tube produces perturbations in the external region that are oscillatory in nature near the boundary, with their amplitude in the radial direction rapidly decreasing. Only relatively far from the boundary ($r \gg a$) do the displacements transform into cylindrical waves, which can effectively transfer the tube oscillation energy to the surroundings.

We associate the observed strong damping of fast kink oscillations with an open magnetic-field configuration in the quiet corona, which leads to the generation of running waves in the external region propagating along magnetic field lines. However, some of the waves can be reflected to become standing waves. Clearly, this weakens the energy outflow from the oscillating loop and reduces the damping. It should also be noted that if the number of nodes in the standing wave is $N_t \gg 1$, then the acoustic damping of fast kink oscillations is negligible. This result suggests that only small-scale kink waves can effectively heat the coronal loops. However, such perturbations are capable of easily penetrating the dense photospheric layers where the dissipative processes increase appreciably in importance.

Fast kink oscillations primarily result in a modulation of the loop magnetic-field direction. Therefore, one might expect them to be easiest to detect using microwave observations, because the radio-emission mechanisms are most sensitive to changes in the angle between the line of sight and the magnetic-field direction. However, the acceleration and propagation of charged particles are determined by the solar coronal magnetic field, and much of the solar-flare energy, which subsequently goes into plasma heating and emission (Miller *et al.* 1997), is accounted for by the accelerated particles. Hence, the modulation of the emission produced by fast kink oscillations can also appear in other wavelength ranges.

ACKNOWLEDGMENTS

We are grateful to A.V. Stepanov and to the referee for a discussion and helpful remarks. This study was supported by the Russian Foundation for Basic Research (project no. 00-02-16356) and the State Science and Technology Program "Astronomy."

REFERENCES

1. K. Appert, R. Gruber, and J. Vaclavik, Phys. Fluids **17**, 1471 (1974).
2. M. J. Aschwanden, L. Fletcher, C. J. Schrijver, *et al.*, Astrophys. J. **520**, 880 (1999).

3. S. I. Braginskiĭ, in *Reviews of Plasma Physics,* Ed. by M. A. Leontovich (Gosatomizdat, Moscow, 1963; Consultants Bureau, New York, 1963), Vol. 1.
4. K. Hain and R. Lüst, Z. Naturforsh. A **13**, 936 (1958).
5. B. B. Kadomtsev, *Collective Phenomena in a Plasma* (Nauka, Moscow, 1976).
6. J. Kleczek and M. Kuperus, Sol. Phys. **6**, 72 (1969).
7. Yu. G. Kopylova and Yu. T. Tsap, Izv. Glavn. Astron. Obs. Akad. Nauk SSSR, No. 215, 301 (2000).
8. A. G. Kosovichev and V. V. Zharkova, Nature **393**, 317 (1998).
9. J. A. Miller, P. J. Cargill, A. G. Emsile, *et al.*, J. Geophys. Res. **102**, 14631 (1997).
10. V. M. Nakariakov, L. Ofman, E. E. DeLuca, *et al.*, Science **285**, 862 (1999).
11. E. N. Parker, Phys. Today **53**, 26 (2000).
12. S. B. Pikelner, *Fundamentals of Cosmic Electrodynamics* (NASA, Washington, DC, 1964; Nauka, Moscow, 1966).
13. B. Roberts, in *Advances in Solar System Magnetohydrodynamics,* Ed. by E. R. Priest and A. W. Wood (Cambridge Univ. Press, Cambridge, 1991; Mir, Moscow, 1995).
14. B. Roberts, P. M. Edwin, and A. O. Benz, Astron. Astrophys. **279**, 857 (1984).
15. M. R. Ryutova, Zh. Éksp. Teor. Fiz. **94** (8), 138 (1988) [Sov. Phys. JETP **67**, 1594 (1988)].
16. H. C. Spruit, Sol. Phys. **75**, 3 (1982).
17. B. A. Trubnikov, *Theory of Plasma* (Énergoatomizdat, Moscow, 1996).
18. C. J. Schrijver and D. S. Brown, Astrophys. J. Lett. **537**, L69 (2000).
19. C. J. Schrijver *et al.*, Astrophys. J. Lett. **520**, L888 (1999).
20. C. J. Schrijver, A. M. Title, T. E. Berger, *et al.*, Sol. Phys. **187**, 261 (1999).
21. Y. T. Tsap, Sol. Phys. **194**, 131 (2000).
22. G. N. Watson, *Treatise on the Theory of Bessel Functions* (Cambridge University Press, Cambridge, 1945; Inostrannaya Literatura, Moscow, 1949).
23. V. V. Zaĭtsev and A. V. Stepanov, Issled. Geomagn., Aéron. Fiz. Solntsa **37**, 3 (1975).

Translated by V. Astakhov

Astronomy Letters, Vol. 27, No. 11, 2001, pp. 745–753. Translated from Pis'ma v Astronomicheskiĭ Zhurnal, Vol. 27, No. 11, 2001, pp. 867–876.

A Study of the Regularities in Solar Magnetic Activity by Singular Spectral Analysis

A. Yu. Loskutov[1,*], I. A. Istomin[1], O. L. Kotlyarov[1], and K. M. Kuzanyan[2]

[1]*Moscow State University, Vorob'evy gory, Moscow, 119899 Russia*
[2]*Institute of Terrestrial Magnetism, Ionosphere, and Radiowave Propagation, Russian Academy of Sciences, Troitsk, 142092 Russia*

Received March 12, 2001

Abstract—The method of singular spectral analysis (SSA) is described and used to analyze the series of Wolf numbers that characterizes solar activity from 1748 until 1996. Since this method is relatively new, we detail its algorithm as applied to the data under study. We examine the advantages and disadvantages of the SSA method and the conditions for its applicability to an analysis of the solar-activity data. Certain regularities have been found in the dynamics of this series. Both short and long (80–100-year) periodicities have been revealed in the sunspot dynamics. We predict the solar activity until 2014.

Key words: *Sun, nonlinear dynamics, solar cyclicity*

INTRODUCTION

It has long been noticed that the solar activity is related to the number of sunspots visible on the solar disk. The sunspot number varies greatly within an 11-year interval called the solar cycle. The accompanying change in the solar magnetic-field structure indirectly affects the Earth's climate and has a probable relationship to natural disasters. Since the solar magnetic activity is significant, its analysis is of great practical interest.

Various tracers are used to describe the dynamics of solar magnetic activity, of which the Wolf number (relative sunspot number) is most convenient. The dynamics of this parameter is quasi-periodic in pattern. However, accurate predictions are difficult to make, because simple models of the process disregard many important factors of the solar magnetic activity. During the last 250 years, the duration of the solar cycle has varied by no more than 20%, while its amplitude has varied by more than a factor of 10. Even sophisticated models do not give a detailed description of these variations.

Recently, many methods for predicting and reconstructing the dynamics of the series of Wolf numbers have been proposed (see Schatten 1997, Nagovitsyn 1997, Wilson *et al.* 1998, Hoyt and Schatten 1998, Hathaway *et al.* 1999, and references therein). Since they all have various drawbacks, predicting the sunspot dynamics from the available observational data alone, without constructing a model of the phenomenon, has become very promising. Here, an analysis of time series by the methods of nonlinear dynamics (see Afraĭmovich and Reĭman 1989, Casdagli 1989, Loskutov and Mikhaĭlov 1990, Ruelle 1990, Sauer *et al.* 1991, Malinetskiĭ and Potapov 2000, and references therein) can give a significant contribution. In this case, however, there are also many difficulties that stem from the fact that the series of Wolf numbers is apparently not a strictly deterministic system and has no well-defined dimensionality (Lowrence *et al.* 1993, 1995); besides; it is relatively short.

As a new method for analyzing and predicting the dynamics of the time series formed by Wolf numbers, we propose to use a singular spectral analysis (SSA). As we show below, it provides highly reliable predictions of the amplitude of the 11-year solar cycle and is suitable for revealing longer cycles. It can also be used to study regularities in series of other astrophysical indices. Since this method is relatively new and covered little in the literature, we detail its algorithm as applied to the formulated problem.

SINGULAR SPECTRAL ANALYSIS

The SSA method (Broomhead and King 1986a, 1986b; Broomhead and Jones 1989; Vautard *et al.*

*E-mail: loskutov@moldyn.phys.msu.su

1992; Danilov and Zhiglyavskiĭ 1997) used here allows the following:

—to distinguish the components of a time series obtained from a sequence of values of a quantity taken at equal time intervals;

—to find periodicities in a series that are not known in advance;

—to smooth initial data on the basis of selected components;

—to best separate a component with a period known in advance; and

—to predict the subsequent behavior of the observed dependence.

The SSA method is efficient enough to successfully compete with numerous smoothing techniques (Danilov and Zhiglyavskiĭ 1997, Percival and Walden 1993, Theiler *et al.* 1992, Kaplan and Glass 1992). Moreover, SSA-based predictions in many cases yield more reliable results than do other known algorithms (see Casdagli 1989, Danilov and Zhiglyavskiĭ 1997, Deppish *et al.* 1991, Murray 1993, Cao *et al.* 1995, Keppenne and Ghil 1995, and references therein).

The SSA method is based on the passage from an analysis of the initial linear series $(x_i)_{i=1}^N$ to an analysis of a multidimensional series composed of its sets, which, apart from x_i itself, contain a certain number of x_{i-j}, $j = 1, \ldots, \tau$, at preceding times.

Let us briefly describe the main stages of SSA application to the specific series $(x_i)_{i=1}^N$.

(1) At the first stage, the one-dimensional series is transformed to a multidimensional one. For this transformation, it is necessary to take some number of delays $\tau \le [(N+1)/2]$, where $[\cdot]$ denotes the integer part of a number, and to represent the initial τ values of the sequence as the first column of some matrix X. The sequence values from x_2 to $x_{\tau+1}$ are chosen for the second column of this matrix, and so on. The last τ elements of the sequence $x_n, \ldots, x_N$ correspond to the last column with number $n = N - \tau + 1$. Thus, the transformed series takes a matrix form

$$X = \begin{pmatrix} x_1 & x_2 & x_3 & \ldots & x_\tau & \ldots & x_n \\ x_2 & x_3 & x_4 & \ldots & x_{\tau+1} & \ldots & x_{n+1} \\ x_3 & x_4 & x_5 & \ldots & x_{\tau+2} & \ldots & x_{n+2} \\ \vdots & \vdots & \vdots & \ddots & \vdots & \ddots & \vdots \\ x_\tau & x_{\tau+1} & x_{\tau+2} & \ldots & x_{2\tau-1} & \ldots & x_N \end{pmatrix}.$$

The constructed matrix X is rectangular, but in the limiting case, i.e., for $\tau = (N+1)/2$ and odd N, it degenerates to a square matrix.

(2) Next, the corresponding covariance matrix is constructed for matrix X

$$C = \frac{1}{n} X X^T.$$

(3) Now, the eigenvalues and eigenvectors of matrix C must be determined. This requires its decomposition into eigenvectors $C = V \Lambda V^{\mathrm{T}}$, where we introduced

$$\Lambda = \begin{pmatrix} \lambda_1 & 0 & \ldots & 0 \\ 0 & \lambda_2 & \ldots & 0 \\ \vdots & \vdots & \ddots & \vdots \\ 0 & 0 & \ldots & \lambda_\tau, \end{pmatrix}$$

the diagonal matrix of eigenvalues, and

$$V = \left(V^1, V^2, \ldots, V^\tau\right) = \begin{pmatrix} v_1^1 & v_1^2 & \ldots & v_1^\tau \\ v_2^1 & v_2^2 & \ldots & v_2^\tau \\ \vdots & \vdots & \ddots & \vdots \\ v_\tau^1 & v_\tau^2 & \ldots & v_\tau^\tau, \end{pmatrix}$$

the orthogonal matrix of eigenvectors for matrix C. Clearly, $\Lambda = V^{\mathrm{T}} C V$, $\det C = \prod_{i=1}^\tau \lambda_i$, and $\sum_{i=1}^\tau \lambda_i = \tau$ (the latter equality holds only for the prenormalized rows of matrix X).

(4) The matrix of eigenvectors V is commonly represented as a transition matrix to the principal components $Y = V^{\mathrm{T}} X = (Y_1, Y_2, \ldots, Y_\tau)$ of the initial series, where Y_i, $i = 1, 2, \ldots, \tau$, are the rows of length n. In this case, the eigenvalues $\lambda_1, \lambda_2, \ldots, \lambda_\tau$ may be considered as a contribution of the principal components $Y_1, Y_2, \ldots, Y_\tau$ to the total information content of the time series $(x_i)_{i=1}^N$. The initial matrix can then be completely reconstructed from the derived principal components

$$X = \left(V^1, V^2, \ldots, V^\tau\right) \begin{pmatrix} Y_1 \\ Y_2 \\ \vdots \\ Y_\tau \end{pmatrix} = \sum_{i=1}^\tau V^i Y_i;$$

in turn, the time series $(x_i)_{i=1}^N$ can be reconstructed from it. Note that, in general, not all of the principal components $Y_1, Y_2, \ldots, Y_\tau$ but only some of them that are significant in terms of the information content are used to reconstruct the time series (see Broomhead and King 1986a, 1986b; Broomhead and Jones 1989; Vautard *et al.* 1992). More specifically, each row vector Y_i, $i = 1, 2, \ldots, \tau$, may be considered as the result of projecting a τ-dimensional set of points, each of which is specified by the τ-coordinate

column vector of matrix X, onto the direction that corresponds to eigenvector V^i. Thus, the series turns out to be represented as a set of τ components Y_i; the weight of component Y_i in the initial sequence $(x_i)_{i=1}^N$ can be specified via the corresponding eigenvalue λ_i, which, in turn, corresponds to eigenvector V^i.

The transformations $Y_i = (V^i)^{\mathrm{T}} X$, $i = 1, 2, \ldots, \tau$, $Y_i[l] = \sum_{q=1}^{r} v_q^i x_q^l$, $l = 1, 2, \ldots, n$, are linear filters. In the case under consideration, the eigenvectors V^i are the transition functions of these linear filters, while the filters themselves are tuned to the components of the multidimensional series X and, consequently, to the components of the initial series $(x_i)_{i=1}^N$.

Each ith eigenvector includes τ components, i.e., $V^i = \left(v_1^i, v_2^i, \ldots, v_\tau^i\right)^{\mathrm{T}}$. Let us construct a dependence of components v_k^i, $k = 1, 2, \ldots, \tau$ on their number: $v^i = v^i(k)$. Using the orthogonality of eigenvectors, the subsequent analysis of sequence $(x_i)_{i=1}^N$ can then be performed by studying the diagrams constructed by analogy with Lissajous figures. More specifically, the components v_k^i and v_k^j are plotted in pairs along the axes. If the constructed diagrams are nearly circular, then the functions $v^i = v^i(k)$ and $v^j = v^j(k)$ will be similar to periodic functions with close amplitudes and with a phase shift of about a quarter of the period.

Thus, a quantity that has the meaning of a period can be calculated for some pairs of eigenvectors V^i and V^j. Consequently, a graphical analysis gives an idea of the frequencies of the components that form the initial time series $(x_i)_{i=1}^N$.

For a given τ, the number of all possible pairs of the principal components is $\sim\tau^2$. Clearly, all these pairs are very difficult to analyze even at small τ. Moreover, since only a few plots are spiral in shape at large τ, the range of search should be narrowed before beginning a graphical analysis. This can be easily done if we arrange V^i and Y_i in order of decreasing eigenvalues and if we consider only those pairs of eigenvectors that have close values of λ_i. In the $\lambda = \lambda(i)$ diagram, these pairs at sufficiently large λ appear as steps against the background of a general decrease in $\lambda(i)$ with increasing i. By examining these steps, we can determine the minimum value of $\lambda_{\min}(i)$ below which the function $\lambda = \lambda(i)$ relaxes to an exponential tail.

(5) Suppose that only the first r of the τ components were retained for the subsequent analysis. The first r eigenvectors V^i are then used to reconstruct the initial matrix X. In that case,

$$\tilde{X} = \left(V^1, V^2, \ldots, V^r\right) \begin{pmatrix} Y_1 \\ Y_2 \\ \vdots \\ Y_r \end{pmatrix} = \sum_{i=1}^{r} V^i Y_i,$$

where $\tilde{X}$ is the reconstructed matrix with n columns and τ rows. The initial time series reconstructed from this matrix is now defined as

$$\tilde{x}_s = \begin{cases} \dfrac{1}{s}\displaystyle\sum_{i=1}^{s} \tilde{x}_{i,s-i+1}, & 1 \le s \le \tau \\ \dfrac{1}{\tau}\displaystyle\sum_{i=1}^{\tau} \tilde{x}_{i,s-i+1}, & \tau \le s \le n \\ \dfrac{1}{N-s+1}\displaystyle\sum_{i=1}^{N-s+1} \tilde{x}_{i+s-n,n-i+1}, & n \le s \le N. \end{cases}$$

This method of obtaining the sequence $(\tilde{x}_i)_{i=1}^N$ is called a SSA smoothing of the initial time series $(x_i)_{i=1}^N$ over the first r components of τ.

(6) At the next stage of SSA application, one may consider a prediction of the initial time sequence (see Keppenne and Ghil 1995, Danilov 1997, Ghil 1997, and references therein), i.e., a construction of series $(x_i)_{i=1}^{N+p}$, which is an extension of the known data $(x_i)_{i=1}^N$. In turn, the prediction for p points ahead reduces to applying the operation of prediction for one point p times.

The basic idea of finding x_{N+1} is as follows. Let there be a set of $x_1, x_2, \ldots, x_N$. We now construct a sample in the form of matrix X. The previously selected eigenvectors $V^1, V^2, \ldots, V^r$ of matrix C may be taken as a basis of the surface containing this sample.

Let us write the parametric equation for this surface as $S(P) = \sum_{i=1}^{r} p_i V^i$, where the set of r parameters p_i corresponds to each value of vector $S(P)$, which is a column of height τ. In that case, the kth $(k = 1, 2, \ldots, n)$ column of the initial matrix X has its own set of parameters $P^k = (p_1^k, p_2^k, \ldots, p_r^k)$ and, consequently,

$$X^1 = S(P^1),\ X^2 = S(P^2), \ldots,\ X^n = S(P^n).$$

To predict x_{N+1}, it is necessary to construct the $(n+1)$th column X^{n+1} of matrix X, which, in turn, corresponds to some value of parameters $P^{n+1} = (p_1^{n+1}, p_2^{n+1}, \ldots, p_r^{n+1})$. This set of parameters can be found from the relation $S(P) = \sum_{i=1}^{r} p_i V^i$ based on the

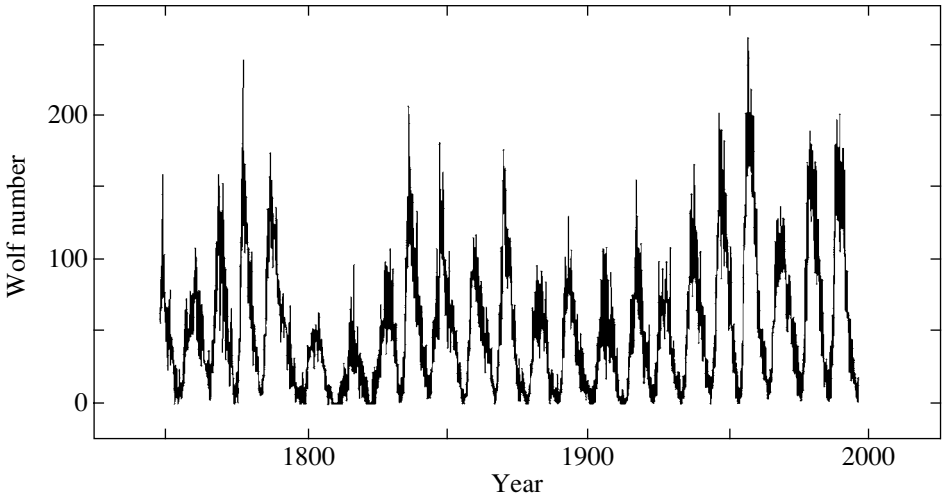

Fig. 1. Monthly mean Wolf numbers.

$(x_i)_{i=1}^N$ data alone. The predicted column is written as $X^{N+1} = S\left(P^{n+1}\right)$.

Let us introduce the following notation:

$$V_* = \begin{pmatrix} v_1^1 & v_1^2 & \dots & v_1^r \\ v_2^1 & v_2^2 & \dots & v_2^r \\ \vdots & \vdots & \ddots & \vdots \\ v_{\tau-1}^1 & v_{\tau-1}^2 & \dots & v_{\tau-1}^r \end{pmatrix},$$

$$\tilde{p} = \begin{pmatrix} \tilde{p}_1^{n+1} \\ \tilde{p}_2^{n+1} \\ \vdots \\ \tilde{P}_r^{n+1} \end{pmatrix}, \quad Q = \begin{pmatrix} x_{N-\tau+2} \\ x_{N-\tau+3} \\ \vdots \\ x_N \end{pmatrix},$$

$$V_\tau = \left(v_\tau^1, v_\tau^2, \dots, v_\tau^r\right).$$

The parameters $(p_1^{n+1}, p_2^{n+1}, \dots, p_r^{n+1})$ can be determined from the system of equations $V_*\tilde{P} = Q$ for $\tilde{P}$. Thus, the final expression for the predicted value reads

$$x_{N+1} = \frac{V_\tau V_*^{\mathrm{T}} Q}{1 - V_\tau V_\tau^{\mathrm{T}}}.$$

In the simplest case, to predict the next values requires only appropriately changing the matrix Q and again multiplying it by $V_\tau V_*^{\mathrm{T}}/(1 - V_\tau V_\tau^{\mathrm{T}})$. Additionally, however, the entire SSA algorithm can be partially or completely repeated for each next point. In this case, the matrices V_τ and V_* also change.

(7) At the final stage of SSA application, one chooses the main parameter, the number of delays τ used to construct the multidimensional sample X. As with the selection of principal components, the choice of τ significantly depends on the problem being studied.

Let the problem consist in smoothing a series by the SSA method, i.e., in reconstructing the series using known periodicities. In that case, as was already noted above, separating the principal component is filtering the series with the filter transition function in the form of an eigenvector of this principal component. The larger τ, the larger the number of parallel filters, the narrower the passband of each of them, and the better the series smoothing.

If unknown (hidden) periodicities must be determined in the observed sequence, then we should first take the largest possible value of τ. After rejecting nearly zero eigenvalues, the delay must then be reduced.

Suppose that it is necessary to separate one known periodicity. In this case, we should choose τ to be equal to the sought-for period.

Finally, let the problem consist in extending the series under study by a specified value (i.e., in predicting the evolution of the observed process). We should then take the maximum admissible value of τ and then choose r.

USING THE SSA METHOD TO ANALYZE SOLAR MAGNETIC ACTIVITY

Here, we apply the SSA method to observational data on solar activity. Wolf proposed to use the sunspot number as a measure of solar activity in 1848. To this end, he considered the sum of the total number of spots seen on the solar disk and ten times the number of regions in which these spots were located.

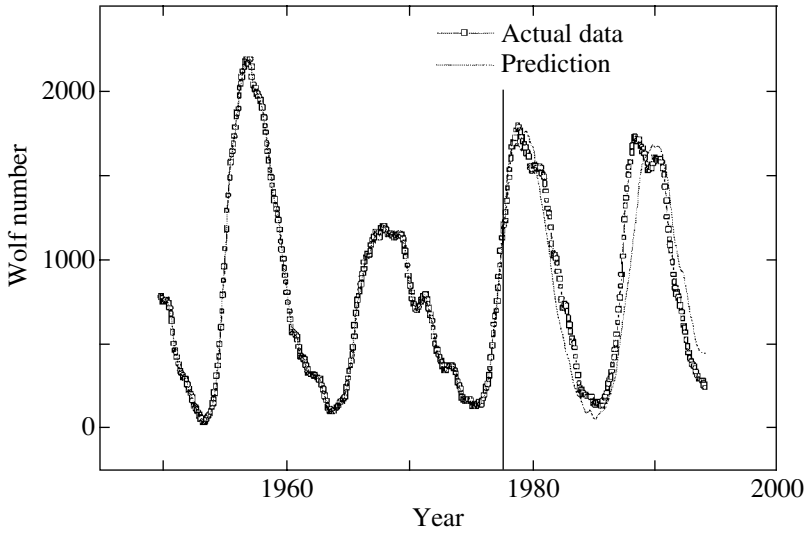

Fig. 2. Prediction of the solar activity for 216 points (18 years ahead) from monthly mean Wolf numbers. The vertical line corresponds to the boundary of the rejected values. We used 500 and 150 components for the decomposition and reconstruction, respectively. The computations were performed in three stages. After predicting another 72 points, the components of the series were recomputed.

The latter summand is intended to reconcile the measurements made under different conditions. By comparing the previous observations obtained from various sources, Wolf reconstructed the solar-activity data until 1818 with several small gaps and with acceptable accuracy. Later, the monthly means were reconstructed until 1749 (this series was used here) and the yearly means until 1700. In the latter case, however, the error in the data can be several tens of percent.

The sequence chosen for our analysis spans a wide period, from January 1749 until December 1996, without gaps and with good time resolution (see Fig. 1, where the time at intervals of one month and the corresponding Wolf number are plotted along the horizontal and vertical axes, respectively). Thus, there is a total of 2976 values.

At the first stage of SSA application, the maximum admissible value of τ should be taken. For our studies, we chose $\tau = 500$, which allowed the periodicities up to a period of 42 years to be covered. Using larger τ significantly complicated numerical calculation. Moreover, a slight increase in τ (to 600) did not cause any significant changes in the results of the first principal-component decomposition but considerably reduced the computer resources.

Because of the large τ, the sequence of the roots of eigenvalues for the matrix of the second moments arranged in decreasing order rapidly relaxed to an exponential tail. In combination with a large number of initial points, this leads to the fact that even the first principal component represents only a slight smoothing of the initial series, and it is almost completely reconstructed from the first four or five components (the sum of the first five eigenvalues exceeds 99% of their total). Moreover, the form of the first principal component changes little at small τ, for example, at $\tau = 5$, which is attributable to the SSA stability for this parameter. Therefore, using a large τ is justifiable only from the viewpoint of prediction.

To test the prediction by the SSA method, let us truncate the sequence of *monthly* mean Wolf numbers on the right by 216 points (18 years) and try to reconstruct it according to the following scheme. Determine the optimum parameters of the algorithm

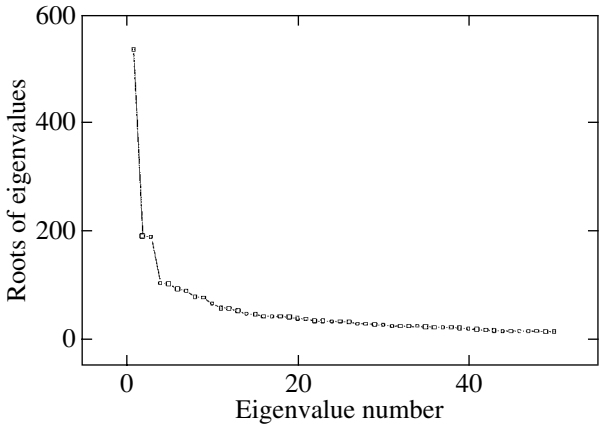

Fig. 3. The first 50 eigenvalues of the matrix of the second moments when decomposing the series of yearly mean Wolf numbers into 123 components. The eigenvalues are arranged in decreasing order.

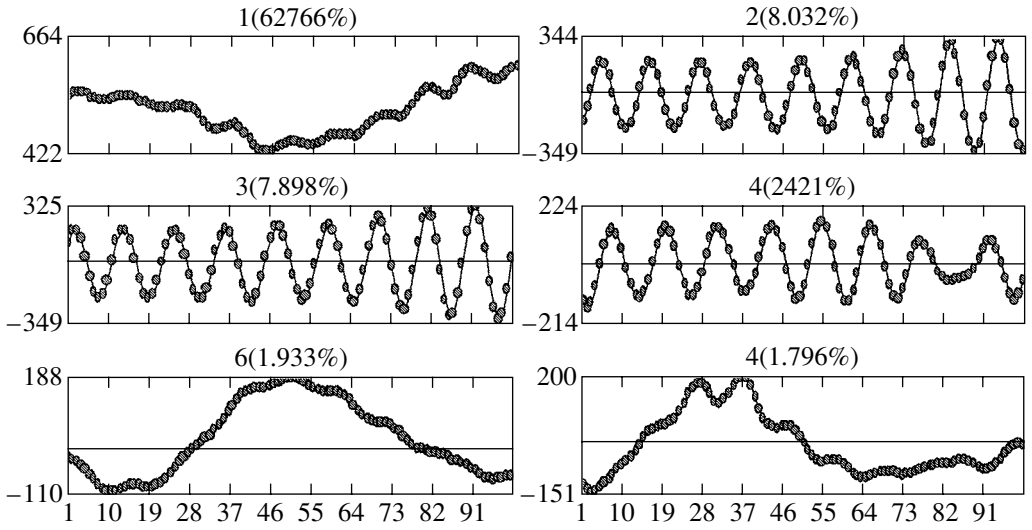

Fig. 4. Some components corresponding to the eigenvalues in Fig. 3. Their percentage contribution to the initial series is given in parentheses.

for reconstructing this series by an additional truncation of the derived series and decompose it into $\tau = 500$ components. In this case, we must choose such a number of the first components for which the agreement between the predicted values and these additionally rejected data is best. Subsequently, we reconstruct the initially truncated part of 216 points by using the parameters found.

It can be established by a direct exhaustive search that the best results are obtained for $r = 150$ (the number of selected components). Let us again take the initial series truncated only by 216 points and use the r chosen for its prediction. The prediction quality can be further increased if we break down the predicted interval into segments and recompute the principal components after predicting each of these segments. Ideally, such a recomputation must be done after predicting each point, but this increases the computational time. Figure 2 shows our prediction for which the components were recomputed three times at intervals of 72 points (which is almost identical to a prediction for 216 points with no breakdown into intervals).

We could try to analyze the components of the series for the presence of particular periods or for the separation of known periods. However, their large number and the associated similarity between the components Y_i of the initial series makes this problem very complex (although quite solvable); i.e., the information contained in the series of monthly mean Wolf numbers is, in a sense, redundant. In addition, since something certain can hardly be said about periodicities of several months, even in the case of their separation, it is easier to take a series with a large time step.

Let us now consider the series of *yearly* mean Wolf numbers. Since the series contains a mere 248 points, the maximum possible delay is $\tau = 123$. Let us choose it as the initial one. The first 50 eigenvalues are shown in Fig. 3. The first value gives the principal component responsible for the trend; the steps form the pairs of components with numbers 2–3, 4–5, 6–7, 8–9, and 11–12; and the dependence relaxes to an exponential tail starting from number 14. The eigenvectors for pairs 2–3, 4–5, 8–9, and 11–12 (Fig. 4) correspond to 11-year periodicities (the spiral two-dimensional plot for components 2 and 3 is shown in the left panel of Fig. 5). However, in addition to this (obvious) 11-year cycle, Gleisberg's presumed 80-year cycle shows up (see the pair of eigenvectors 6 and 7 in Fig. 5). Since the corresponding eigenvalues are not quite equal (the step is skewed; see Fig. 3) and since the phase shift differs from $\pi/2$, the plot for them is not spiral in shape. Nevertheless, the periodicity is traceable, although very small eigenvalues correspond to it.

For a better separation of the 80-year periodicity, we can try to adjust τ for it. For the decomposition of the series with $\tau = 80$ of eigenvectors, vectors 4 and 7 correspond to this period. The eigenvalues that correspond to these vectors are close, but the total contribution of these components at the given τ exceeds 5%. The two-dimensional plot for components 4 and 7 resembles a circumference (Fig. 6). Figure 7 shows the 80-year cycle obtained by reconstructing the series from these two components alone.

Let us now use the SSA method to predict the series of yearly mean Wolf numbers. Let us truncate it on the right by 18 years (i.e., by 18 points) and

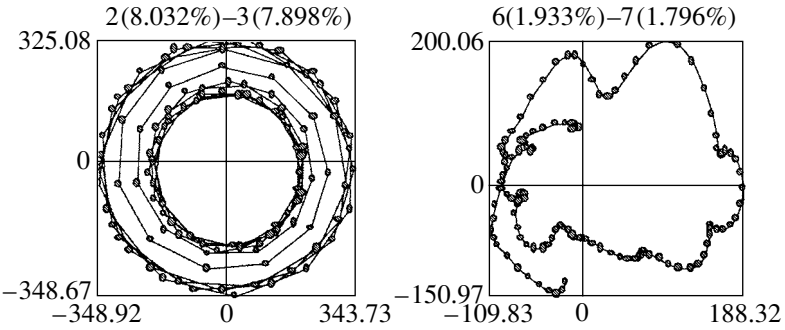

Fig. 5. Diagrams for the vector components 2–3 (left) and 6–7 (right) shown in Fig. 4. The left and right panels correspond to the first and third steps of eigenvalues in Fig. 3, respectively.

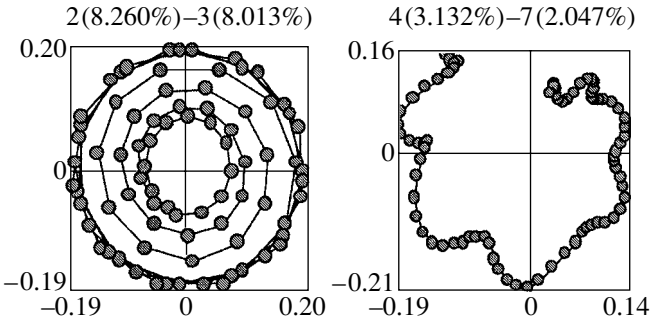

Fig. 6. Plots for the vector components 2–3 (left) и 4–7 (right) at $\tau = 80$.

try to reconstruct them. To this end, we additionally remove an 11-point-long segment and attempt to reconstruct them with the maximum possible accuracy. We perform this procedure in different parts of the series by choosing the best number of eigenvectors for the reconstruction.

For the derived 219-point-long series ($219 = 248 - 18 - 11$, where 248 is the total number of points; see above), the maximum admissible τ is 109. As numerical analyses show, the prediction for 11 points strongly depends on the choice of the components used for the reconstruction. However, the qualitative picture is satisfactory for a wide range of choices. Nevertheless, this value of τ is clearly large for a quantitative prediction. At its lower values, it is much easier to select the required number of components. For example, at $\tau = 33$, the prediction is satisfactory when choosing the first 11 components. Therefore, we use these parameters to reconstruct the 18 distant points. In contrast to the case with monthly mean initial data and $\tau = 500$, it is now possible, for $\tau = 33$, to recompute the eigenvectors every time by taking into account the last predicted point (both at the stage of vector selection for the prediction and during the prediction itself). The prediction corrected at each step is shown in Fig. 8.

In addition, we considered a series of natural logarithms of the initial series. Taking the logarithm is commonly used to analyze time series (e.g., in a correlation analysis) and occasionally yields better results. As with yearly mean Wolf numbers, we use $\tau = 123$. In this case, the general form of the eigenvalues and eigenvectors did not change fundamentally. Thus, it was unnecessary to use the logarithmic series

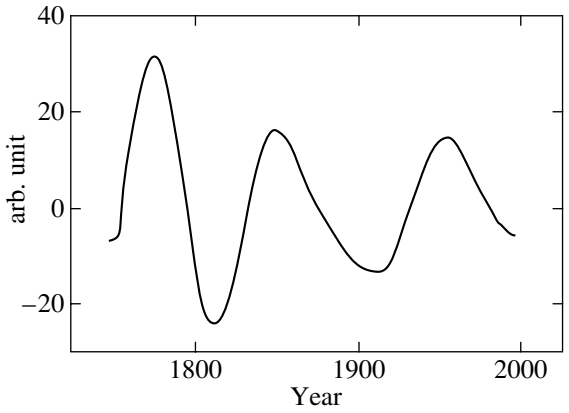

Fig. 7. Reconstruction of components 4 and 7, which correspond to the 80-year solar cycle.

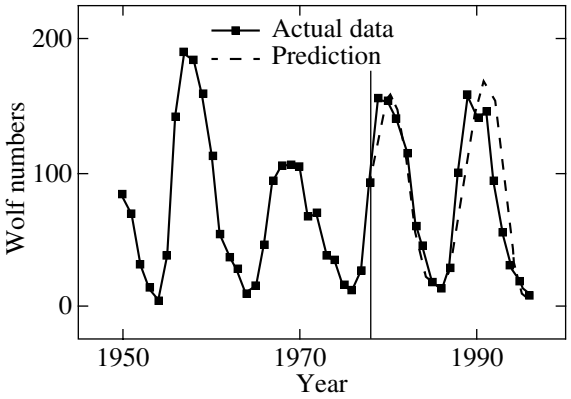

Fig. 8. Reconstruction of yearly mean Wolf numbers corrected at each step. We chose 11 components from 33. The boundary of the rejected 18 points is marked by the vertical straight line.

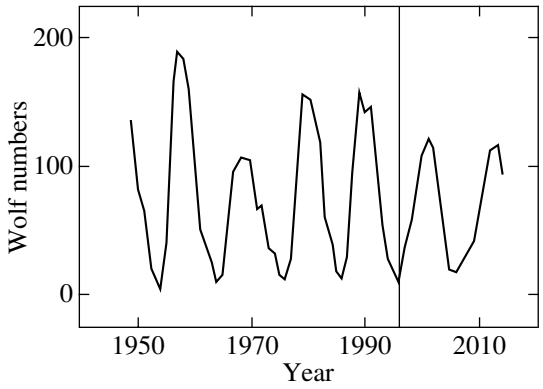

Fig. 9. Prediction of solar activity until 2014.

in this case, because all the main periodicities and the prediction were obtained from the initial series.

At the final stage, we used the SSA method for the actual prediction of solar activity. To this end, we took the series of yearly mean Wolf numbers from 1748 until 1996. Since this yearly mean series ends at a minimum of solar activity, it is of interest to describe its two subsequent maxima. This requires extending the yearly mean sequence by 18 points. We decomposed the series into 33 components and selected the first 11 of them for the prediction.

The prediction until 2014 is shown in Fig. 9. It can be seen from this figure that the maximum of solar cycle 23 occurs in the first half of 2000 and its amplitude is 122. The error in the maximum amplitude is typically of the order of 5–10. This is in excellent agreement with the maximum of Wolf numbers that apparently occurred in the middle of 2000 and that had a smoothed value of 121. As we see from the figure, in the immediate future, the Sun will be relatively quiet (compared to the two previous 11-year periods), while the maximum of solar cycle 24 (presumably in 2011) will be comparatively low. Its estimation yields a Wolf number of 117 (Fig. 9).

For comparison and testing the stability of our result, we also analyzed the series of monthly mean Wolf numbers. However, this analysis introduced no significant additions in the prediction.

If follows from our experience of SSA application that the prediction for more than one and a half 11-year cycles is not informative. At the same time, the Wolf numbers in Fig. 9 (prediction for 18 years ahead) may be considered quite reliable.

CONCLUSIONS

An analysis of time series by the SSA method will probably rank high among the various techniques used to analyze and predict experimental data. Since the initial series is decomposed into components whose analytic form is not fixed in advance, the SSA method allows us to satisfactorily separate components with specified periods from the series and to predict its dynamics. The only criterion for SSA applicability is the information content of the sequence under study. In this case, the constraints on the number of points and characteristic periods are generally much weaker than in other methods (e.g., in a correlation or Fourier analysis).

Here, we have considered the possibility of analyzing the sequence of Wolf numbers that characterize solar activity by the SSA method. Despite the relatively small length of this sequence, the method makes it possible to reveal its components that correspond to the already known solar cycles and allows for a reconstruction using only some of its components. We also found that even short series of observations could be predicted with acceptable accuracy by the SSA method.

Like any other method, SSA has its own drawbacks. First, there is a problem of accurately determining the unknown frequencies in the sequence under study (for a sufficiently long series, this problem can be solved by a Fourier analysis). Second, SSA does not include well-defined component selection rules for a reconstruction, particularly for a prediction. Finally, when applied to an analysis of solar activity, it does not allow the occurrence times of activity peaks (maximum Wolf numbers) to be accurately estimated, although it gives an accurate estimate of their amplitude. As a result, a systematic phase shift is accumulated in the predicted series. Nevertheless, as follows from our analysis, the SSA method described above serves as a good supplement to the available experimental data reduction techniques, particularly for analyzing and predicting fairly short time series to which the series of Wolf numbers belongs (there are only data on 23 11-year cycles).

In the next papers on solar-activity analysis, we will explore the possibility of correcting the cycle phase by using other prediction methods and solar-cycle regularities. It is also possible to improve the governing parameters of this method and/or to use additional information, for example, an empirical relationship between solar-cycle amplitude and phase (Dmitrieva *et al.* 2000). Note also that the decomposition components in the SSA method are generally harmonic functions. However, because of the nonlinearity in the behavior of the solar magnetic-field generation mechanism, significant anharmonicity emerges. As a result, the rise phase of the solar cycle is appreciably shorter than its decline phase. Although the maximum amplitude in the 11-year cycle calculated by SSA is close to its true value, its occurrence time is determined inaccurately. Hence, significant errors are possible in the current Wolf numbers at the rise and decline phases immediately before and after the maximum of the 11-year cycle.

In general, it can be said that SSA is fairly efficient and very promising method for predicting the dynamics of solar magnetic activity. It can also be used to study regularities in series of other astrophysical indices.

ACKNOWLEDGMENTS

This study was supported in part by the Russian Foundation for Basic Research (project no. 00-02-17854) and a youth grant of the Russian Academy of Sciences. K.M. Kyzanyan wishes to thank the NATO grant PST.CLS.976557.

REFERENCES

1. V. S. Afraĭmovich and A. M. Reĭman, in *Nonlinear Waves. Dynamics and Evolution* (Nauka, Moscow, 1989), p. 238.
2. D. S. Broomhead and R. Jones, Proc. R. Soc. London **423**, 103 (1989).
3. D. S. Broomhead and G. P. King, Physica D (Amsterdam) **20**, 217 (1986).
4. D. S. Broomhead and G. P. King, in *Nonlinear Phenomena and Chaos,* Ed. by S. Sarkar (Adam Hilger, Bristol, 1986), p. 113.
5. L. Cao, Y. Hong, H. Fang, and G. He, Physica D (Amsterdam) **85**, 225 (1995).
6. M. Casdagli, Physica D (Amsterdam) **35**, 335 (1989).
7. D. L. Danilov, *Principal Components of Time Series: The Caterpillar Method* (St. Petersburg State Univ., St. Petersburg, 1997).
8. D. L. Danilov and A. A. Zhiglyavskiĭ, *Principal Components in Time Series: Caterpillar Method* (St. Petersburg State Univ., St. Petersburg, 1997).
9. J. Deppish, H.-U. Bauer, and T. Geisel, Phys. Lett. A **158**, 57 (1991).
10. I. V. Dmitrieva, K. M. Kuzanyan, and V. N. Obridko, Sol. Phys. **195** (1), 209 (2000).
11. M. Ghil, Proc. SPIE **3165**, 216 (1997).
12. D. H. Hathaway, R. M. Wilson, and E. J. Reichmann, J. Geophys. Res. **104** (A10), 22375 (1999).
13. D. V. Hoyt and K. H. Schatten, Sol. Phys. **181**, 491 (1998).
14. D. T. Kaplan and L. Glass, Phys. Rev. Lett. **68**, 427 (1992).
15. C. L. Keppenne and M. Ghil, *Exp. Long-Lead Forecast Bulletin* (National Meteorological Center, NOAA, US Department of Commerce, 1992–1995), Vol. 1, Nos. 1–4; Vol. 2, Nos. 1–4; Vol. 3, Nos. 1–4; Vol. 4, Nos. 1–2.
16. J. K. Lowrence, A. A. Ruzmaikin, and A. C. Cadavid, Astrophys. J. **417**, 805 (1993).
17. J. K. Lowrence, A. A. Ruzmaikin, and A. C. Cadavid, Astrophys. J. **455**, 366 (1995).
18. A. Yu. Loskutov and A. S. Mikhaĭlov, *An Introduction to Synergetics* (Nauka, Moscow, 1990).
19. G. G. Malinetskiĭ and A. B. Potapov, *Modern Applied Nonlinear Dynamics* (URSS, Moscow, 2000).
20. D. B. Murray, Physica D (Amsterdam) **68**, 318 (1993).
21. Yu. A. Nagovitsyn, Pis'ma Astron. Zh. **23**, 851 (1997) [Astron. Lett. **23**, 742 (1997)].
22. D. B. Percival and A. T. Walden, *Spectral Analysis for Physical Applications. Multitaper and Conventional Univariate Techniques* (Cambridge Univ. Press, Cambridge, 1993).
23. D. Ruelle, Proc. R. Soc. London **427** (1873), 241 (1990).
24. T. Sauer, Y. A. Yorke, and M. Casdagli, J. Stat. Phys. **65**, 579 (1991).
25. J. Theiler, S. Eubank, A. Longtin, *et al.*, Physica D (Amsterdam) **58**, 77 (1992).
26. K. Schatten, Astron. Soc. Pac. Conf., Ser. **154**, 1315 (1997).
27. R. Vautard, P. Yiou, and M. Ghil, Physica D (Amsterdam) **58**, 95 (1992).
28. R. M. Wilson, D. H. Hathaway, and E. J. Reichmann, J. Geophys. Res. **103**, 17411 (1998).

Translated by V. Astakhov

Astronomy Letters, Vol. 27, No. 11, 2001, pp. 754–757. Translated from Pis'ma v Astronomicheskiĭ Zhurnal, Vol. 27, No. 11, 2001, pp. 877–880.

Unstable Periodic Orbits in a Rotationally Symmetric Potential

T. A. Agekyan, V. V. Orlov*, and N. Yu. Kretser

Astronomical Institute, St. Petersburg State University, Bibliotechnaya pl. 2, Petrodvorets, 198904 Russia

Received October 23, 2000

Abstract—We derive an equation to determine the coordinates of the points at which unstable periodic orbits emerge from a zero-velocity contour in an arbitrary rotationally symmetric potential. Examples of such orbits are given for several model potentials. © 2001 MAIK "Nauka/Interperiodica"

Key words: *nstable periodic orbits, rotationally symmetric potential*

A rotationally symmetric potential is one of the most common forms of potential in nature. The gravitational potentials of planets, stars, globular clusters, and many galaxies are exactly or almost exactly rotationally symmetric.

For the problems of stellar dynamics, analytical and celestial mechanics to be completely solved, a rigorous theory of the motion in a rotationally symmetric potential field must be constructed. The foundations of this theory were laid by Agekyan (1972, 1974), Agekyan and Pit'ev (1977), Agekyan *et al.* (1992), and Pit'ev (1981). The method uses exact laws of the direction field produced by an infinite trajectory in a gravitational field.

Here, our goal is to determine the coordinates of the points on a zero-velocity contour in a rotationally symmetric potential field from which unstable periodic orbits emerge and to give examples of such orbits.

The trajectory of a body lies in the region of possible motions in the meridional plane bounded by the zero-velocity contour

$$U(r,z)+I=0, \tag{1}$$

where $U(r,z)$ is the reduced potential, and I is the energy integral.

Box-shaped and tube-shaped trajectories form angular points with the vertices on the zero-velocity contour. Ollongren (1962) proved that the sides of such orbits at the angular point are mutually orthogonal. Differentiating Eq. (1) yields

$$\frac{\partial U}{\partial r}dr+\frac{\partial U}{\partial z}dz=0. \tag{2}$$

We then have

$$\tan\varphi=\frac{dz}{dr}=-\frac{\dfrac{\partial U}{\partial r}}{\dfrac{\partial U}{\partial z}}, \tag{3}$$

where φ is the angle formed by the tangent to the zero-velocity contour at a given point and the R axis.

Consider the difference

$$\Psi=\varphi-f, \tag{4}$$

where f is the angle between the tangent to one of the sides of a box-shaped or tube-shaped orbit at the angular point and the R axis. We then have

$$\tan\Psi=\frac{\tan\varphi-\tan f}{1+\tan f\tan\varphi}. \tag{5}$$

Using (3), we obtain

$$\tan\Psi=\frac{\dfrac{\partial U}{\partial r}\cos f+\dfrac{\partial U}{\partial z}\sin f}{\dfrac{\partial U}{\partial r}\sin f-\dfrac{\partial U}{\partial z}\cos f}. \tag{6}$$

For equality (6) to define unstable periodic orbits, it is necessary that both the numerator and denominator of the fraction simultaneously become zero (that there be an uncertainty). In that case,

$$\begin{cases}\dfrac{\partial U}{\partial r}\cos f+\dfrac{\partial U}{\partial z}\sin f=0\\[2ex] \dfrac{\partial U}{\partial r}\sin f-\dfrac{\partial U}{\partial z}\cos f=0.\end{cases} \tag{7}$$

Applying the L'Hospital rule to (6) yields

$$\tan\Psi=\left(\frac{\partial^2U}{\partial r^2}\cos^2 f+2\frac{\partial^2U}{\partial r\partial z}\cos f\sin f\right.$$
$$\left.+\frac{\partial^2U}{\partial z^2}\sin^2 f+\left(-\frac{\partial U}{\partial r}\sin f+\frac{\partial U}{\partial z}\cos f\right)\right.$$

*E-mail: vor@astro.spbu.ru

1063-7737/01/2711-0754$21.00

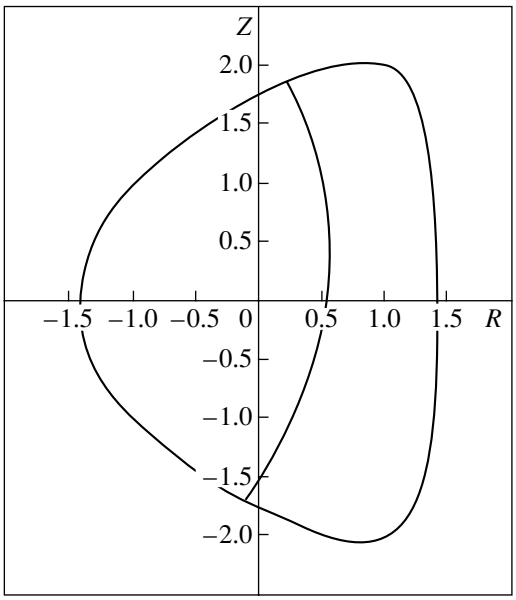

Fig. 1. The first unstable periodic orbit in the Contopoulos potential with parameters $A = 1$, $B = 0.65$, $\varepsilon = 0.2$, $\beta = 0$, and $\alpha = 0$; the energy integral is $I = 1$. The coordinates of the starting point are $r_0 = 0.22954$ and $z_0 = 1.86779$.

$$\times \frac{1}{2(U(r,z)+I)}\left(-\frac{\partial U}{\partial r}\sin f + \frac{\partial U}{\partial z}\cos f\right) \Bigg/ \left(\frac{\partial^2 U}{\partial r^2}\sin f\cos f - \frac{\partial^2 U}{\partial r\partial z}(\cos^2 f - \sin^2 f) - \frac{\partial^2 U}{\partial z^2}\sin f\cos f + \left(\frac{\partial U}{\partial r}\cos f + \frac{\partial U}{\partial z}\sin f\right) \times \frac{1}{2(U(r,z)+I)}\left(-\frac{\partial U}{\partial r}\sin f + \frac{\partial U}{\partial z}\cos f\right)\right). \quad (8)$$

For the property of instability to be preserved, both the numerator and denominator of fraction (8) must also be simultaneously equal to zero at the point under consideration.

Since, according to (7), the last terms in the numerator and denominator of the right-hand part of (8) meet this condition, it is necessary that the following condition be satisfied

$$\frac{\partial^2 U}{\partial r^2}\cos^2 f + 2\frac{\partial^2 U}{\partial r\partial z}\cos f\sin f + \frac{\partial^2 U}{\partial z^2}\sin^2 f = 0. \quad (9)$$

$$\frac{\partial^2 U}{\partial r^2}\sin f\cos f - \frac{\partial^2 U}{\partial r\partial z}(\cos^2 f - \sin^2 f) - \frac{\partial^2 U}{\partial z^2}\sin f\cos f = 0. \quad (10)$$

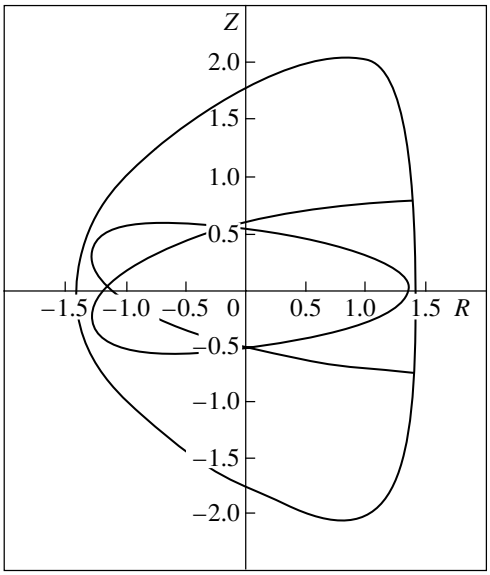

Fig. 2. The second unstable periodic orbit in the Contopoulos potential with the same parameters as in Fig. 1. The coordinates of the starting point are $r_0 = 1.39544$ and $z_0 = 0.75798$.

Excluding the angle f from equalities (9) and (10) leads to the condition

$$\left(\frac{\partial^2 U}{\partial r^2}\frac{\partial^2 U}{\partial z^2} - \left(\frac{\partial^2 U}{\partial z^2}\right)^2 - 2\left(\frac{\partial^2 U}{\partial r\partial z}\right)^2\right)$$

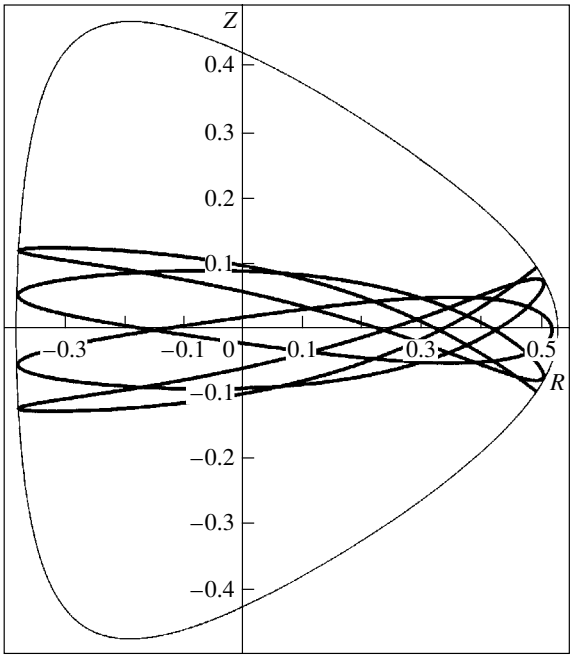

Fig. 3. The first unstable periodic orbit in the Henon–Heiles potential with $A = 1$, $B = 1$, $\varepsilon = -1$, $\beta = 1/3$, and $\alpha = 0$; the energy integral is $I = 0.09$. The coordinates of the starting point are $r_0 = 0.49090$ and $z_0 = 0.0949$.

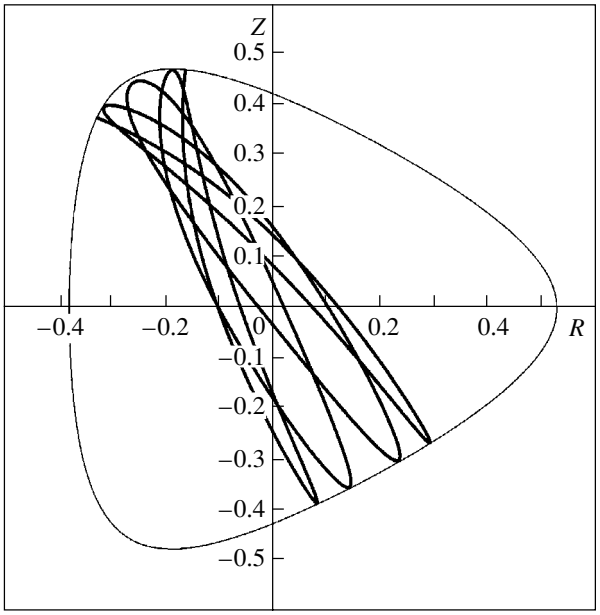

Fig. 4. The second unstable periodic orbit in the Henon–Heiles potential with the same parameters as in Fig. 3. The coordinates of the starting point are $r_0 = -0.32771$ and $z_0 = 0.37764$.

$$\times \left(\left(\frac{\partial^2 U}{\partial r^2} \right)^2 - \frac{\partial^2 U}{\partial r^2} \frac{\partial^2 U}{\partial z^2} + 2 \left(\frac{\partial^2 U}{\partial r \partial z} \right)^2 \right) \quad (11)$$

$$+ \left(\frac{\partial^2 U}{\partial r^2} \frac{\partial^2 U}{\partial r \partial z} + \frac{\partial^2 U}{\partial r \partial z} \frac{\partial^2 U}{\partial z^2} \right)^2 = 0,$$

which together with Eq. (1) defines the coordinates of the points on the zero-velocity potential from which unstable periodic orbits emerge. The method was applied to the Pit'ev model potential

$$U(r,z) = -\frac{1}{2}(Ar^2 + Bz^2) \quad (12)$$

$$+ \varepsilon r z^2 + \beta r^3 + \alpha.$$

The Contopoulos model potential corresponds to $\beta = 0$ and $\alpha = 0$ in (12); the Henon–Heiles model potential corresponds to $\alpha = 0$. The potential and energy integral were specified. We determined the coordinates of the points from which unstable periodic orbits emerged from zero-velocity contour.

The equation of the trajectory

$$\frac{\partial f}{\partial r} \cos f + \frac{\partial f}{\partial z} \sin f \quad (13)$$

$$- \frac{1}{2(U(r,z) + I)} \left(-\frac{\partial U}{\partial r} \sin f + \frac{\partial U}{\partial z} \cos f \right) = 0$$

was numerically integrated by the fourth-order Runge–Kutta method for the specified potential and energy integral. As the initial conditions, we used the coordinates of the points at which unstable periodic orbits emerge from the zero-velocity contour. The initial value f_0 was calculated from the condition

$$\tan f_0 = \frac{\partial U}{\partial z} \Big/ \frac{\partial U}{\partial r}.$$

The numerical integration of Eq. (13) continued over one period (Figs. 1–5). The orbits are seen

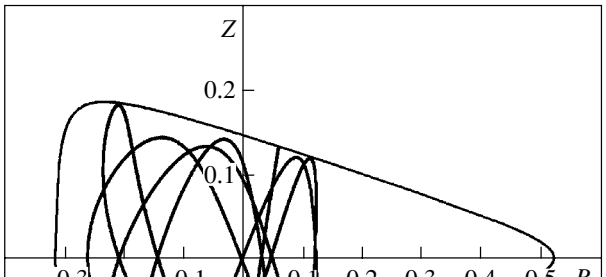

Fig. 5. Unstable periodic orbit in the Pit'ev potential with $A = 2$, $B = -12$, $\varepsilon = -18$, $\beta = 1$, and $\alpha = -1$; the energy integral is $I = 1.13$. The coordinates of the starting point are $r_0 = 0.05915$ and $z_0 = 0.13392$.

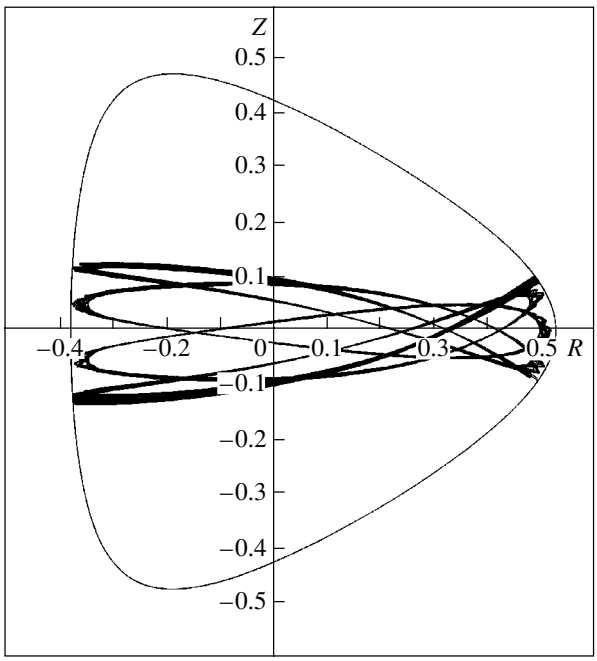

Fig. 6. The results of prolonged integration of the orbit shown in Fig. 3 (the number of turns was increased several-fold compared to Fig. 3 for the same integration step).

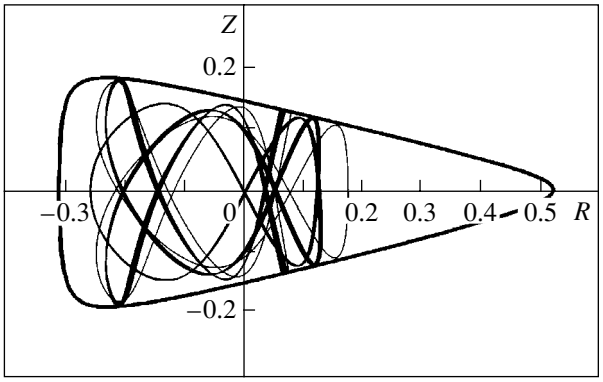

Fig. 7. The results of prolonged integration of the orbit shown in Fig. 5 (the number of turns was increased several-fold compared to Fig. 5 for the same integration step).

to be periodic, because the trajectory returns to the starting point. Figures 6 and 7 present the results of the longer integration of Eq. (13) for the two periodic orbits found over several periods.

In the course of time, the trajectories blur, which argues for the instability of the periodic orbits we found.

The number of unstable periodic orbits in the region of possible motions under consideration can be equal to zero, one, two, or, possibly, more. Unstable periodic orbits can be simple or complex in shape. It is virtually impossible to find unstable periodic orbits by numerical methods. The turns of each of them fills a certain area in the region of possible motions.

The existence of unstable periodic orbits and the clear-cut pattern of their axial lines show that the popular opinion about the comparatively rapid chaotization in the system of orbits in the gravitational field of a rotationally symmetric potential may be wrong.

REFERENCES

1. T. A. Agekyan, Astron. Zh. **49**, 371 (1972) [Sov. Astron. **16**, 303 (1972)].
2. T. A. Agekyan, Dokl. Akad. Nauk SSSR **214**, 783 (1974) [Sov. Phys. Dokl. **19**, 45 (1974)].
3. T. A. Agekyan and N. P. Pit'ev, Astron. Zh. **54**, 1128 (1977) [Sov. Astron. **21**, 641 (1977)].
4. T. A. Agekyan, A. A. Myullyari, V. V. Orlov, *et al.,* Astron. Zh. **69**, 469 (1992) [Sov. Astron. **36**, 236 (1992)].
5. A. Ollongren, Bull. Astron. Inst. Netherlands **16**, 241 (1962).
6. N. P. Pit'ev, Astron. Zh. **58**, 528 (1981) [Sov. Astron. **25**, 299 (1981)].

Translated by V. Astakhov